Proximity Induced Superconducting Properties in One and Two Dimensional Semiconductors

Towards Topological States of Matter

Morten Kjaergaard

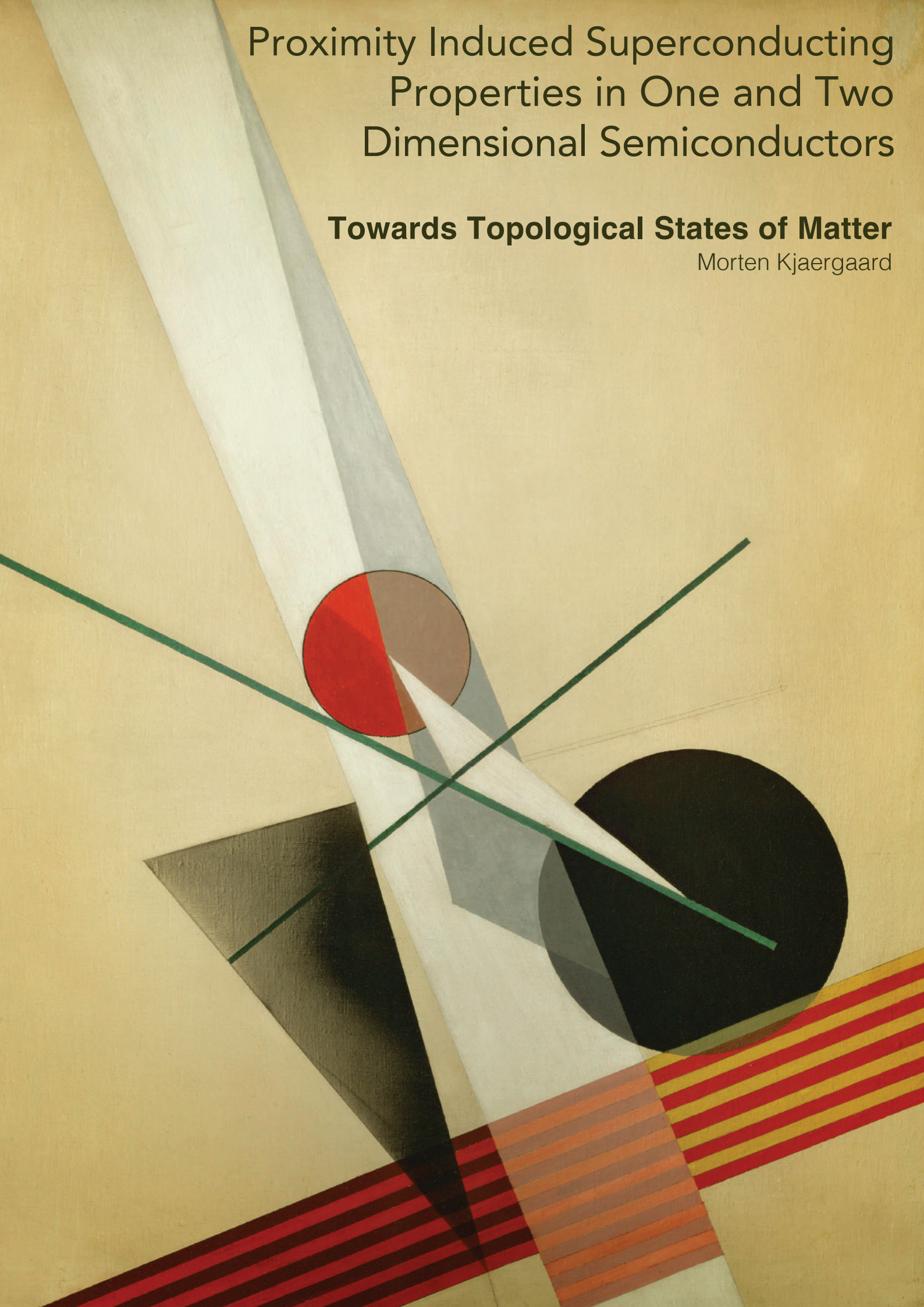

PROXIMITY INDUCED SUPERCONDUCTING PROPERTIES IN ONE AND TWO DIMENSIONAL SEMICONDUCTORS

Towards topological states of matter

MORTEN KJAERGAARD

Ph.D. Thesis
Center for Quantum Devices
Faculty of Science
Copenhagen University

Academic advisors:
Charles M. Marcus & Karsten Flensberg

September 2015

Ad nauseam et ad infinitum. . .

COVER:
Composition A XXI
László Moholy–Nagy
Oil on canvas, 96 x 77cm, 1925

Dedicated in loving memory to my mother Hanne Kjaergaard

1948 – 2013

ABSTRACT

This report is concerned with the properties of one and two dimensional semiconducting materials when brought into contact with a superconductor. Experimentally we study the 2D electron gas in an InGaAs/InAs heterostructure with aluminum grown *in situ* on the surface, and theoretically we show that a superconducting 1D nanowire can harbor Majorana bound states in the absence of spin–orbit coupling.

We fabricate and measure micrometer–sized mesoscopic devices demonstrating the inheritance of superconducting properties in the 2D electron gas. By placing a quantum point contact proximal to the interface between the 2D electron gas and the aluminum, we are able to demonstrate quantization of conductance in units of $4e^2/h$ indicative of perfect Andreev reflection at the interface. We show that the quantum point contact can be operated as a tunnel probe to locally measure the density of states in the electron gas, which shows dramatically suppressed conductance (a hard gap) for energies below the superconducting pair potential. By fabricating Josephson junctions where the 2D electron gas is flanked by two superconducting banks, we also study the supercurrent carrying properties of the 2D electron gas. When a voltage is passed through the Josephson junction, we observe multiple Andreev reflections and preliminary results point to a highly transmissive interface between the 2D electron gas and the superconductor.

In the theoretical section we demonstrate analytically and numerically, that in a 1D nanowire with a superconducting pairing potential, Majorana bound states can exist in the absence of spin–orbit coupling. Our proposal dispenses with spin–orbit coupling at the expense of a locally varying magnetic field. The presence of the topological state is demonstrated analytically by mapping our model onto a superconducting nanowire with topological properties. We deploy a numerical code using the scattering matrix approach to demonstrate the topological state for realistic parameters of a typical nanowire and magnetic fields generated from small permanent magnets.

RESUME

Denne rapport omhandler egenskaber ved en og to dimensionelle halvledende materialer, når disse bringes i kontakt med en superleder. Eksperimentelt studerer vi 2D elektron gassen som formes i en InGaAs/InAs heterostrukture med aluminum groet *in situ* på overfladen. Teoretisk har vi vist at en 1D nanowire kan indeholde bundne Majorana tilstande uden spin–bane kobling i nanowiren.

Vi har fremstillet og målt på mikrometer størrelse mesoskopiske kredsløb, som viser at 2D elektron gassen har nedarvet egenskaber fra aluminium superlederen på overfladen. Ved at placere en kvantepunkt–kontakt ved grænselaget mellem elektrongassen og superlederen, observerer vi at kvantiseringen af konduktansen er i enheder af $4e^2/h$, hvilket indikerer at Andreev reflektionerne er ideelle. Kvantepunkt– kontakten kan bruges som en tunnel kontakt for tilstandstætheden i elektrongassen. Vi har demonstreret at når kvantepunktkontakten bruges som en tunnel kontakt, er konduktansen kraftigt reduceret for energier mindre end parrings–potentialet i superlederen (det såkaldte "hårde gab"). Derudover har vi fremstillet en Josephson kontakt, og studeret superstrømmen. Når en spænding appliceres over Josephson kontakten observerer vi adskillige Andreev reflektioner, indikativt for et rent grænselag imellem halvlederen og superlederen.

Teoretisk har vi demonstreret at i en 1D nanotråd med superledende kontakt kan bundne Majorana tilstande frembringes også uden spin–bane kobling. Vores model bruger lokalt varierende magnetfelter til at erstatte spin–bane koblingen. Den topologiske fase, i hvilken bundne Majorana tilstande kan opstå, demonstreres analytisk ved at vise at det varierende magnetfelt giver ophav til en *effektiv* spin–bane kobling. Vi har udviklet programmel der ved hjælp af spredningsmatrix–formalismen numerisk demonstrerer hvornår nanotråden overgår til den topologiske fase, under realistiske parameter for nanotråden og det fornødne magnetfelt.

ACKNOWLEDGMENTS

I know it's common practice to thank my academic advisors first, but I'll take the liberty of deviating from that tradition briefly. I would like to extend my deepest feelings of gratitude to my father Johan, my brother Jesper and my wife Maria. Your continued support, love and understanding throughout this period is truly amazing. It simply wouldn't have worked out without you. I am grateful that my choices and priorities have always been respected and supported, also in times were the notion of "right decisions" where very far from trivial. Tak for jeres forståelse.

With that being said, the journey from being a young still–wet–behind–the–ears nanotechnology student at Copenhagen University through my first visit to Charlies old lab at Harvard, to helping ultimately dismantle that same lab, just to put it all back together and fabricate my own devices here in Copenhagen, have been a fantastic experience. My initial dabble in theoretical physics, a bout of introspection, and finally finding my place on the shelf as a low temperature quantum transport experimentalist was all made possible by continued trust and encouragement from both Charlie and Karsten. I couldn't hope for better tour guides, and I'm truly grateful you let me try all the rides.

Charlie: Thank you for recognizing and encouraging me to find a more optimal use of my skill set. Your mentorship in a personal relation the first few years of our interactions, up to formally signing on as my Ph.D. advisor has been, and continues to be, invaluable. The hard and acquired taste of justifying skipping dinner (and sleep), so we could load a new chip before going home, to avoid losing a full night of cooling, is a fantastic attitude that I am proud to have picked up, under your guidance. The relentless attention to details of measurement setups and viewgraphs has kept me on my (science–)toes and I'm grateful for the high standard of vigilance that it's required on my part to stay on top of all the details.

Karsten: Thank you – now for the 3rd time! – for being a mentor in not just asking extremely keen questions regardless of the problem at hand being theoretical or practical in nature, but also for being an inspiration

in the broader strokes of establishing life as a young physicist. I am very grateful for all our interactions throughout the years. I think I never thanked you properly for shipping me to Harvard back in 2009. It stands as one of the most important experiences in both my personal life (I met the friend who several years later would become the priest at my wedding!), and my academic life (I was exposed to science outside of Copenhagen University).

Two other people in particular have made this whole thing work out: Henri Suominen and Dr. Fabrizio Nichele. The countless sessions we have shared in front of the e–beam, in front of the evaporator, in front of the whiteboards designing new devices, in front of the fridge(s) and in our offices together have been phenomenal. If this phd is a success by any metric, it would not have been a success without collaborating with you two gentlemen. Thank you so much for all the hard work we've done together. I'm looking forward to another year with long evenings of measurements and terrible jokes.

Javad Shabani is another person without whom the contents of this document would have been dramatically different. I doubt I would've graduated with my sanity in check, had you not offered your wafers. Thank you for growing the beautiful buried InAs heterostructure wafers and then the even–more–beautiful epitaxial aluminum/InAs wafers. Your positive and relaxed attitude have been fantastic, especially when my frustration with leaking devices was reaching a crescendo, your continued faith in the project and me was a tremendous boost. Thanks!

I am also grateful to my committee members: Professors Leo Kouwenhoven and Klaus Ensslin and the local committee chairman Thomas Sand Jespersen. Thank you for taking the time out of your schedules, and I sincerely hope the future brings many more interactions and physics discussions with you – but perhaps under less formal circumstances!

For assisting me in treading the very first steps into the strange world of failed e–beam exposures, lift off problems and non–uniform resist spinning I would like to thank Willy Chang and Hugh Churchill (I'm proud to report all 3 issues have now been solved). Willy, thanks for following Charlies lab here to Copenhagen, I shudder to think how my fab had turned out, had you not been around. Your demeanor and approach have been a big inspiration. I am also grateful to Andrew Higginbotham not just for being about the most rock–solid physicist I know, but also a phenomenal lab mate in all walks of life in QDev. I have really really appreciated our talks and hope we get to do it again, down the road. When it comes to rock–solid though, there really is no one next to Ferdinand Kuemmeth. Your love for finding noise sources, explaining filters and enthusiasm for the technical aspects of low–temperature physics is amazingly contagious. I dedicate the section on the dilution unit in this thesis to you. Another german in the lab who significantly contributed to my happiness and level of fitness: Sven Albrecht. I am extremely happy you joined the group, and I have appreciated our trips to the icecream stand to discuss science, (lab–)life and

bulking. I'd also like to thank Marina, J.T. and Maarten who helped try to get the 2D InSb quantum well structures to work before we had any clue just how hard those wafers were to work with. Your youthful enthusiasm was integral to keeping my sanity while working on that project.

In the last 6 months of the phd I have had the distinct pleasure of working very closely with Josh Folk during his sabbatical here in Copenhagen. I think my data–acquisition and "asking–critical–questions–of–my–data–less–than–2–seconds–after–a–scan–finished"–skills quadrupled with Josh at the setup (and I wouldn't have it any other way).

In this latter part of the phd I have also benefited tremendously from discussing theory and experiments (and rock-climbing) with Anton Akhmerov. Michal Nowak is a brand new colleague who have stepped up with some phenomenal numeric work and I look forward to co–authoring manuscripts including these simulations (and meeting you outside of skype and gchat). If there ever was a seamless start to a new collaboration, I think this is it.

On the theory side I am very happy to have interacted with someone as smart and helpful as Konrad Wölms. Thanks for showing me how to keep track of indices in a scattering matrix. Gediminas Kirsanskas and Astrid Tranum Rømer were fantastic Ph.D. buddies when it said 'theorist' on the office door. Also thanks to Erikas Gaidamauskas who contributed to my understanding and appreciation of the Su–Schrieffer–Heeger model and the Kitaev model.

I would also like to recognize all the great interactions with Kim Splittorff while being a teaching assistant in the course "Quantum Mechanics 2". Working with Kim have been a inspiration in the art of teaching and disseminating science to undergraduates.

Outside of lab life, Tobias, Jon, Jakob and Søren thanks for reminding me that, just every now and then, replacing dilution refrigerators and thermal evaporators with vegan meals and dilapidated German punk squats is an edifying pastime. When it comes to vegan punks, I am happy to thank Thomas Rosén and the positive influence he's had on my life in the latter part of this phd as well. The rest of IRON for likewise impacting my life in such a strong way (and for playing at my wedding!). To Christian Otte I'm sorry I missed so many good shows, and thank you for keeping the torch burning. Thanks to everyone involved in the d.i.y. h/c community in Copenhagen, which have provided a great and positive platform for expressing whatever else might be going on, than blocked precool loops and leaking devices. Finally, a thanks to Peter D., Peter V., Asmus, Tobias and Nicholas for sharing all the ups and downs in life throughout the last many many years.

CONTENTS

LIST OF FIGURES

LIST OF TABLES

1

WHY WORRY ABOUT SEMICONDUCTORS COUPLED TO SUPERCONDUCTORS?

The marriage of semiconductors and superconductors unlocks the potential for controlling and observing novel phenomena in mesoscopic physics. By the process of Andreev reflection from the interface to a superconductor, a carrier in the semiconductor can inherit certain properties of the superconductor while maintaining the semiconducting characteristics, such as tunable carrier density, long mean free paths, spin–orbit properties and their g–factor [1, 2].

In particular, if a semiconductor (say, a 2D electron gas) is sandwiched between two superconductors, a dissipationless supercurrent can flow between the two superconductors despite the semiconducting interposer. This supercurrent is carried by electrons and holes forming a bound state arising from coherent bounces back and forth between the two superconductors [3]. The magnitude of this supercurrent can be controlled by electrostatically changing the electron density in the electron gas, showcasing the combination of superconducting and semiconducting properties.

Also in the single interface superconductor/semiconductor structure does the inheritance of the superconducting properties in the semiconductor lead to exotic phenomena. A superconductor is characterized by a gap in its density of states, usually denoted Δ, around the Fermi energy, and if the superconductor/semiconductor interface is sufficiently pristine, the semiconductor will also show a gap commensurable with Δ in its local density of states. This proximity induced gap can, in concert with properties of the semiconductor, drive a transition into a topological phase, identical to the exotic p–wave superconductor [4, 5, 6, 7, 8]. The quasiparticle excitations in a p–wave superconductor are rather exotic, in that they obey non–abelian statistics and have been proposed as qubits in fault–tolerant topological quantum computing schemes [9, 10, 11].

Between gating a supercurrent in an SNS junction and performing computation on excitations in the effective p–wave superconductor is a significant

amount of materials science, quantum transport experiments and theoretical insights. The use of (effective) p–wave superconductors for quantum computation boils down to the hunt for, and ultimately manipulation of, its quasiparticle excitations – the Majorana bound state. Within the last few years, several very encouraging reports on the experimental signatures of Majorana excitations have appeared [12, 13, 14].

The realization of an effective p–wave superconductor and the understanding of the materials and devices associated with it, is the underlying motivation for both the theoretical and experimental work in this thesis, so we devote the next section to a brief tour of the allure of the Majorana excitation.

1.1 THE PROMISE OF TOPOLOGICAL QUANTUM COMPUTING

The Majorana bound state, named after the Italian physicist Ettore Majorana (1906-1959), is a quasiparticle living at zero energy, which is its own antiparticle. In second quantization this property translates to

$$\gamma^\dagger = \gamma \tag{1.1}$$

What has spurned the increased interest in Majoranas (as they are colloquially named) is not just their remarkable particle/antiparticle property, but also their properties under exchange. Namely, their exchange statistics are non–Abelian (i.e. non–commuting), which means that

$$\psi(\gamma_1, \ldots, \gamma_j, \gamma_{j+1}, \ldots, \gamma_N) = \hat{U}\psi(\gamma_1, \ldots, \gamma_{j+1}, \gamma_j, \ldots, \gamma_N) \tag{1.2}$$

where $\hat{U}$ is a *matrix* representing a rotation in the degenerate subspace of Majoranas at zero energy. In $2+1$ dimensions the exchange of Majoranas can be thought of as strands being weaved around each other (see Figure 1.1), and the process is referred to as braiding. What truly kicked off the excitement was the realization that braiding non–Abelian anyons is equivalent to implementing logical operations on quantum bits [15, 16, 11]. While this in itself is remarkable, the nature of the Majorana fermion makes it insensitive to local perturbations, which in turn makes the braid operations insensitive to local perturbations. In Chapter 6 we will see how this insensitivity comes about (roughly: via the non–local nature of this exotic state). From a quantum computing stand point this would constitute a milestone: Many qubit implementations are limited by decoherence effects due to the environment. While several schemes exist to circumvent the unavoidable errors due to decoherence from the environment, a qubit architecture that is fault–tolerant at the hardware level would be superior.

One implementation of an operation on a quantum memory built from Majoranas, require spatially moving the quasiparticles around to perform

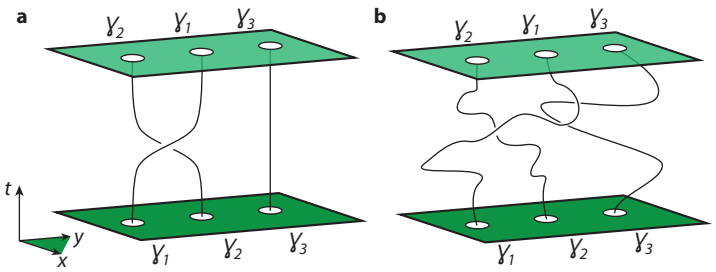

FIGURE 1.1: **a**, Interchange (braiding) of two Majoranas in $2+1$ dimension. **b**, The same braid operation as in **a**, but now with "noise" added on top. As long as the final number of braids is the same, and they're performed in the same order, the braiding will not care how large excursions the particles take from the direct route.

the braiding operations[1]. Thus, to realize scalable topological quantum computing, the Majoranas should reside in a material where complex geometries can be carved using top–down approaches. In a number of landmark papers from 2010 several groups proposed realization of Majoranas in semiconducting systems with spin–orbit coupling, in the presence of an external magnetic field, if the semiconductor is coupled to an *s*–wave superconductor [5, 6, 7, 8]. Shortly thereafter, Alicea and coworkers published a "cookbook" for how braiding operations on Majoranas can be implemented in T–shaped junctions in the semiconductor/superconductor interface devices [20].

The braiding scheme proposed by Alicea is the motivation for the experimental part of this thesis: We are interested in paving way for materials and devices, starting from a 2D electron gas, that can harbor and potentially operate on Majorana particles for quantum computing. The motivation for the theoretical work in this thesis is that spin–orbit coupling, implied in the proposals for topological matter discussed above, is a materials–dependent property which only to a certain extent can be engineered. We have proposed a model that dispenses with the need for intrinsic spin–orbit at the cost of introducing micromagnets proximal to a nanowire.

1 Other proposals exist that dispense with the need for spatially moving the zero–energy state around, but here we focus on the intuitive picture offered by envisioning the Majoranas moving in a 2D plane [17, 18, 19]

1.2 WHATS IN THIS THESIS

This thesis concerns two major subjects under the umbrella realizing p–wave superconductivity: The fabrication and measurement of superconductor/semiconductor devices in a InAs 2D electron gas, with a thin layer of aluminum grown *in situ* on top of the quantum well, and a theoretical investigation into realizing Majorana quasiparticles in semiconducting nanowires without spin orbit coupling. These subjects are covered in three parts:

I: The technology of growing aluminum *in situ* on the quantum well represents a new strategy for forming a highly-transmissive interface between the semiconductor and the superconductor. We therefore devote Chapter 2 to the basic characterization of the quantum well and the aluminum film itself, before proceeding to couple them in the subsequent section. The fabrication steps that we have developed for realizing the superconductor/semiconductor geometries in this structure is discussed in Chapter 3, along with the basics of a dilution refrigerator and the electronic setup used to measured the devices.

II: This part is devoted to measurements of the superconducting properties of a single super/semi (abbreviated SN) interface and of a super/semi/super device (abbreviated SNS). In Chapter 4, the Andreev reflection and the Blonder–Tinkham–Klapwijk formalism is introduced to understand the phenomenology of the SN device. We have observed a doubling of the conductance quantum in a quantum point contact fabricated in the SN geometry, and we introduce the theoretical framework to understand this behavior. In Chapter 5 we focus on the supercurrent carrying properties of the SNS device and the observation of multiple Andreev reflections, which indicate highly transmissive transport through the junction.

III: Finally we review theoretical work on realizing Majorana fermions in 1D nanowires without spin–orbit coupling. In this section we derive the requirement for a topological phase to appear in nanowires with p–wave pairing, show that it maps onto a nanowire with s–wave pairing and spin–orbit coupling in the presence of an external magnetic field. This allows us to study, numerically and analytically, how a nanowire even without spin–orbit coupling, but in the presence of a locally oscillating magnetic field formed by micromagnets, can also exhibit topological properties and harbor Majorana excitations.

The results reported on the bare 2DEG and the superconducting film in Chapter 2 is part of a manuscript to be submitted

EPITAXIAL AL-INAS TWO-DIMENSIONAL SYSTEMS: A PLATFORM FOR GATEABLE TOPOLOGICAL SUPERCONDUCTIVITY

J. Shabani, M. Kjaergaard, H. J. Suominen, Y. Kim, F. Nichele, K. Pakrouski, T. Stankevic, R. M. Lutchyn, P. Krogstrup, R. Feidenhans'l, S. Kraemer, C. Nayak, M. Troyer, C. M. Marcus, and C. J. Palmstrom.
(to be submitted)

Chapter 4 in section II is also based on a manuscript to be submitted

ANDREEV-ENHANCED QUANTUM POINT CONTACT AND TUNNEL SPECTROSCOPY OF A HARD SUPERCONDUCTING GAP IN A 2D INAS ELECTRON GAS

M. Kjaergaard, F. Nichele, H. J. Suominen, J. A. Folk, M. P. Nowak, A. R. Akhmerov, K. Flensberg, J. Shabani, C. J. Palmstrom and C. M. Marcus
(to be submitted)

and likewise, Chapter 5 is based on an ongoing project in the same collaboration, where we are currently developing a numerical framework to reconcile all facets of the data.

Finally, the results in section III is published as

MAJORANA FERMIONS IN SUPERCONDUCTING NANOWIRES WITHOUT SPIN-ORBIT COUPLING

M. Kjaergaard, K. Wölms and K. Flensberg
Physical Review B: Rapid Communications
85, 020503 (2012)

Disclaimer: The results of section III have already been reported as part of the masters thesis on the 4+4 integrated MSc and PhD Program at Copenhagen University. The text and figures presented in the master thesis have been significantly revised for the PhD thesis.

Before diving into the main matter, a general remark on the experimental work presented in this thesis is in order. In the context of coupling superconductors to 2D semiconductors, one issue has marred the field: the problem of the interface transparency, and the experimental work in this thesis was no exception. When this thesis was initiated, we were blissfully oblivious to the gravity of this obstacle. In particular, the initial hope was to form transmissive SN devices out of a high–mobility AlInSb/InSb 2DEG. However, due in part to the small bandgap, the low growth temperature and the presence of a Schottky barrier at an exposed edge of the InSb, processing and

contacting of such wafers is exceedingly difficult. We will show the data on a quantum point contact fabricated on InSb in Section 6.2.1. The data presented in Section 6.2.1 represent the most stable device we succeeded in measuring, but (as evident in Figure 6.6) the gates were still hysteretic and we did not observe quantized conductance in the QPC geometry. Compounded with problems of leaking devices and opaque contacts to superconductors we decided to switch materials.

The InSb was replaced with high mobility buried InGaAs/InAs quantum well heterostructure grown by Javad Shabani, then a post doctoral researcher working in the group of Chris Palmstrom [21, 22]. With these wafers we succeeded in making transparent super/semi contacts and measured a "soft" superconducting gap in the tunneling density of states of the InAs. However, inspired by the recent experiments and significant progress on the SN interface using InAs nanowires with epitaxially grown aluminum *in situ* [23, 24], Javad Shabani pursued a similar structure in 2D. The new wafers were based on the wafers in which we had successfully gated and coupled to superconductors using *ex situ* cleaning and processing. These new wafers, with aluminum grown *in situ* directly onto the surface of an InGaAs/InAs quantum well, has superior quality in terms of interface transparency and critical magnetic field (as we show in Chapters 4 and 5) and consequently, the main matter of the experimental part is based on those wafers. For completeness the fabrication and an overview of the data on the buried high–mobility heterostructure is included in appendix A.

Part I

BASIC CONCEPTS & FABRICATION

This part is devoted to basic concepts and characterization of the 2D electron gas formed in the InGaAs/InAs quantum well and the superconducting properties of the aluminum film. In the 2nd half of this section we turn to device–fabrication and measurement techniques.

2

MESOSCOPIC PROPERTIES OF THE EPITAXIAL ALUMINUM / INAS SYSTEM

This chapter is devoted to setting the stage for the experiments on the InAs 2D electron gas (2DEG) coupled to aluminum. Historically, a major obstacle for coupling superconductors and 2D electron gases has been the processing of the interface between them. The structure of the wafer reported in this thesis sidesteps all fabrication concerns regarding this interface, by having the aluminum grown *in situ* on the surface of 2DEG in the molecular beam epitaxy system. Since these wafers constitute a new paradigm with respect to forming high–transparency contacts we devote this chapter to an introduction to the properties of this "quasi–buried–heterostructure" 2DEG and the aluminum film.

2.1 BASICS CHARACTERIZATION OF THE 2D ELECTRON GAS

A 2 dimensional electron gas is a catch-all term for semiconducting materials where the density of states is such that at a point along the growth direction, electrons are confined to a narrow quantum well (QW). The confined electrons will form standing waves in the growth directions and be free to move in the 2D plane perpendicular to the growth. Most 2DEGs have engineered band structures formed by introducing dopants during growth, which contribute electrons to the confined QW and by carefully choosing the materials in the quantum well and the barriers. In this report we study InGaAs/InAs, a III-V 2DEG. The two most prevalent flavors of 2DEGs are the surface–inversion and heterostructure based systems.

2.1.1 *Surface inversion 2DEG*

The inversion layer 2DEG can be formed in e.g. a hole–doped InAs. At the surface of an InAs wafer, where translational invariance is broken, the

dangling bonds will reconstruct by forming surface states, to align with the Fermi level in the bulk. The surface states are formed by an accumulation of holes, which lead to a bending of the conduction and valence band [25]. For large enough hole concentration, the conduction band dips below the chemical potential at the surface, and the majority carrier in this region is electrons, hence the name 'inversion layer'. The band bending effect is sketched in Figure 2.1. Electrons at the surface are confined to a layer of thickness comparable to the Fermi wavelength (to be discussed below). The band bending effect is the reason for the absence of a Schottky barrier when a metal is deposited onto hole–doped–InAs.

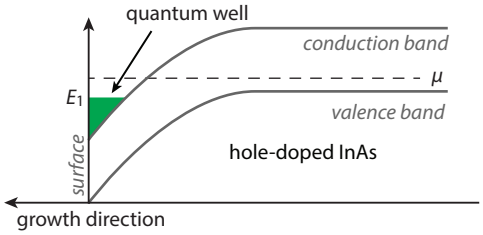

FIGURE 2.1: Sketch of the band bending effect in hole–doped–InAs leading to a surface inversion layer 2DEG.

We mention surface–inversion 2DEGs here, since the structure of the epitaxial aluminum / InAs wafers to be studied in this thesis takes cues from the early insights into surface inversion 2DEGs. Moreover, historically, in the study of superconductor/2D semiconductor interfaces, the surface–inversion variant was used predominantly because the surface area of the superconducting contact to the 2DEG can be orders of magnitude larger than for heterostructure based contacts. Since the inversion layer forms naturally at the surface, a superconductor can be evaporated directly onto the wafer–surface and making, in principle, good contact directly to the electron gas [26, 27, 28, 29]. However, the mobility of surface inversion 2DEGs is severely limited. Furthermore, since the electrons live at the surface, the quality of the 2DEG is highly dependent on details of fabrication and processing of the wafer. To achieve higher mobilities the quantum well can be buried deeper in the wafer.

2.1.2 *Quasi–buried* 2DEG

A different approach to forming confined quantum wells is by engineering the chemical potential by introducing dopants, in sandwiches of materials with differing bandgaps. When two such engineered materials with unequal bandgaps are brought into contact, the chemical potential of the two materials will align and can form a quantum well. Here, we use InAs as the low bandgap material and sandwich it between InGaAs. To align the chemical potential in the InGaAs/InAs/InGaAs sandwich structure, charge is transferred from remote dopants, introduced during growth, and into the

quantum well. The quantum well widths are ∼7 nm. The flexibility of the heterostructure over the surface inversion layer is provided by the ability to change and optimize the growth by introducing buffer layers and dopants. In particular, the heterostructure studied in this report is shown in Figure 2.2a. The wafers are grown by Javad Shabani (then at Chris Palmstroms laboratory in UC Santa Barbara) and is based on a high–mobility and gate-hysteresis free InAs 2DEG heterostructure recently reported [22, 21].

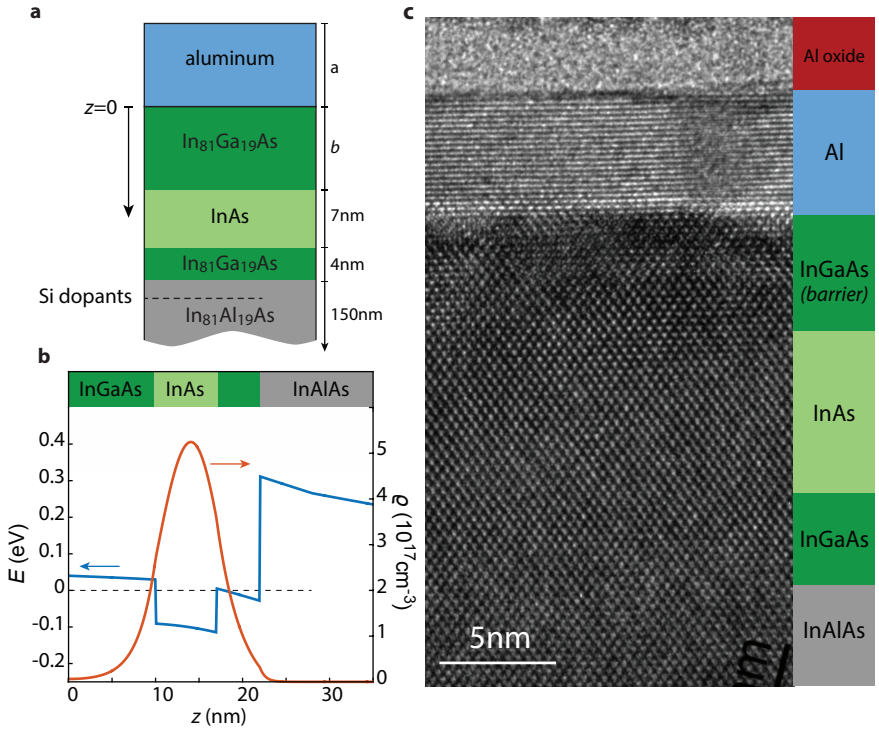

FIGURE 2.2: **a**, Sketch of the wafer structure of the *in situ* grown aluminum on InAs/InGaAs quantum well structure. b is the width of the top–barrier, and a is the width of the aluminum film. **b**, Self–consistent Poisson equation calculation showing the wavefunction predominantly living in the quantum well. **c**, TEM micrograph of a wafer grown under identical conditions to the one studied in this report. The TEM image was taken of a wafer with an aluminum thickness of $a = 5$ nm, and InGaAs barrier thickness $b = 5$ nm. TEM image and heterostructure simulation by J. Shabani.

InAs with a bandgap $E_g^{\text{InAs}} = 0.372$ eV is sandwiched between $In_{81}Ga_{0.19}As$ with a bandgap $E_g^{\text{InGaAs}} = 0.52$ eV [30]. From the bottom, the quantum well is confined with $In_{0.81}Al_{0.19}As$ with a large bandgap $E_g^{\text{InAlAs}} = 0.88$ eV, and on the top an aluminum layer of thickness a caps of the structure.[1] The slightly larger bandgap in $In_{81}Ga_{0.19}As$ localizes the wavefunction predominantly in the InAs, while it still has a non–zero value at the interface to the top aluminum layer. We'll refer to the epitaxial aluminum / $In_{81}Ga_{0.19}As$ / InAs / $In_{81}Ga_{0.19}As$ hetereostructure as simply the "epi-Al/InAs" quantum well from now on. Figure 2.2b shows the density of the wavefunction in

1 The bandgaps quoted in this section is taken from [31] and we have linearly interpolated between the bandgaps of binary alloys to obtain bandgap for the ternary alloys.

the first subband, using a self–consistent electrostatic Poisson solver. The aluminum layer is grown *in situ* in the molecular beam epitaxy chamber. Since vacuum is never broken and the interface is atomically abrupt and oxide free, the interface between the superconductor and the semiconductor is nominally pristine. This strategy of making *in situ* contact between a "quasiburied" 2DEG and a superconductor was introduced back in 1999 in a surprisingly overlooked paper (cited once at the time of writing!) by D.A. Williams [32] using GaAs as the 2D electron gas, and AlGaAs as the spacer. The growth of *in situ* aluminum was also done using a heavily doped GaAs structures as the semiconductor (but without a barrier) by Taboryski *et al.* [33] and in the same group by Kutchinsky *et al.* [34]. Similar results were reported by De Franceschi *et al.* [35].

Javad Shabani supplied several wafers where a few parameters were varied between each growth. The bottom InGaAs barrier was kept fixed at 4 nm and the InAs QW was always grown with a thickness of 7 nm, while the thickness of the top barrier and the aluminum was varied. It was not clear what the quality of the 2DEG grown in the epi-Al/InAs structure would be, and it was not at all clear if the 2DEG would inherit any of the properties of the aluminum, via Andreev reflections from the interface (to be discussed at greater length in Section II). For this reason we investigated in particular two wafers: JS113, with no InGaAs barrier ($b = 0$ nm) between the InAs and the aluminum, and JS118, with a 10 nm InGaAs barrier ($b = 10$ nm). Those two wafers were chosen based on an educated guess that JS118 would have a higher mobility (due to the InGaAs barrier separating InAs from the surface), and that if the InAs QW should have superconducting properties, it should at least work in the wafer with no barrier between the InAs and the aluminum. Indeed, the material with 10 nm barrier has higher mobility, but surprisingly both wafers exhibited similar superconducting properties, as evident through the measurement of a supercurrent in an SNS geometry and a gap in the local density of states measured using a tunnel probe, in both wafers. These two results are the subject of Chapters 4 and 5 in Section II.

In the following sections we present theory and mesoscopic characterization of the 2DEG formed in the epi-Al/InAs quantum well structure. The aluminum is chemically etched away prior to characterization of the 2DEG. We'll focus on the 2DEG and the superconducting films separately, and details of the fabrication and measurements are relegated to Chapter 3.

2.1.3 *Cursory review of mesoscopics of the 2DEG*

Usually the quantum well can be modeled as a finite square well[2]. The dispersion relation $E_n(k_x, k_y) = \frac{\hbar^2 k^2}{2m^*} + E_n$ of a 2D quantum well forms parabolic

2 In the case a surface inversion quantum well, or for heavily doped structures, a triangular potential shape can be more appropriate.

bands shifted upwards by the index n, corresponding to the confinement in the well. In Figure 2.3a we have sketched the parabolic bands.

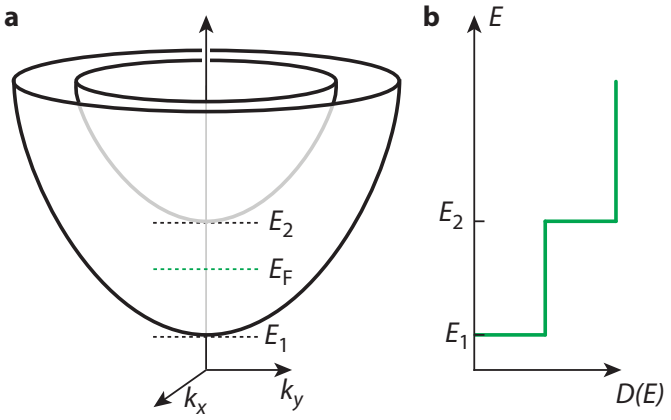

FIGURE 2.3: **a**, Sketch of the dispersion relation in a square quantum well, with the first two (parabolic) subbands. In the case of quantum well with one level occupied, the Fermi level E_F will be located between E_1 and E_2. **b**, The density of states in 2D.

A few mesoscopic parameters of the 2DEG are key when evaluating properties of the SN and SNS systems which we analyze later in this report. The density of states in 2D is constant and given by

$$\mathcal{D}(E) = \frac{d\mathcal{N}}{dE} = \frac{m^\star}{\pi\hbar^2}. \tag{2.1}$$

where $m^\star$ is the effective mass. If the dispersion is isotropic, then

$$\frac{1}{m^\star} = \frac{1}{\hbar^2}\frac{d^2E}{dk^2} \tag{2.2}$$

and thus for $E(k)$ parabolic the effective mass is a constant. However, if k is not small and the bandgap is small (as for our InAs), significant deviations from the parabolic dispersions can occur, due to mixing with other bands. This effect is relevant for our wafers, as we'll see below.

The density of electrons in a 2DEG with one subband occupied can be calculated using the density of states

$$n = \int_{E_1}^{E_F} dE\mathcal{D}(E) = \frac{m^\star}{\pi\hbar^2}(E_F - E_1) \tag{2.3}$$

The wavevector corresponding to the states at the Fermi energy is denoted k_F, and is given by $E_F - E_1 = \frac{\hbar^2 k_F}{2m^\star}$. Upon plugging k_F into Equation (2.3), we arrive at the relation

$$k_F = \sqrt{2\pi n}. \tag{2.4}$$

Once the density n of carriers is measured, the Fermi wavevector can be calculated using Equation (2.4).

Important derived quantities are the Fermi wavelength, Fermi velocity and Fermi energy,

$$\lambda_F = \frac{2\pi}{k_F} \quad , \quad v_F = \frac{\hbar k_F}{m^\star} \quad , \quad E_F = \frac{\hbar^2 k_F^2}{2m^\star} \tag{2.5}$$

The average time between undergoing elastic scattering is denoted τ_e, and is given by $\tau_e = \frac{m^\star}{e}\mu$. The quantity μ is the mobility of the 2DEG and has units [m^2/Vs]. The mean free path is then given by

$$l_e = v_F \tau_e = \frac{\hbar}{e}\mu\sqrt{2\pi n} \tag{2.6}$$

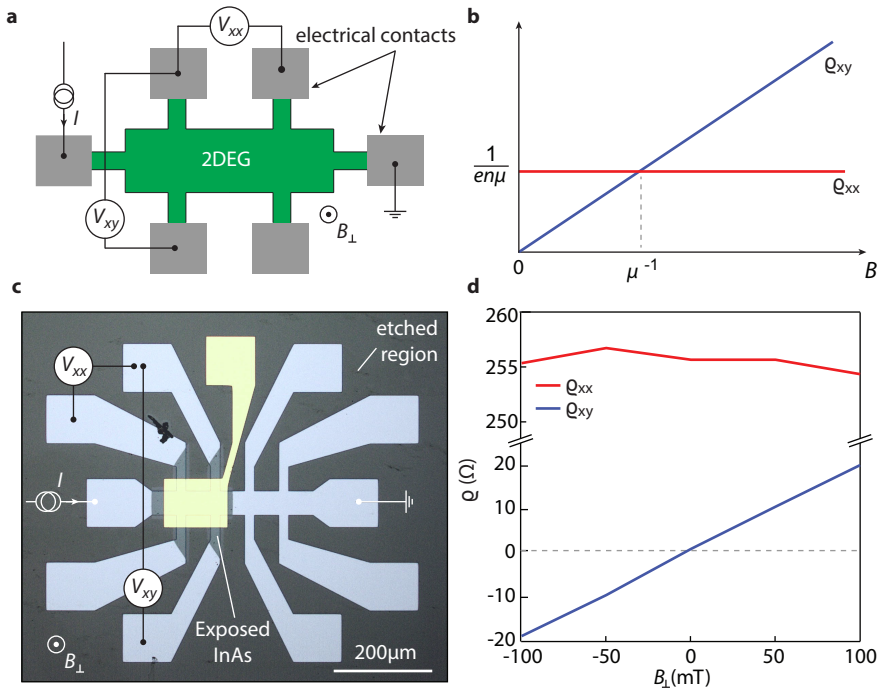

FIGURE 2.4: **a**, Sketch of a hallbar geometry with measurement setup. Gray areas indicate metallic contacts to the 2DEG. **b**, Cartoon of $\rho_{xx} = (V_{xx}/I)\cdot(W/L)$ and $\rho_{xy} = V_{xy}/I$, with indication of their relationship to mobility and density. **c**, Optical micrograph of Hallbar in epi–Al/InAs heterostructure. Regions without aluminum are dark gray (barely distinguishable to the etched background), the light orange is Ti/Au gate used to tune the density, and regions with aluminum left intact is silver. **d**, Low field magnetoresistance measurements of ρ_{xx} and ρ_{xy} in a hallbar lithographically identical to the one in **c**. The L/W ratio is in this case 1.4, where L is measured from the middle of the V_{xx} probes.

The two quantities n and μ are measured using a hallbar geometry, shown in Fig.2.4. From the magnetoresistance we extract the density and mobility using the relations

$$n = \frac{1}{e\frac{d\rho_{xy}(B=0)}{dB}} \quad , \quad \mu = \frac{1}{en\rho_{xx}(B=0)} \tag{2.7}$$

The mesoscopic parameters at $V_g = 0$ V are tabulated in Table 1 for the 10 nm and 0 nm barrier wafers.

InGaAs	$\rho_{xx}(\Omega)$	$n(\mathrm{m}^{-2})$	$\mu(\mathrm{cm}^2/\mathrm{Vs})$	$k_F(\mathrm{nm}^{-1})$	$\lambda_F(\mathrm{nm})$	$l_e(\mathrm{nm})$
0nm	332	$4.5 \cdot 10^{16}$	4.130	0.019	11	145
10nm	255	$3.2 \cdot 10^{16}$	7.500	0.022	14	230

TABLE 1: Review of mesoscopic data in the two wafers studied in this thesis.

Figure 2.5 shows the mobility and density dependence as the topgate is used to deplete the 2D electron gas in the wafer JS118 with a 10nm InGaAs barrier. The derived quantities l_e and λ_F correspondingly vary with the topgate and are shown in Figure 2.5. The non–monotonic behavior of mobility as the 2DEG is depleted (Figure 2.5b) is speculated to be the result of pushing the wavefunction away from the epi–Al interface and thereby decreasing the "surface roughness". From the simulations we know that the band edge of the 2nd subband is around 0.29 eV so the non–monotonicity is not an effect of the second subband entering the quantum well.

Due to the small bandgap of InAs and the high density in our wafers, deviations from the parabolic dispersion have to be considered, and the effective mass is not given by the straightforward relation in Equation (2.2). Using numerical simulation of the 8×8 Kane model [36], Rafal Skolasinski, working in the group of Michael Wimmer, has simulated the band structure of the wafer shown in Figure 2.2a for the case $b = 10$ nm. The simulation includes the density and accounts for non–parabolic corrections, but do not include modifications due to the surface aluminum. The effective mass is found to be $m_{\mathrm{eff}} = 0.051 m_0$, roughly a factor of 2 larger than the bulk InAs effective mass of $0.023 m_0$ [36]. Using this effective mass for the 10 nm InGaAs barrier wafer, the Fermi energy, Fermi velocity and elastic scattering time is calculated to be

$$E_F = 0.147 \text{ eV}, \quad v_F = 9.3 \cdot 10^5 \text{ m/s}, \quad \tau_e = 0.22 \text{ ps} \tag{2.8}$$

Many of the properties relating to SN and SNS junctions studied in the next chapters are limited by the phase coherence length. For electrons moving in a solid, their phase is randomised on a timescale denoted τ_ϕ. Static, non–magnetic impurities are time-reversal invariant and does not lead to dephasing, but phonons and electron–electron interaction will decrease τ_ϕ. At the base temperature of a dilution refrigerator $T \approx 30$ mK the phononic degrees of freedom are completely static. However, the e–e interactions will lead to dephasing. We can estimate a length scale for this process as follows. After a time τ two electrons with energy difference ΔE will acquire a relative phase $\phi = \tau \Delta E/\hbar$. When ϕ is of order unity, the two electrons are completely uncorrelated. Due to the Fermi–Dirac statistics, their energy difference is $\Delta E \sim k_B T$. In the time τ the electrons will have traveled $l = v_F \tau$ in a ballistic system and $l = \sqrt{D\tau}$, where D is the diffussion con-

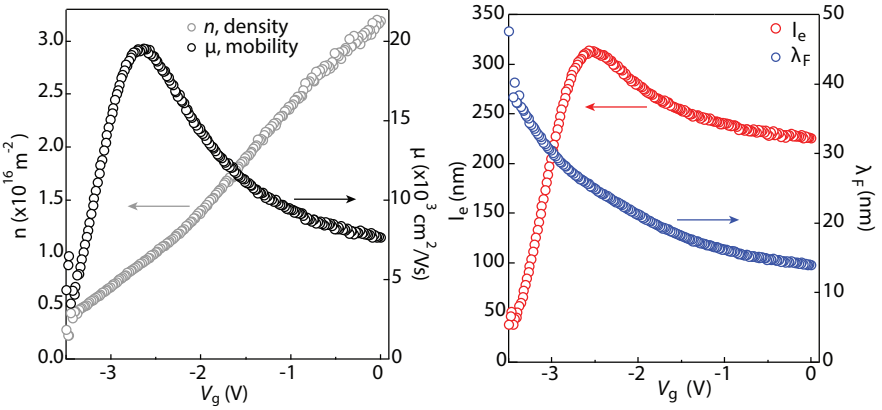

FIGURE 2.5: **a**, Density and mobility in wafer JS118 with a 10 nm InGaAs barrier as a function of topgate voltage. **b**, Mean free path and Fermi wavelength in the JS118 wafer.

stant $D = v_F l_e/2$ in 2 dimensions, in a diffusive system. The thermal phase coherence length is then

$$\xi_{N,\text{bal}} = \frac{v_F \hbar}{k_B T} \quad , \quad \xi_{N,\text{diff}} = \sqrt{\frac{v_F l_e \hbar}{2 k_B T}} \tag{2.9}$$

The study of how properties of a mesoscopic sample scales with coherence length, mean free path and sample size is an exceedingly rich field, and the cursory review here does not do it justice. The reader is referred to Imry's wonderful book [37].

For the remainder of the experimental part of the thesis, we will stick to measurements on wafer JS118 (10 nm InGaAs barrier), with the highest mobility, lowest density and longest mean free path. In all cases, devices fabricated on JS113 (0 nm InGaAs barrier) showed qualitatively similar properties to JS118, but were generally more noisy and unstable when gated to low density.

2.1.4 *The quantum point contact*

The conductance through a sufficiently narrow constriction in a 2DEG is quantized in values of $G_0 = \frac{2e^2}{h} \approx 3.87 \cdot 10^{-5}\ \Omega^{-1} \approx 1/12906\ \Omega$. This remarkable effect was observed in 2DEGs by van Wees *et al.* [38] and Wharam *et al.* [39] in the quantum well in a AlGaAs/GaAs heterostructure and is now a classic result in low–temperature condensed matter physics. The geometry used for these experiments is the split gate quantum point contact. A negative voltage can be applied on metallic gates electrically isolated from the 2DEG to form a constriction with an effective width $W(V_g)$ set by the voltage on the gate. For appropriate dimensions and layout of the gates, as the voltage is increased[3] the effective width of 2DEG will be comparable to

3 Throughout this thesis, by "increasing" gate voltage, it is understood that the voltage is turned more negative

the Fermi wavelength, $W(V_g) \sim \lambda_F$. If the temperature is low enough that the level spacing in the QPC is the dominant energy scale, then conductance becomes quantized. One of the main results of the experimental efforts in this report is the study of how the fundamental quantization through a QPC is modified, if it is placed proximal to a superconducting interface.

For quantization to be observable, the quality of the 2DEG and the design of gate–geometry should be such that $l_e \gg L, W$. Figure 2.6a the split–gate experimental realization of a QPC in a 2DEG.

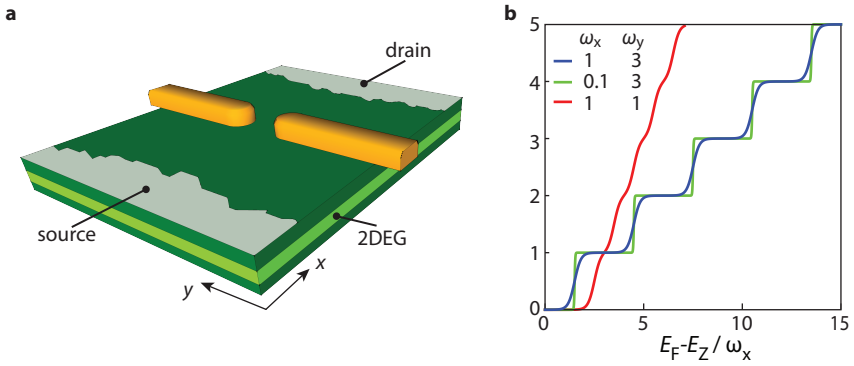

FIGURE 2.6: **a**, Sketch of the split gate quantum point contact geometry. Details of the shape of the gate has direct implications for the observation of quantized steps. **b**, Conductance of the first few modes in the saddlepoint constriction model, for a few parameters of the potential landscape. Calculated using Equations (2.10), (2.12) and (2.13).

For a small applied bias (the linear–response regime), and at low temperatures, the conductance through the QPC is given by the Landauer-Buttiker formula (see e.g. [37, 40] or any other mesoscopic physics book worth its salt)

$$G = \frac{2e^2}{\hbar} \sum_n^N \mathcal{T}_n(E_F). \tag{2.10}$$

By modeling the potential in the constriction as a saddle point [41, 42],

$$\mathcal{V}(x,y,z) = -\frac{1}{2}m^\star\omega_x^2 x^2 + \frac{1}{2}m^\star\omega_y^2 y^2 + \mathcal{V}(z), \tag{2.11}$$

the transmission through each mode can be found analytically

$$\mathcal{T}_n(E) = \frac{1}{1+e^{-2\pi\epsilon_n}}, \tag{2.12}$$

where

$$\epsilon_n = \frac{E - \hbar\omega_y(n+1/2) - E_z}{\hbar\omega_x} \tag{2.13}$$

This equation is powerful for building intuition about the behavior of the steps in a QPC and the underlying potential. Well-developed plateaus in the QPC will occur if the ratio $\omega_y/\omega_x \gg 1$, which also intuitively makes sense:

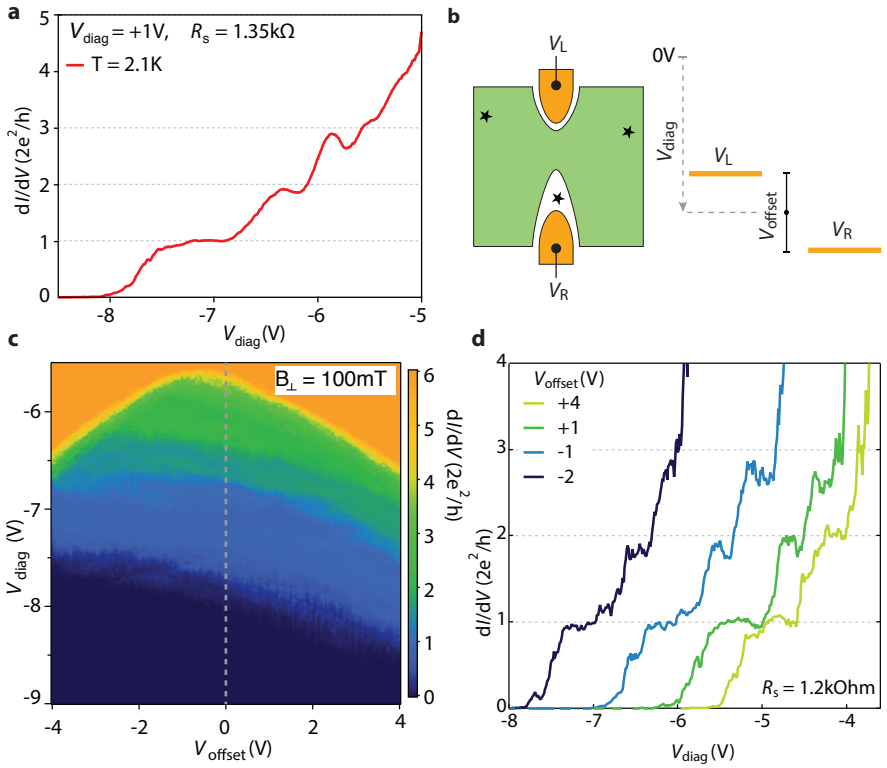

FIGURE 2.7: **a**, Pinchoff trace at elevated temperature. This trace taken with $V_{\text{offset}} = +1$ V, and a series resistance $R_c = 1.3$ kΩ have been subtracted. Details of the series resistance is given in Chapter 4. **a**, Sketch of the 2DEG when the gates are set asymmetrically. Stars indicate impurities. The diagram indicates definitions of V_{diag} and V_{offset}. **c**, Pinchoff map showing how the conductance through the QPC varies as the asymmetry between the gates is varied. The dashed line indicates symmetric gating. We have applied a perpendicular field $B_\perp = 100$ mT, because this QPC was fabricated with aluminum contacts in close proximity. **d** Cuts in the pinchoff map showing how QPC varies with asymmetric gating.

The level spacing in the QPC is related to the steepness of the potential, which is set by ω_y^2, so a large ω_y indicates well–separated spacing. The level spacing in the constriction manifests itself as the width of the conductance plateaus. Furthermore, $\hbar\omega_x$ is related to the smoothness of the potential (on the scale of λ_F), which in turn determines sharpness of the transition between the plateaus. Figure 2.6b shows how the step shape is dependent on the relative sizes of ω_y and ω_x. Other effects than just the shape of the potential formed by the gates can have detrimental influence on the quantized conductance. The QPC steps shown in Figure 2.7a and 2.7d are of unequal size, and show oscillations on top of the plateau structure.

- In the case where $l_e \sim L$, transport through the constriction is not fully ballistic and the effect of scattering within the QPC has to be taken into account. Scattering can lead to resonances, which manifests themselves as deviations from the idealized monotonic decrease in conductance with increasing gatevoltage.

- A local charge impurity close to the constriction can dramatically change the local potential, again leading to strong deviation from the saddle–point model. We can sometimes sidestep such resonances by applying the gate–voltage asymmetrically. This idea is sketched in Figure 2.7b, and in 2.7a we show a pinchoff curve where the gates are tuned asymmetrically. In Figure 2.7c and 2.7d the "pinchoff map" shows how resonance change in the QPC when the gates are biased asymmetrically. The resonances can be tracked independently from how the position of the plateaus move.

By elevating the temperature resonances tend to be smoothed out, due to thermal averaging, as is evident when comparing the curve in Figure 2.7b at elevated temperatures, and Figure 2.7d. A magnetic field applied perpendicular to the plane of the QPC can also clean up the QPC steps. The introduction of an Aharanov-Bohm contribution to the phase eliminates the coherent nature of the backscattering and resonances become suppressed.

Finally we note, that for the data presented in this report the gate–dependence of the devices would shift over time. This has the unfortunate consequence that the gate–voltage in different viewgraphs will not necessarily line up with each other. This is evident in comparing e.g. Figures 2.7b, 2.7c and 2.7d.

2.2 CRASH COURSE IN BCS THEORY

We now turn our attention to superconductivity and the basics of the BCS theory. In their landmark paper from 1957 Bardeen, Cooper and Schrieffer successfully worked out a microscopic model to explain superconductivity [43]. In their model, below a certain critical temperature T_c, electrons with opposite momentum and spin pairs up and lower the energy of the system. Such pairs are bosonic particles built from $(\boldsymbol{k}\uparrow, -\boldsymbol{k}\downarrow)$–electrons and are called Cooper pairs. The pair–forming potential is mediated by the electron–phonon interaction [3]. In the condensed state where Cooper pairs have formed, the system has a gap of size Δ in the density of states. The superconducting gap is pinned to the Fermi level, unlike the gap in insulators and semiconductors, and there are no states available with energy $E < \Delta$.

Excitations from this condensed state can be described by the Bogoliubov-de Gennes (BdG) equation [3, 44],

$$\begin{bmatrix} H(\boldsymbol{r}) & \Delta(\boldsymbol{r}) \\ \Delta^*(\boldsymbol{r}) & -H(\boldsymbol{r}) \end{bmatrix} \Psi_{\boldsymbol{k}}(\boldsymbol{r}) = E\Psi_{\boldsymbol{k}}(\boldsymbol{r}), \tag{2.14}$$

where

$$\Psi_{\boldsymbol{k}}(\boldsymbol{r}) = \begin{pmatrix} u_{\boldsymbol{k}}(\boldsymbol{r}) \\ v_{\boldsymbol{k}}(\boldsymbol{r}) \end{pmatrix} \tag{2.15}$$

is a two–component wave function in electron and hole space. The factor $u_{\boldsymbol{k}}$ ($v_{\boldsymbol{k}}$) describe the electron (hole) content of the state $\Psi_{\boldsymbol{k}}(\boldsymbol{r})$. If $|u_{\boldsymbol{k}}|^2 > |v_{\boldsymbol{k}}|^2$ we call the state electron–like (and hole–like in the reverse case). In the absence of the superconducting gap Δ the electron and hole parts in (2.14) decouple into two single–particle states. The bare single–electron hamiltonian is given

$$H(\boldsymbol{r}) = -\frac{\hbar^2}{2m^*}\nabla^2 + U(\boldsymbol{r}) - \mu \tag{2.16}$$

where $U(\boldsymbol{r})$ is a scalar potential. For a homogeneous superconductor $\Delta(\boldsymbol{r}) = \Delta_0 e^{i\phi}$, where ϕ is the phase of the superconducting order parameter. In the absence of a scalar potential $U(\boldsymbol{r}) = 0$, the solutions to Equation (2.14) are particularly simple and illuminating. The spatial dependence of the wavefunction can be separated out

$$\Psi(\boldsymbol{r}) = e^{i\boldsymbol{k}\cdot\boldsymbol{r}} \begin{pmatrix} u_0 \\ v_0 \end{pmatrix} \tag{2.17}$$

inserting this form of $\Psi(\boldsymbol{r})$ into Equation (2.14) yields expressions for the coherence factors

$$u_0^2 = \frac{1}{2}\left(1 + \frac{\sqrt{E^2 - \Delta_0^2}}{E}\right) \tag{2.18}$$

$$v_0^2 = 1 - u_0^2 \tag{2.19}$$

and the energies are given by

$$E = \pm\sqrt{\xi_k^2 + |\Delta_0|^2}, \qquad \xi_k = \frac{\hbar^2}{2m^*}k^2 - \mu. \tag{2.20}$$

In Figure 2.8 we have plotted the coherence factors and the (positive) energies of single–particle excitations in a BCS superconductor. From Figure 2.8a it is evident that excitations with $k > k_F$ are electron–like and excitations with $k < k_F$ are hole–like.

The density of states (DOS) in the superconductor can be determined heuristically using Equation (2.20). A superconductor is a metal with a gap around E_F, so we can equate the DOS of the superconductor to the DOS in a normal conductor, but with a gap:

$$N_s(E)dE = N_n(\xi)d\xi \tag{2.21}$$

Since we are only interested in physics around E_F where the normal state DOS is constant, Equation (2.21) takes the simple form

$$\rho_s(E) \equiv \frac{N_s(E)}{N_n(0)} = \frac{d\xi}{dE} = \begin{cases} \frac{E}{\sqrt{E^2-\Delta^2}} & E > \Delta \\ 0 & E < \Delta \end{cases} \tag{2.22}$$

In figure 2.8c the density of states of quasiparticles in the superconductor is plotted as a function of energy.

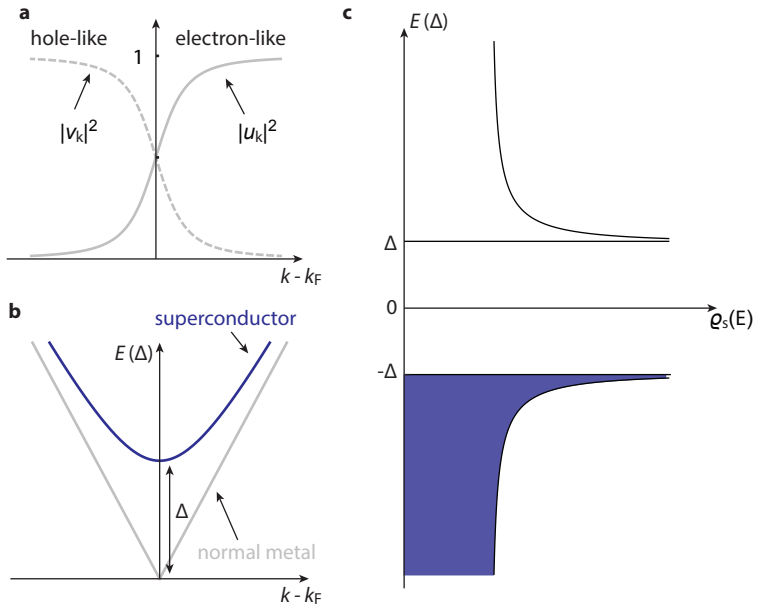

FIGURE 2.8: **a**, The value of the coherence factors $u_{\boldsymbol{k}}$ and $v_{\boldsymbol{k}}$ close to $\boldsymbol{k} = \boldsymbol{k}_F$ (in one direction of $\boldsymbol{k}$). **b** The energy gap in a superconducting material compared to a normal metal with $\Delta = 0$. **c**, The density of states $\rho_s(E)$ of the quasiparticles in a superconductor. The states witb $|\Delta| < E$ have been pushed out of the gap.

The group velocity of a particle is given by

$$v_{\boldsymbol{k}} = \frac{1}{\hbar}\nabla_{\boldsymbol{k}} E \tag{2.23}$$

For electrons with momentum $\boldsymbol{k} > \boldsymbol{k}_F$ the energy is positive and for $\boldsymbol{k} < \boldsymbol{k}_F$ their energy is negative and thus, the group velocity and wavenumber $\boldsymbol{k}$ of electrons have the same sign (relative to $\boldsymbol{k}_F$). For holes, this situation is reversed, leading to the observation that they move in reverse direction to the sign of their wavenumber. This point will lead to interesting consequences in Chapter 4, when we introduce Andreev reflection and the proximity effect.

2.2.1 *Properties of the thin aluminum film*

We close this chapter by briefly discussing the properties of the thin aluminum film. In the hallbar shown in Figure 2.4c, a large region of the

aluminum is left unetched. We have measured the properties of 5 nm and 10 nm aluminum film in a current biased 4–terminal measurement setup, as a function of temperature and in–plane magnetic field. The results are shown in Figure 2.9. The alignment of the magnetic field to was performed with a vector magnet after the samples were loaded. The 5 nm film has a small finite resistance even at base temperature. This is due to a parallel conduction path within the wafer leading to a small parasitic resistance.

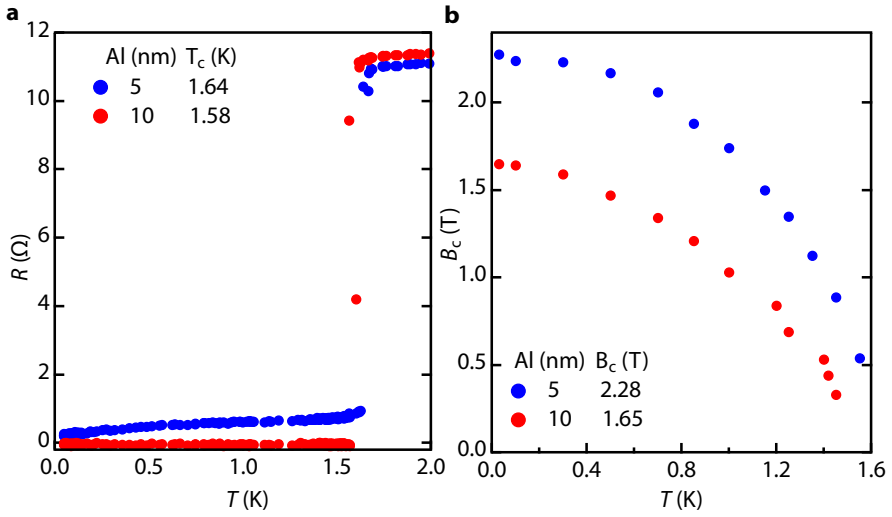

FIGURE 2.9: **a**, The temperature dependence of the superconducting state in two aluminum films. **b**, The temperature dependence of the in–plane critical field.

From the critical temperature it is possible to estimate the size of the superconducting gap at $T = 0$ within BCS theory [3]

$$\Delta(0) = 1.764 k_B T_c \tag{2.24}$$

The slightly awkward–looking numerical factor 1.764 stems from the evaluation of an integral of the form $\int \tanh(x)/x$ whose solution involves Eulers constant. The critical temperature and critical in–plane magnetic field in Figure 2.9 show excellent agreement with previously published results on thin aluminum films [45, 46]. The critical in–plane field B_c can be compared to the theoretical maximal value. In this limit, the spin–singlet pairing of the coopers pairs (in an s–wave superconductor) is broken by the paramagnetic contribution from the external field, effectively killing superconductivity. This effect is was originally discussed by A.M. Clogston and B.S. Chandrasekhar [47, 48]. For superconductors with negligible spin–orbit interaction, the Clogston-Chandrasekhar limit is given by [3]

$$B_{\text{limit}} = \frac{\Delta_{\text{Al}}}{\sqrt{2}\mu_B} \approx 2.8 \text{ T} \tag{2.25}$$

The critical field of the 5 nm film is reasonably close to the Clogston-Chandrasekhar limit. Despite the higher B_c of the 5 nm film, we will concentrate on the

aluminum thickness (nm)	T_c (K)	B_c (T)	Δ_{Al} (μeV)
5	1.64	2.28	235
10	1.58	1.65	225

TABLE 2: Properties of the superconducting thin films. *measured at $T = 30$ mK

wafer with the 10 nm film, because of the parallel conduction path in 5 nm aluminum wafer, and due to 2DEG in the 10 nm wafer being of a higher quality. The temperature, magnetic field and gap properties of the two films are listed in Table 2.

3

DEVICE FABRICATION & MEASUREMENT TECHNIQUES

This chapter is devoted to the hands–on part of being a low temperature quantum transport experimental physicist. We go through the fabrication process of the devices measured in this report, some basics of the Triton He^3-He^4 dilution units as well as measurement techniques. The device fabrication process is often relegated to appendices in the ph.d. thesis, but the tough art of producing and designing micron– and nanometer scale devices has been a key part of the research reported here. Working with new and unexplored wafers has provided obstacles that we have surmounted as they became apparent. In the hope of helping other researchers working on similar new 2DEG structures hurdling such obstacles, we devote some time to identifying and avoiding potential issues with a wafer/chip/device.

3.1 FABRICATION OF SAMPLES IN EPI–AL/INAS MATERIAL

Fabrication of a device can be split into the following steps:

1. Designing the device
2. Etching mesa
3. Etching aluminum
4. Deposition of insulator
5. Deposition of gates (a 2-step process)
6. Bonding and preparation for cooldown

We will go through each step in more detail below. The fabrication of these samples require relatively few fabrication steps compared to superconducting contacts to buried 2DEG heterostructures. For the buried structures, a separate step for cleaning the interface and depositing the superconductor is necessary (see e.g. the fabrication recipe in Appendix A). The cleaning of

the interface is perhaps the most crucial point for such devices (indeed, a full chapter is devoted to this issue in Thomas Schäpers great book *Superconductor/Semiconductor Junctions* [44]). The issue of the quality of the interface is central to many experimental reports on superconductor/2DEG interfaces [27, 49, 50, 51]. We conjecture that the problem of achieving sufficiently clean interfaces is part of the reason for the stalled interest in coupling superconductors to 2DEGs. The ohmic contacts in our epi–Al/InAs wafers are naturally formed via the aluminum grown on the 2DEG, leaving out another step in fabrication.

3.1.1 *Cleaving and preparing a chip*

The chips are cleaved from quarter inch wafers, and the optimal chip size we found is 2.5×5 mm. Cleave them smaller and you run into issues because the resist edge–beads are of a size that can lead to non–uniform resist coverage throughout the entirety of the small chip (see Section 3.1.3). A significant amount of prototyping was necessary to develop the mesa– and aluminum–etch recipes presented below, so we kept the chip sizes as small as possible to keep wafer consumption down.

After cleaving the chip it is rinsed in 3–step solvent clean:

- 2 min in TCE (always start with the most aggressive of the solvents)
- 2 minutes in acetone
- 1 minute dunk in IPA
- Finally blow–drying the chip with N_2

Before continuing fabrication the chip is inspected under a microscope. A lot can be learned from carefully looking at the surface of the chip before further processing. Figure 3.1 shows a few examples of the surface on unprocessed wafers. A few general rules of thumb that we learned the hard way: stay away from edges of the wafer, where non–uniformity in the surface is most likely to occur. Figure 3.1f shows the transition in color from an inner, good region (dark) to an outer, bad region (cloudy). Stay away from regions which has spots/pimples that cannot be attributed to holes in the aluminum. To check the latter we use an atomic force microscope to image the pimples. The dots in the photo in e. g. Figure 3.1c and 3.1d are benign holes in the aluminum surface, because their depth was commensurate with thickness of aluminum. As long as a device did not have the active region within a few microns of such a hole, many successful devices (i. e. with superconducting properties) were fabricated in these regions.

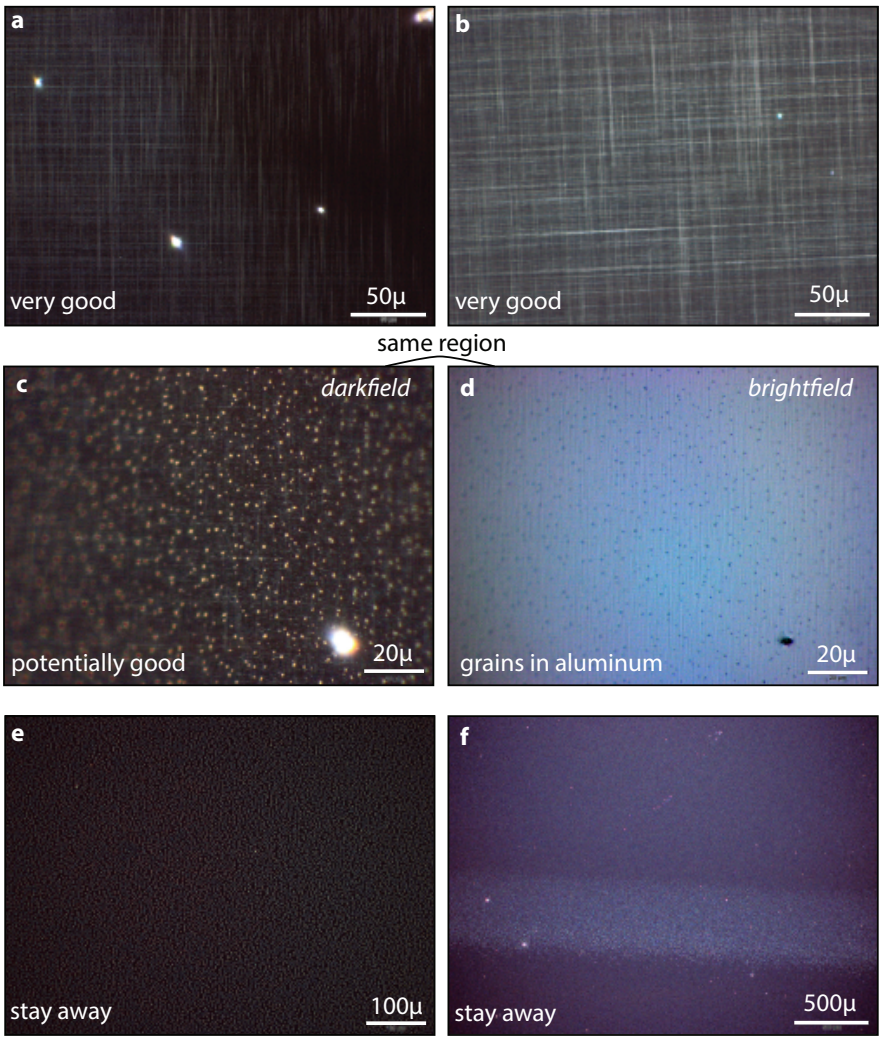

FIGURE 3.1: **a** and **b**, good surfaces showing hatched pattern indicating that the strain from growing lattice mismatched compounds is relieved systematically, which usually entails high(er) quality 2DEG. **c** and **d**, a region shown in both darkfield (with pimples) and brightfield, where the pimples look like holes in aluminum film. This can be double–checked with AFM. **e** and **f**, two bad regions with pimples and cloudy surface indicative of an arsenic deficient surface, which can lead to leakage paths and metallic conduction.

3.1.2 *The virtue of a stable schematic*

Prototyping and developing devices is an integral part of many experiments in mesoscopic low–temperature quantum transport. In order to stay efficient it pays of to plan the fabrication in a consistent way, that will not require starting from scratch when a device design has to be updated. We found that a stable solution was to use a template for alignment marks and ohmic contacts, and relegating all flexibility to the inner parts of the device. Figure 3.2a shows the alignment–marker and mesa template used for all our 2.5×5 mm chips. The template has an abundance of alignment marks which often proved useful, and has room for 19 4–terminal devices. The

spacing between devices is optimized to allow room for routing of gates in a subsequent step. The bondpads are 100 μm wide, which is close to the footprint of the bonder with the settings needed to punch through the 40 nm isolating Al_2O_3 layer (details in Section 3.1.7). Using this template,

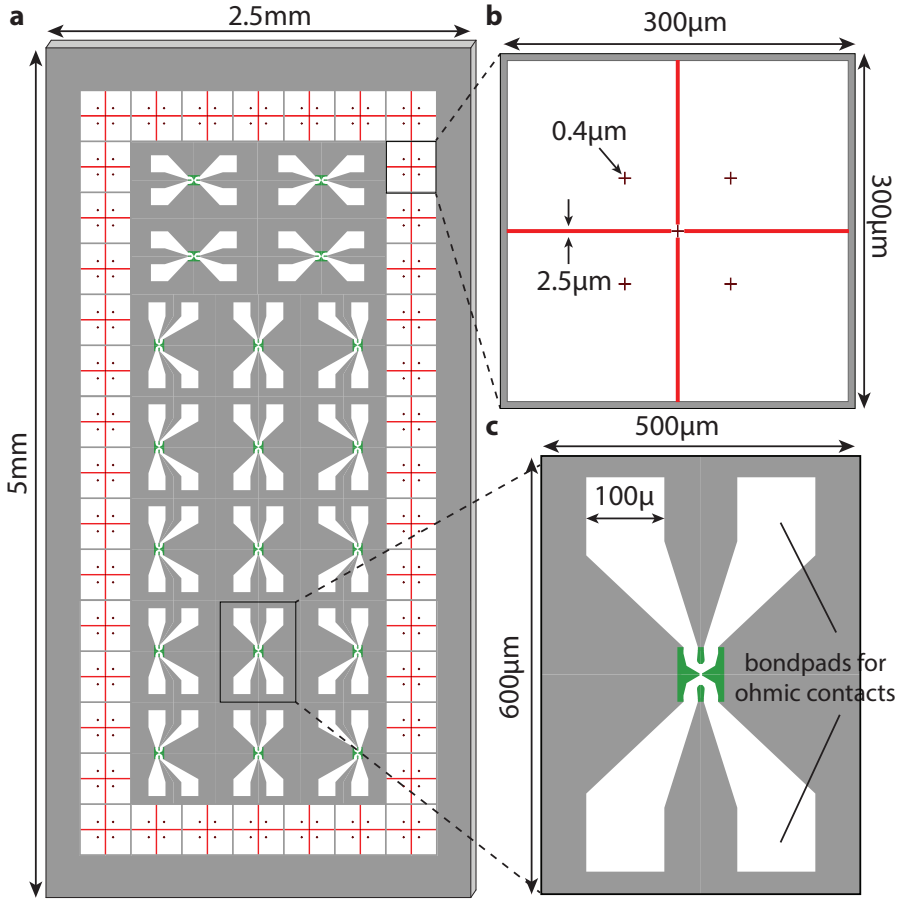

FIGURE 3.2: **a**, Template layout for a full 2.5 × 5 mm chip. **b**, Zoom in showing details of alignment marker sizes. **c**, Zoom in showing the 4–terminal template device. Green and red regions exposed and etched using high definition settings from section 3.1.3 and gray regions exposed and etched using low definition settings.

variations in device design is implemented simply by changing the layer highlighted in green, while the remaining template is left identical. The larger alignment marks is placed with even spacings of 300 μm, making them easy to locate relative to each other. The smaller alignment marks are placed (45μ m, 45μ m) relative to the center of the larger alignment marks. The alternating shape of the contacts on the 4–terminal geometry is designed to keep the high–definition regions (shown in green) exactly centered in the write fields of the e–beam lithography system, using equally spaced writefields throughout the entire chip. The centering is needed to achieve maximal alignment accuracy. Using 4 point alignment registration we consistently achieve ∼30 nm overlay precision between different layers with these markers and this layout.

3.1.3 *Defining mesas and alignment marks*

After cleaving the chip, inspecting it for bad surface regions and preparing the design file, mesas and alignment markers are etched. For all the steps we use e–beam lithography due to the flexibility to allow for changes in geometry without waiting for a new photomask. The chips are cleaned and resist is spun as follows,

CLEAN: 2 min acetone (swirl chip) / 1 min IPA (swirl chip) / blowdry with N_2 / bake for 3 mins at 185 °C.

SPIN RESIST: PMMA A4, 4000 RPM, 45 seconds: Place chip centered in chuck and turn on vacuum. If chip is not centered properly the resist will be unevenly distributed, due to the small size of the chip and the size of edge beads. Start rotation and pause at 500 RPM. Before accelerating to 4000 RPM dispense ~ 2 drops of PMMA A4. Spin 45 seconds at 4000 RPM. Bake for 3 mins at 185°C.

Inspect the chip under a microscope to make sure the resist is uniform (no color gradient) in the entire active region of the chip. If resist not uniform, clean chip and start over. For stripping resist I like to start with 2 min swirl in dioxalene, followed by 2 min acetone and 1 min IPA. Respin until resist is uniform. Before proceeding to the e–beam system make sure resist has not crept underneath the chip during spinning. An underside with PMMA chunks will lead to uneven loading in the e–beam system and bad exposures / bad alignment. Scratch any chunks off with a scalpel (carefully). The e–beam lithography exposure is split into two parts, one for the inner regions of the devices and the alignment marks, and one for the big features. Load chip in load lock and check that chip is even by gently pushing on it in the corner and check that the position of the ceiling lights refracted from the surface does not change as you push down (indicating the chip is slightly tilted). If it does, check underside for PMMA residues and scratch with scalpel as necessary. With chip properly loaded, these settings are used for the exposure

E–BEAM LITHOGRAPHY – HIGH DEFINITION: $I = 500$ pA, writefield size = 300 μm (matching exactly the size of an alignment mark), 60.000 dots and dwell time of 0.4 μS/dot, corresponding to a dose of $= 800\mu$ C/cm^2.

E–BEAM LITHOGRAPHY – LOW DEFINITION: $I = 20$ nA, writefield size = 600 μm, 20.000 dots and a dwell time 0.36 μS/dot, corresponding to a dose $= 800\mu$ C/cm^2.

The doses used here nominally underexposes the PMMA, but because the exposed areas are large, the proximity effect will add dramatically to the effective dose. The chip is then developed and plasma cleaned to remove any leftover resist residues

DEVELOP: 60 second swirl in MIBK:IPA (1:3) followed by 20 second swirl in IPA and blowdry with N_2.

PLASMA: 60 second plasma ash, removing approximately 15 nm PMMA.

Figure 3.3a shows the surface of a chip after finished plasma ashing. The resist edge bead is visible as a discoloration of the resist close to the right edge. After plasma ashing the chip is ready for etching the mesas, which is a 3–step process: Aluminum etch, followed by mesa etch, followed by another aluminum etch.

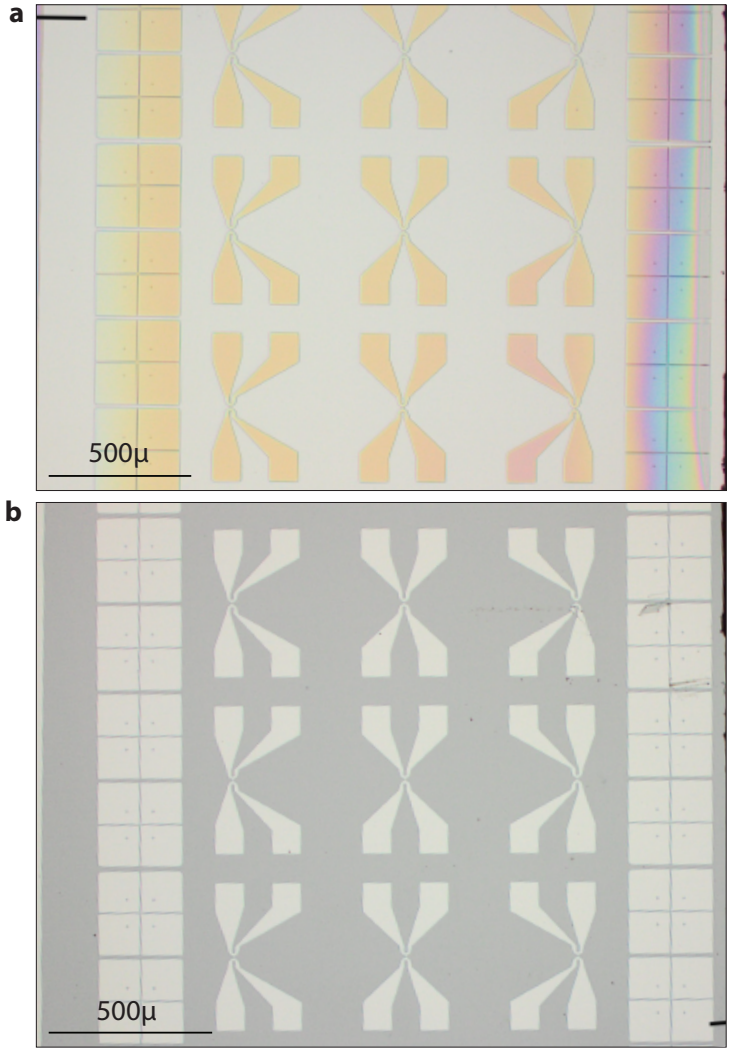

FIGURE 3.3: **a**, Mesa etch pattern after e–beam exposure, develop and plasma ashing. **b**, Mesa pattern after etching and stripping resist.

PREPARE ETCH: For the aluminum etch we use Aluminum Etchant Type D from Transene. Pour into two small (50 mL) plastic beakers and set both into 50 °C hotbath. Let it thermalize while the mesa etch

mixture is being prepared. The mesa etch has an approximate rate 0.5 nm/second, and is a variation on a standard III-V etch:

H_2O	:	citric acid	:	H_3PO_4	:	H_2O_2
220	:	55	:	3	:	3

The H_2O_2 acts as an oxidizing agent and H_3PO_4 (38%) binds the oxidized surface. The citric acid acts as a surfactant that helps replenish fresh etch close to the active regions. Figure 3.5 shows SEM image of mesa etched with, and without, added citric acid added to the etchant. The mix is created by adding 220 mL H_2O to a $\sim$ 750 mL beaker placed on a magnet stirrer. The citric acid is mixed (1M home mixed) and 55 mL is added to the large beaker with water in. Turn on magnet stirrer. Get the H_2O_2 (30% by weight) out of the chemicals refrigerator. H_2O_2 should be stored in a cool, dark space due to its volatile nature and the relative ease with which it decomposes into water and oxygen. Never use H_2O_2 that has been opened for more than $>$ 4 weeks or left out in light (you'll waste a lot of time trouble shooting your etch, like we did). Add 3mL H_3PO_4 to the mixture, use a 5mL measurement beaker and bottom of miniscus should be level with 3 mL indicator. Finally add H_2O_2 and cover mixture with lid. Put H_2O_2 back in refrigerator and clean up. The aluminum Etch Type D should now be 50 °C. Measure with a thermometer, it should be within $\pm$1.5 °C. The rate of the aluminum etch is highly dependent on the temperature, so correct temperature is critical [52].

ETCH: The following steps were developed by painstaking trial–and-error, and deviation has lead to (among other bad things): Redeposition of etched material on chip, bad definition of the mesa edges, and overhanging aluminum flaps making subsequent gate–deposition very hard. I encourage following the steps diligently, and moving efficiently. Figure 3.4 outlines the 10 steps discussed in detail below.

1. 10 second aluminum etch. Use acid tweezer and swirl carefully.
2. 20 second MQ water, swirl vigorously. Keep MQ beaker in the hot bath next to beaker with aluminum etch, so the chip is exposed to air for as short a time as possible, while moving between beakers.
3. 40 second fresh MQ water in a large beaker next to hot bath. After swirling for $\sim$20 s, carefully place chip on bottom of beaker and replace acid tweezer with standard carbon-tipped tweezer, for better grip in following steps.
4. Blowdry thoroughly with N_2, then dry tweezer with cloth and N_2, and finally blowdry chip again.
5. 480 seconds etching in mesa etch. Keep magnet stirrer on at speed 4. Swirl with frequency $\sim$ 1 Hz in a figure "∞" motion and hold chip approximately perpendicular to the bottom of the

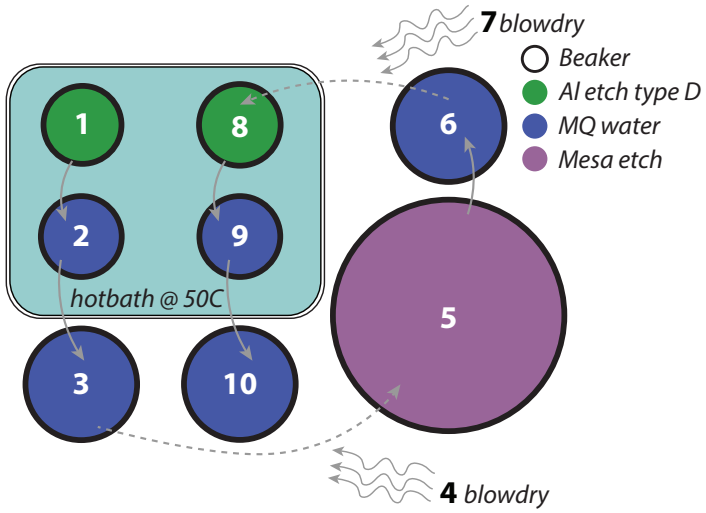

FIGURE 3.4: Cartoon showing the 10 steps in mesa etching

beaker. This lets the etchant attack surface uniformly, instead of skating along surface.

6. 40 second dunk and swirl in MQ.
7. Blowdry thoroughly with N_2, then dry tweezer with cloth and N_2 and finally blowdry chip again.

   The mesa etchant does not etch the aluminum, so to remove overhanging aluminum flaps, the chip is once again etched in Aluminum etchant Type D. Pick up chip with acid tweezer and finally go through:
8. 10 second aluminum etch (again, swirl carefully).
9. 20 second MQ water in same hotbath, swirl vigorously.
10. 40 second MQ water while swirling.
11. Same 3–step blowdry as after other etch steps.

RESIST STRIPPING: Finally, strip the resist mask using $\sim$50 °C acetone for 3 mins, followed by 1 min IPA and blowdry.

Figure 3.3b shows a typical mesa surface after the three etch steps outlined above. Inspecting the etched mesa in a microscope is critical: If there are halos around the edge of the mesa, if the edge is jagged or cloudy, it is an indication that something went wrong with the mesa etch, and should be inspected using SEM and AFM. The height of the mesa is measured in a profilometer. The mesas should be approximately $h = 240\ \text{nm} \pm 10\ \text{nm}$.

3.1.4 *Etching aluminum*

A chip with the etched mesas is cleaned and spun in the same way as when preparing for mesa etching, see section 3.1.3.

E–BEAM LITHOGRAPHY: $I = 500$ pA, writefield size = 300μ m, 60.000 dots and dwell time of 0.6μ S/dot, corresponding to a dose of 1200μ C/cm^2. The dose is increased relative to the exposure for mesas. This is because the area to be exposed is significantly smaller, so proximity effect will play a less pronounced role. I recommend running a dose– and etch–test when developing recipes for radically different aluminum etch windows.

DEVELOP: 60 second swirl in MIBK:IPA (1 : 3) followed by 20 second swirl in IPA and blowdry with N_2.

PLASMA: 60 second plasma ashing, removing approximately 15nm PMMA.

ETCH: Prepare two small beakers with Transene Aluminum Etchant Type D and submerge both in 50 °C hotbath. Allow $\sim$5 minutes to thermalize. Measure temperature with thermometer, should be 50 °C $\pm$1.5 °C. Prepare two beakers (one small, one large) with MQ water and submerge the small in the hotbath next to aluminum etches.

1. 5 second with acid tweezer in beaker 1 with aluminum etchant. Swirl carefully.
2. Quickly switch to next beaker with aluminum etchant and swirl another 5 seconds.
3. Dip into 50mL beaker with MQ water in hotbath and take care to minimize exposure to air. Swirl for 10 seconds.
4. Move chip into large 100mL beaker with plenty MQ water. Swirl for 20 seconds, place chip on bottom and replace tweezer with standard carbon–tipped version. Swirl $\sim$40 seconds.
5. Three step blowdry: Blowdry chip, dry tweezer with wipe and blowdry, and finally blowdry chip again.

RESIST STRIPPING: Strip remaining resist using $\sim$50°C acetone for 3 mins, followed by 1 min IPA and blowdry.

Douple–dipping in the aluminum etchant yielded cleaner sample surfaces when inspected by SEM after etching. Figure 3.5 shows SEM images of SNS devices where we compare a device etched using Aluminum Etch Type D and a device etched using AZ400K. The latter is a photoresist developer that is commonly used as aluminum etching agent. The addition of citric acid to the mesa etch, and using Al Etch Type D, instead of AZ400K, proved crucial for our fabrication of small (< 1 μm) devices.

3.1.5 *Insulator deposition*

The chip is cleaned using standard solvent clean just prior to being placed in an atomic layer deposition (Cambridge Nanotech Savannah ALD) machine. We use 400 pulses of trimethylaluminum (TMA) with H_2O as oxidizing agent, which results in $\sim$ 40 nm Al_2O_3 oxide layer. It's recommended

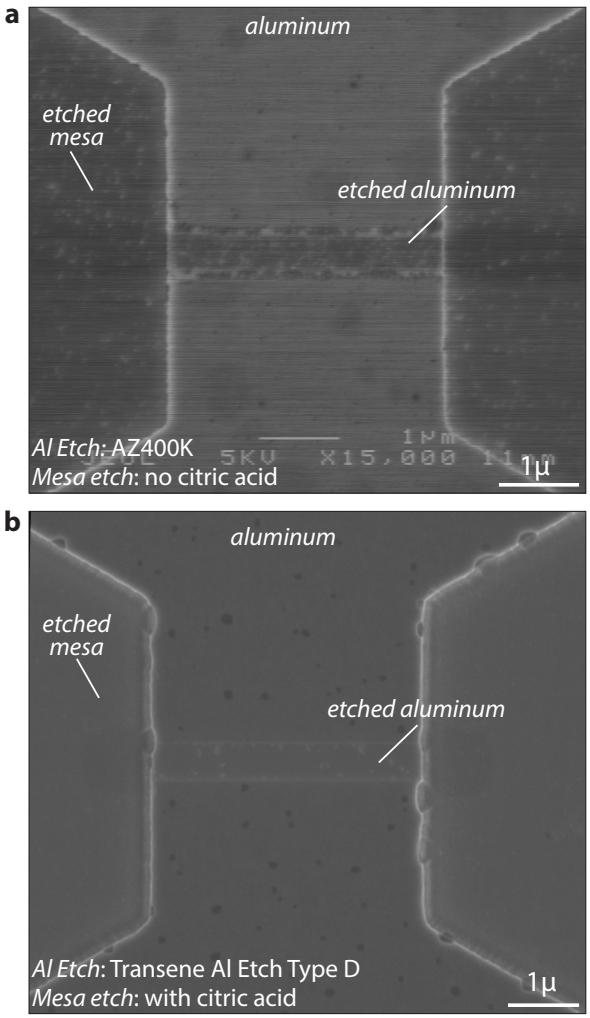

FIGURE 3.5: **a**, SNS junction using mesa etch recipe but without citric acid added. Aluminum etched with AZ400K photoresist developer. **b**, Mesa etch with added citric acid and aluminum etched with Aluminum Etchant Type D from Transene.

to gently pushing down on the ALD lid while starting to pump out the chamber. This reduces the likelihood of the chip flipping around inside the chamber, when the vacuum (rather violently) pulls the lid completely shut. A wait time of 60 seconds between each pulse allows proper purging of the chamber between TMA and H_2O pulses.

In relation to depositing the insulator, we pause to discuss the greatest unsolved fabrication mystery (and one of the biggest time sinks) throughout working with these wafers: After finishing a chip (mesa etch, aluminum etch, insulator deposition, gate deposition) we test the electrical contact and isolation of the gates in a 4 K liquid helium dunker setup. If the mesa etch–depth was $h \lesssim 200$ nm two otherwise disconnected mesas would be electrically connected to each other with $R \approx 2\,\mathrm{k}\Omega$. This parallel conduction path only appeared *after* deposition of insulator. Javad Shabani, the mate-

rials grower, made test devices at UC Santa Barbara with $h \lesssim 200$ nm and did not observe the same parallel conduction path after Al_2O_3 deposition. Even without a plausible chemical reason, we suspected some aspect of the insulator deposition process to be the cause of this parallel conduction path. For posterity, we list the amendments we tried to the ALD deposition to overcome this obstacle:

- High-temperature (200 °C) Al_2O_3, which allows us to significantly reduce the pulse times, leading to shorter exposure of the chip to elevated temperatures in the ALD machine.
- Dip in ammonium polysulphide to passivate the surface prior to loading chip into ALD machine.
- Replacing TMA with Tetrakis(ethylmethylamido)hafnium(IV) to form hafnium oxide (HfO_2), another commonly used insulator, in case leakage was related to the TMA. HfO_2 deposited at 90°C.
- Low-temperature HfO_2 (40°C) using Argon as carrier gas.
- Low-temperature HfO_2 with Argon as carrier gas and IPA instead of H_2O as oxidizing agent.
- Dip in buffered oxide etch (to remove native oxide) followed by dip in dilute ammonium hydroxide to passivate surface prior to ALD.
- Sputter deposition of Si_3N_4, to completely avoid the ALD process.

All of the tests above yielded same result: Disconnected mesas had a parallel conduction path with $R \approx 2$ kΩ. The problem was ultimately resolved not by changing the ALD process, but by etching deeper $h \gtrsim 200$ nm. As of writing, it is still unresolved what caused this parallel conduction path, or why it was not present in samples prepared using the ALD machine at UC Santa Barbara. The only outstanding difference is that the UCSB machine was plasma–based ALD, while the ALD machine at QDev is thermal ALD.

3.1.6 *Deposition of gates*

Finally the metallic gates can be deposited. The process is split into two steps. First step is depositing the fine structures that forms the innermost regions of the gates, followed by a second (thicker) metallic layer that forms bondpads and outer region of gates. The process cannot be done in a single step, since the gates need to crawl up onto the mesa ($h \gtrsim 250$ nm), while still having small ($\sim$100 nm) features.

Inner gate regions

CLEAN: 2–solvent clean: 2 minutes in acetone, 1 minute in IPA and 3 minutes bake at 185 °C.

SPIN RESIST: PMMA A4, deposited in the same way as for mesa etch, see section 3.1.3. Spin at 4000RPM for 45 seconds.

E–BEAM LITHOGRAPHY: $I = 500$ pA, writefield size = 300 μm, 60.000 dots and dwell time of 0.62 μS/dot, corresponding to 1240 μC/cm^2.

DEVELOP: 60s MIBK:IPA (1:3) followed by 20 sec IPA and then thorough blowdry with N_2.

PLASMA ASH: 45 seconds, approximately equivalent to 12 nm PMMA removed.

METAL EVAPORATION:

- 5 nm titanium at an angle of 10° with a rotation of 50 RPM.
- 20 nm gold at an angle of 10° with a rotation of 50 RPM.
- 30 nm gold at an angle of 0° with a rotation of 50 RPM.

LIFTOFF: Over night in N-Methyl-2-pyrrolidone (commonly referred to as NMP). Scratch the corner of the chip with a syringe to help the NMP crawl under the film. This relatively delicate lift off is necessary since the resist is not a bilayer stack and metal is deposited at an angle, making it harder to lift off.

Outer gate regions

CLEAN: 2–solvent clean as for the inner gates.

SPIN RESIST: Deposit resist using dynamic deposition, same as for all other e–beam steps, this time with a bilayer:

1. EL-9, 4000 RPM for 45 seconds
2. Bake for 3 minutes at 185°C.
3. PMMA-A4, 4000 RPM for 45 seconds
4. Bake for 3 minutes at 185°C.

E–BEAM LITHOGRAPHY: $I = 20$nA, writefield size = 600 μm, 20.000 dots and dwell time 0.36 μS/dot, corresponding to 800μC/cm^2.

DEVELOP: 60 seconds in MIBK:IPA (1:3) followed by 20 second IPA and then thoroughly blowdry with N_2.

PLASMA ASH: 45 seconds equivalent to roughly 12nm PMMA

METAL EVAPORATION: 5 nm titanium at an angle of 10° with a rotation of 50 RPM / 50 nm gold at an angle of 10° with a rotation of 50 RPM / 130 nm gold at an angle of 0° with a rotation of 50 RPM / 20 nm gold at an angle of 10° with a rotation of 50 RPM.

LIFTOFF: $\sim$4 hours in 80 °C NMP

Figure 3.6 shows a finalized chip, fabricated using the steps outlined above. Data on two devices from the chip in Figure 3.6 is the subject of Chapters 4 and 5, respectively.

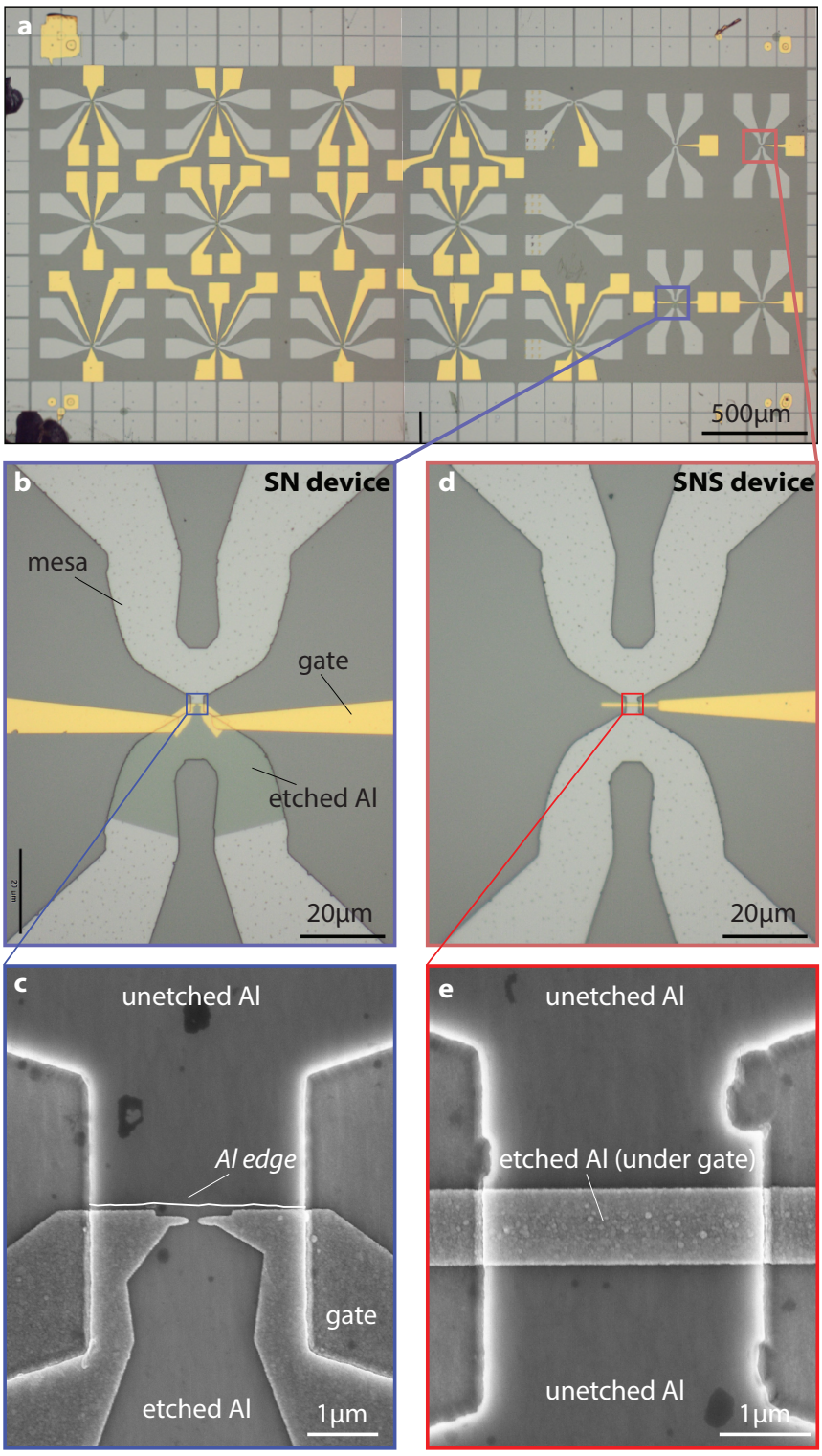

FIGURE 3.6: **a**, Full 2.5 × 5 mm chip with 19 devices. **b**, **c**, Optical and SEM zoom of the SN junction highlighted in blue in **a**. The superconducting properties of this device is the subject of Chapter 4. The double–layer gate metal deposition is visible as a slight change in the intensity of yellow close to the mesa. **d**, **e**, Optical and SEM zoom of the SNS device highlighted in red in **a**. The supercurrent and multiple Andreev reflections in this device is studied in detail in Chapter 5.

3.1.7 *Wire bonding and prepping for cooldown*

To mount the chip, we use the new QDev sample boards developed by Morten Madsen and Ferdinand Kuemmeth. The boards were developed to utilize 48 DC lines. Figure 3.7c shows a QDev sample board with a chip mounted. The chip is glued onto the QDev board with a drop of PMMA A4 and baked for 3 minutes at 185 °C in the cleanroom.

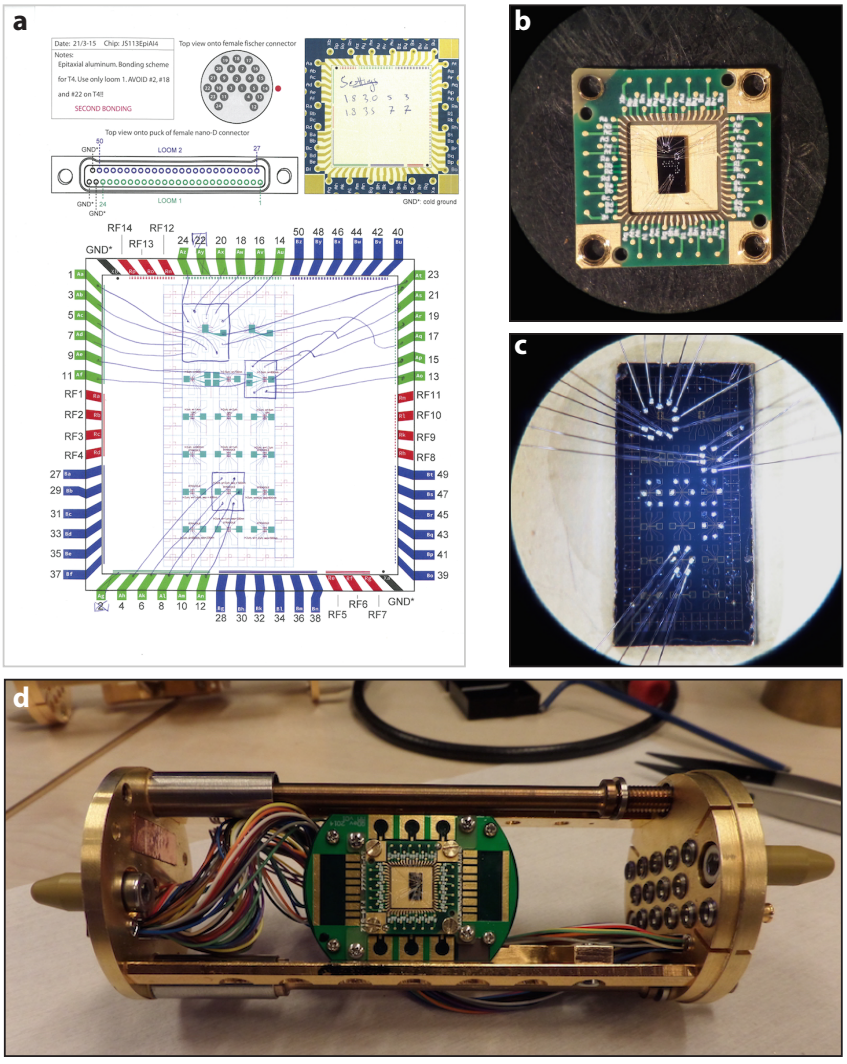

FIGURE 3.7: **a**, An example of a used pinout schematic for the device `JS113EpiAl4`. Only loom 1 was used (loom 2 had not been fitted in the fridge at the time of this device loading). A blank template is available on the QDev wiki page. **b**, **c**, Sample `JS113EpiAl4` bonded on QDev board. **d**, A sample mounted on the QDev board in a puck. Notice position of non–gold plated corner of the QDev board relative to the motherboard, this sets the orientation to match the pinout.

For bonding we used the settings shown in Table 3 on the bonder to ensure punching through the Al_2O_3. We developed a pinout sheet to assist in keeping track of line numbers and bonding, see Figure 3.7a (a blank template can be found on the QDev wiki page). After bonding we usually

	Search	Power	Time	Force
1st bond	1.8	3.0	5	3
2nd bond	1.8	3.5	7	7

TABLE 3: Settings used on wirebonder. The values for the first bond (made on the chip carrier) should just be set so the bonding is comfortable. The settings on 2nd bond are necessary to punch through Al_2O_3.

take optical images through a microscope as shown in Figure 3.7b and 3.7c, which is useful if troubleshooting is needed, after device is loaded.

Before the puck is loaded into the dilution unit we test the bonds at room temperature. This is done by loading the puck onto the puck tester, which is connected with a Fischer connector onto a test breakout box, see Figure 3.8. Using an AC current bias 2–terminal measurement the room temperature resistance of the ohmics is then measured. For an ohmic to be working at base temperature, it should have $R^{\text{2-T}}_{\text{room temp}} \lesssim 2\text{k}\Omega$. At base temperature the corresponding contact resistance would be between 0.5 kΩ and 1 kΩ. It is exceedingly helpful to perform this test, since it allows not just checking the ohmic contacts and bonds, but also ensuring the pinout scheme is correct prior to loading the chip in the fridge. I highly recommend doing it, no matter how tired you are when loading a device late at night.

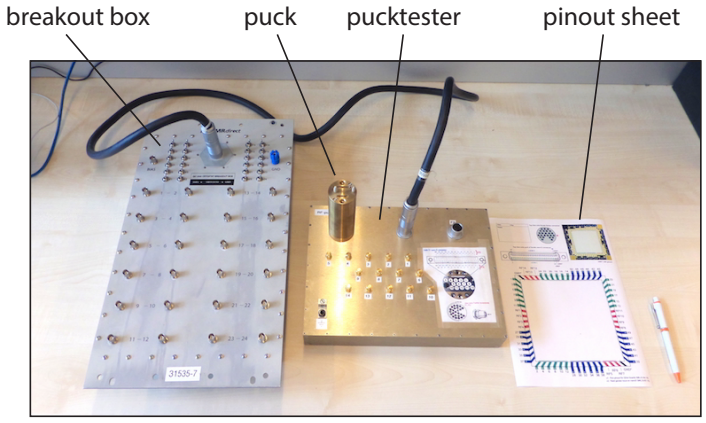

FIGURE 3.8: Puck tester with puck attached connected to a breakout box for room temperature tests before loading a device.

3.2 MEASUREMENT TECHNIQUES AND ELECTRONICS

All measurements reported in this thesis were done in a Triton cryofree dilution refrigerator with base temperatures $T_{\text{mc}} = 23$ mK, measured using ruthenium oxide temperature sensor anchored to the mixing chamber. The refrigerators are bottom-loaded He^3–He^4dilution units bought from Oxford Instruments. We'll refer to them simply as *fridges* throughout this section. We start with a brief review of the insides of a typical Triton fridge and how we have amended them for the low–frequency ($f < 100$ Hz) AC+DC

measurements performed in this thesis and then move to details of the measurement setup and electrical filtering in section 3.2.2.

3.2.1 *The guts of a Triton dilution unit*

The role of the refrigerator is to decrease the temperature of the sample until $k_B T$ is no longer destroying (or hiding) the quantum effects we are interested in, and offer a means to inject and collect electrical signals. Here, we briefly review the process of He^3–He^4dilution refrigeration. Details can be found in e.g. Pobells textbook [53]. Roughly, the cooling is achieved by a two stage process (see Figure 3.9): Precooling down to $T \sim 10$ K on the mixing chamber (eventually the coldest part of the fridge) by circulating a mixture of He^3–He^4 in the gas phase, which is thermalized by contact to a stage mechanically cooled to 4 K using a pulse tube cooler [54]. Once the mixing chamber reaches 10 K, a different cooling scheme is deployed. One of the many famous results on the properties of He^3 an He^4 is that even as $T \to 0$ K, they are still in liquid form and there is a finite solubility of the two liquids [53, 55]. Roughly speaking, the mixing of these two quantum liquids requires energy from the surroundings and cools the chamber containing the liquid (this is a gross simplification). This is a fundamentally quantum mechanical process that relies on the Bose and Fermi statistics of He^4 and He^3. By a series of heat exchangers and pumps, the He^3 from the dilute phase in He^4 is recirculated through the refrigerator and the cooling (dilution) process can run perpetually, see Figure 3.9b. What ultimately sets the temperature limit is the ability to thermally isolate the mixing chamber and requirements on flow rates in the He^3–He^4circuit. In practice, lower than $T = 10$ mK temperatures is not feasible using the He^3–He^4 dilution strategy [53].

The fridge is equipped with 2 looms of 12 twisted pair constantan cables, for a total of 48 lines usable for AC+DC measurements. There is also space for 14 coax lines, but none of them are used for our measurements. The coax lines are terminated at the mixing chamber. Due to the layout of the twisted pairs in the nano–D connectors, the DC lines are labeled 1–24 and 27–50.

The temperature in the sample is in general not the same as the temperature of the electrons in the electrical signal used to excite the sample, unless special care is taken. It's the electron temperature, T_e, that will set the thermal broadening of our experiments, so we should care about thermalization of the electrical lines. To cool the electrons, we thermalise the loom by tightly wrapping it around a copper post which is thermally anchored to the mixing chamber. The loom is fixed in place with dental floss and painted with GE varnish, see Figure 3.10c. The brackets containing the PCB boards with the electrical filters is also anchored to the mixing chamber, and will also contribute to thermalization. Figure 3.10c shows a schematic of the thermalization and filtering layout in the fridge used for the measurements

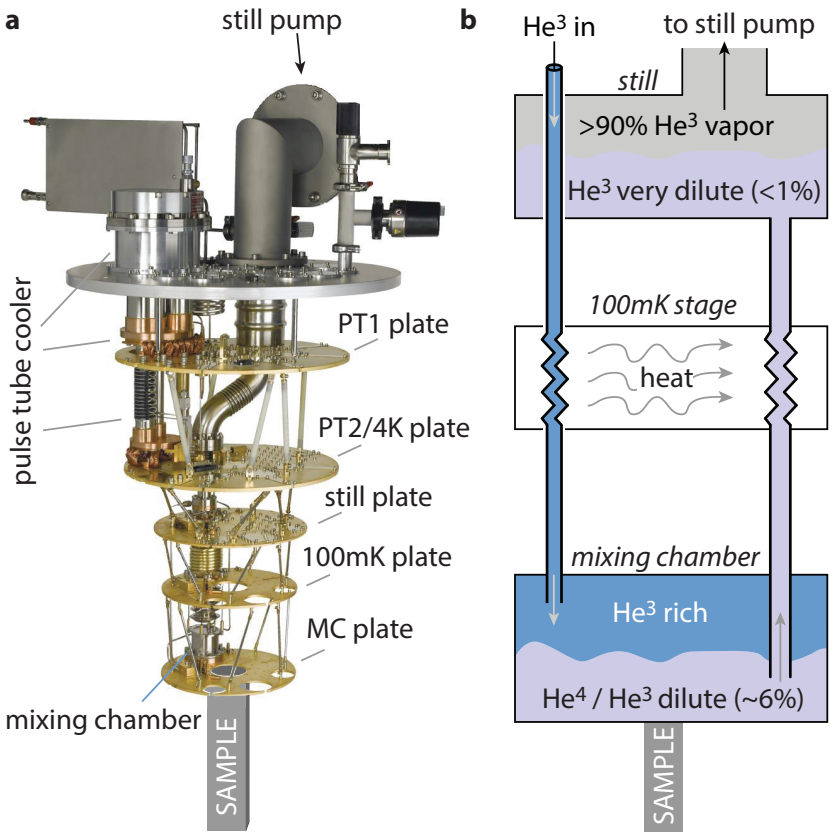

FIGURE 3.9: **a**, Picture of the inner parts of a Triton cryofree dilution refrigerator. This fridge does not have a coldfinger (indicated by gray box, where sample would be loaded) and is void of any electrical wiring. **b**, Rough schematic of the He^3–He^4 circulation system inside the fridge. Flow impedances and details of the design is omitted.

reported in Chapters 4 and 5. The electron temperature was measured using Coulomb blockade thermometry on a quantum dot in GeSi nanowires to be $T_e = 100$ mK (measurements performed by the previous user of the fridge). The filtering consists of two homebuilt 3–stage filter boxes developed by Ferdinand Kuemmeth (the so–called *RF PCB filters* and *RC PCB filters*). The capacitors and resistors in the RC circuit are chosen to have a reasonable range in cutoff-frequency when using a large bias resistor, while the π filters in the RF box are an off-the-shelf item from Mini–Circuits. The RC filter has a cutoff frequency $f_c = 1/2\pi RC \approx 15.6$ kHz, and the π filters are 80 MHz, 1450 Mhz and 5000 MHz 7–pole low–pass filters, respectively. Figure 3.10d shows a schematic of the layout of the filters. Finally we note that the high–frequency filters are necessary to measure a sharp transition to the superconducting branch in IV curves in the SNS geometry discussed in Chapter 5, indicating that high–frequency noise needs to be filtered.

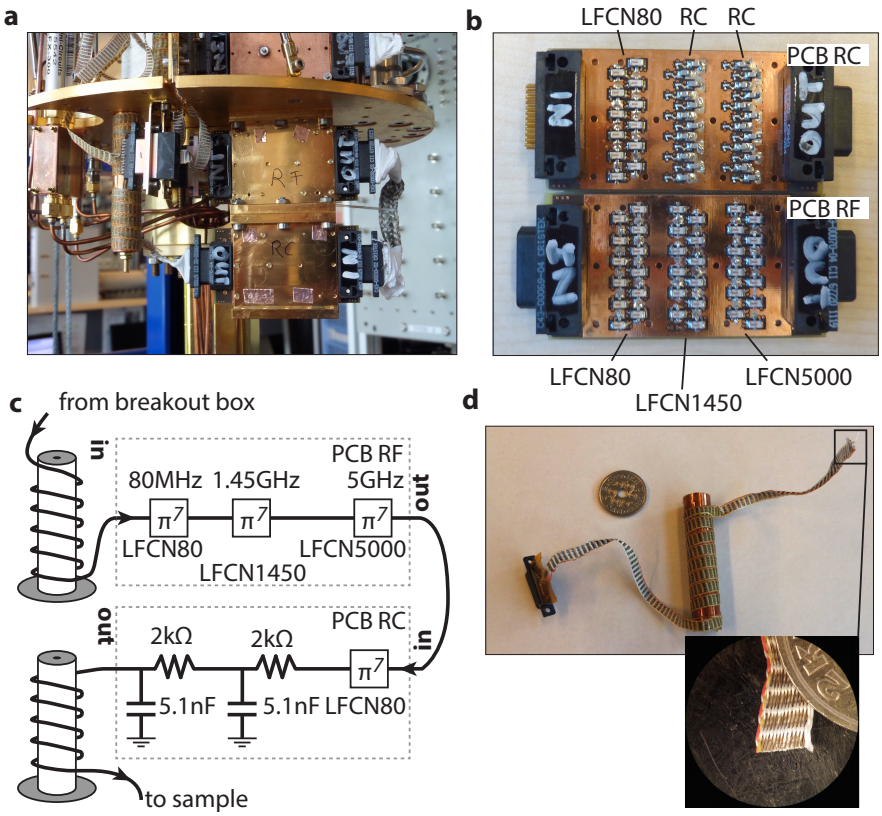

FIGURE 3.10: **a**, Picture of ferdi RF and ferdi RC filters inside gold plated copper brackets thermally anchored to the mixing chamber. **b**, the PCB boards inside the RF and RC filters, showing the 3–stage structure of each filter. **c**, diagram of thermalization of loom (indicated in thick black) via copper posts and filters. **d**, image of the copper post with loom wound around it. Zoomin shows the 12 twisted pair cables in the loom.

3.2.2 *Measurement strategies*

Here we briefly review the measurement techniques and strategies used for the measurements reported in Chapters 4 and 5. All measurements are done in a 4–terminal setup, except for cases where a device is operated in the very pinched off regime, with a resistance $R \approx 10\ \mathrm{M}\Omega \approx 0.01 G_0^{-1}$ (as is the case for the data in Figure 4.10). Such larges resistances are comparable to the input impedance on the voltage preamplifiers, so current will start flowing to the voltage probes, instead of the (virtual) ground. In this case we use a 2–terminal DC measurement.

Figure 3.11a show the 4–terminal measurement setup used for measuring the quantum point contact. The setup is operated in voltage–bias, using a home–built IV converter that applies the bias V_{out} symmetrically on either contact, and simultaneously measures the resulting current through both contacts. An AC signal, sourced from an Stanford Research SR830 lockin amplifier, and a DC signal, sourced from a DAC, is applied simultaneously. The AC component is typically $V_{out}^{AC} \sim 5\ \mu$eV. This should be compared to the superconducting gap, with typical energy scale $\Delta \sim 200\mu$ eV. In light of this,

the value for $V_{\text{out}}^{\text{AC}}$ is a trade–off between signal strength (which gets better with increasing excitation voltage) and broadening (which is proportional to $V_{\text{out}}^{\text{AC}}$), with the overall signal scale set by Δ. The lockin is not comfortable outputting such a small excitation, so we use a homebuilt resistive divider with a factor 1/100.000. All measurements in the voltage bias mode are performed at $f_{\text{out}} \sim 17$ Hz, low enough to not worry about phase shift induced by the RC filters, and high enough to maintain a reasonably low integration time.

For the DC voltage supply, we use a DAC with a range of ± 10 V and 16 bits digitization, leading to resolution $\delta \text{V} = (20 \text{ V})/2^{16} = 0.3$ mV. To increase resolution every second channel on the DAC is used as a fine channel, using a built–in divider, leading to a resolution of $\delta V = 3$ μV. Since the typical scale for the voltage bias measurements is 200μV, we use a homebuilt 1/1.000 divider to increase resolution and avoid running the DAC at the lower edge of its resolution. The differential voltage is amplified by a factor 100 from the preamplifiers, and the current is measured with a feedback resistor $R_{\text{feedback}} = 100$ MΩ. Measuring the DC component simultaneously is crucial when performing finite source–drain bias measurements, and its significance will be discussed in chapter 4. The differential conductance $G = dI/dV$ is found by digitally dividing the AC current readout from the lockin measuring output on the current preamplifier, with the differential voltage from the lockin measuring output from the voltage preamplifier.

For the measurements of the supercurrent in Chapter 5 we use a current bias setup. Since the superconducting state is defined by its absence of a voltage drop across the junction, voltage bias measurements are not suitable. The setup is shown in Figure 3.11b. The critical current at which the SNS junctions measured in Chapter 5 switches to the normal state is $I_c \approx 2$ μA. With this typical current scale in mind we use a 440 kΩ bias resistor on the DC line and a 500 MΩbias resistor with a 2.5 V excitation on the AC current, leading to $I_{\text{AC}} = 5$ nA. In the current bias setup the drain electrode is set to ground to minimize noise, but can be hooked up to a current preamp for diagnosing potential issues and verifying that the current source is operating as expected. The AC voltage is measured to calculate the differential resistance and the DC voltage drop is measured to correctly scale the multiple Andreev reflections signatures (see Chapter 5 for details).

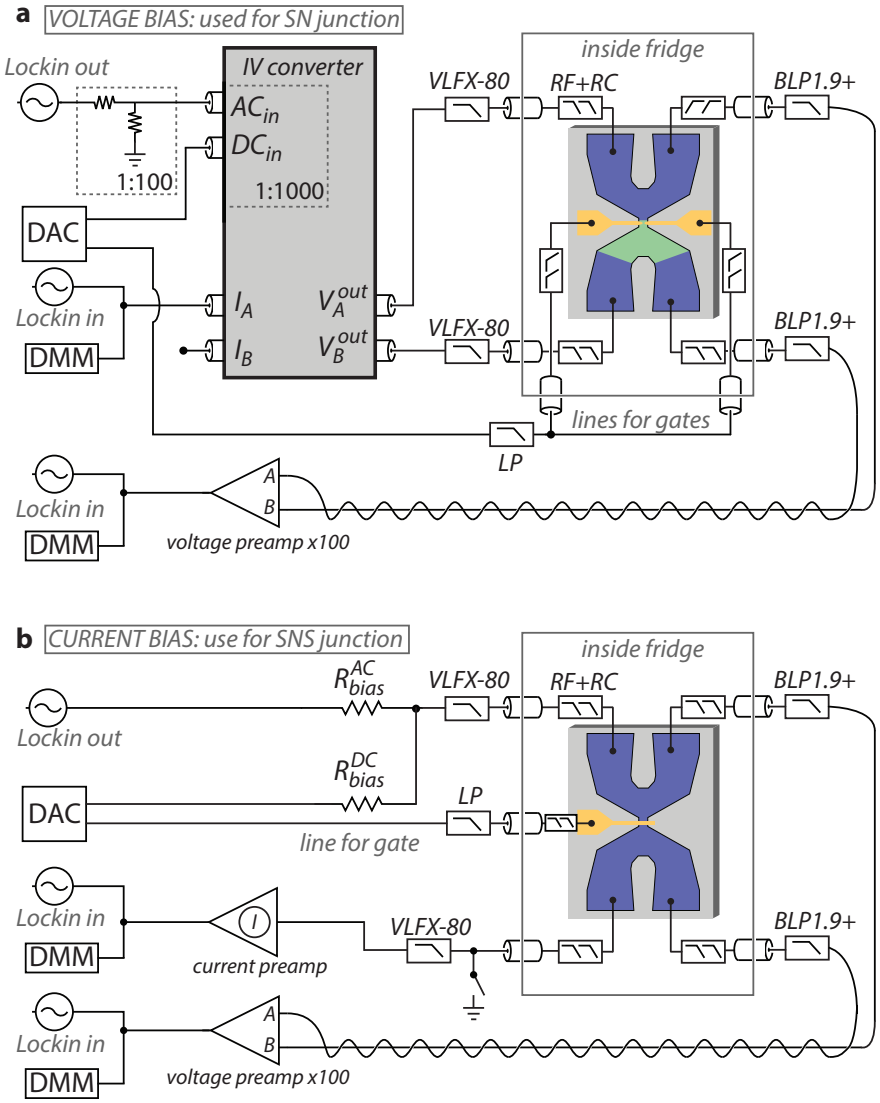

FIGURE 3.11: **a**, Setup for 4–terminal voltage bias measurement using homebuilt IV converter with symmetric biasing. The floating connection marked I_B is the current into line B, which is nominally identical to current in line A (unless there is electrical leakage in device). The I_B line is useful for troubleshooting but is usually kept disconnected. The RF+RC filter is the PCB filters discussed in the main text, while the filter marked 'VLFX-80' is an 80 MHz off-the-shelf filter from Mini–Circuits. We found the measurements more quiet with this added filter at room temperature. Finally, the BLP1.9+ is 1.9 MHz low pass filter and the filter marked 'LP' is a low pass RC filter with an RC time 150 ms filter used for DC voltages on the gates. **b**, Current bias 4–terminal setup used to measure the superconducting state of the SNS geometry. The readout on the current preamp is not necessary, but can be useful for troubleshooting. Most of the time we simply ground this contact to minimize noise. The resistance of the bias resistors is chosen based on the superconducting properties of the junction being measured.

Part II

SUPERCONDUCTING PROPERTIES OF THE EPITAXIAL AL/INAS QUANTUM WELL

In this part we dive into the transport measurements of the superconducting properties of the 2D electron gas. Chapter 4 is devoted to quantum point contact spectroscopy of a single SN interface and in Chapter 5 we investigate the supercurrent carrying and finite–bias properties of an SNS geometry.

4

THE ANDREEV ENHANCED QUANTUM POINT CONTACT

In this chapter we study the properties of the InAs 2DEG coupled to the aluminum grown *in situ*. The InAs inherits properties of the superconductor via Andreev reflection when electrons/holes impinge on the aluminum interface. We start this chapter by reviewing this proximity effect, and introduce the Blonder–Tinkham–Klapwijk formalism for understanding the NS interface. A tunnel probe can be used to measure the local density of states in the 2DEG, and we derive explicitly how the tunnel probe behaves when placed proximal to an NS interface. With these insights we present data on a QPC that can be continually tuned from approximately unity transmission of a single mode and down to tunneling regime, where it is used as a probe of the local density of states in the epi–Al/InAs. We observe doubling of quantization through the QPC (step size $4e^2/h$) in the one–channel limit, and strongly suppressed conductance (the hard gap) when the QPC is used to probe the local density of states, due to the proximity to aluminum.

4.1 THE SUPERCONDUCTOR/SEMICONDUCTOR INTERFACE

When a normal metal (semiconductor) is placed proximal to a superconductor, the properties of both materials can change dramatically. Here we focus on how states in the normal metal are affected by the proximity to the superconductor. Consider an electron with energy $E \gtrsim \mu$ impingent on the NS interface from the normal metal. The fermi energies of the normal metal and superconductor will align, and for $E < \Delta$ there are no quasiparticle states available inside the superconductor. Since there is no barrier at the interface (in this simple model, we'll change this later), and no quasiparticle states available, there is no option for the electron to dump its momentum to change the sign of its wavector and undergo a scattering event. However, the superconductor can accept Cooper pairs at the Fermi energy. If

the normal metal donates an extra electron with $-k\uparrow$ along with the original electron, the superconductor can accept the pair $(k\uparrow, -k\downarrow)$. Due to momentum conservation, this process will leave the fermi sea with a net momentum $+k$. So instead of the normal metal injecting an extra electron into the superconductor, we can think of the original electron retroreflected as a hole with $+k$ momenta. This process is sketched in Figure 4.1a and 4.1b and is known as *Andreev reflection* [56]. Because the group velocity of a hole is opposite to that of its wavevector, the hole will traverse the same path back as the incident electron. Since a charge $2e$ was transfered into the superconductor, Andreev reflection increases the conductance below the gap. If the impingent electron has $E > \Delta$ there will be normal scattering in addition to Andreev reflection.

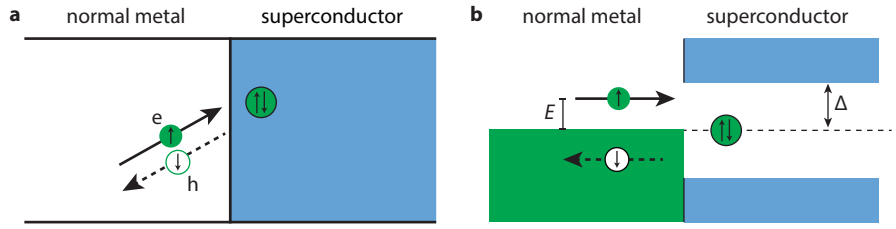

FIGURE 4.1: **a**, Real space schematic of the Andreev reflection process. **b**, Energy space schematic of electron with energy $E > \mu$ but $E < \Delta$ being retroreflected as a hole while a Cooper pair is formed in the superconductor.

4.1.1 *The Blonder–Tinkham–Klapwijk formalism*

The situation outlined above is of course idealized. It is usually the case, that when a semiconductor is in proximity to a superconductor, the interface between the two materials will not be ideal (i. e. not every incident electron is retroreflected as a hole). Two effects can contribute to degrading the interface:

- The density in the semiconductor is in general lower than in the superconductor. This can lead to a fermi velocity mismatch of the carriers.
- The interface between the two materials can (and will) be degraded due to processing of the sample.

These modifications to the idealized case were studied in the seminal paper by Blonder, Tinkham & Klapwijk [57]. The same results were independently found by Zaitsev [58] and Arnold [59], by starting from a microscopic theory. The BTK derivation provides an intuitive and elegant picture, which we outline below.

The interface degradation is modeled by a δ–function located at the interface. The Fermi velocity mismatch between the superconductor and the semiconductor is modeled by a potential step across the interface. The scalar

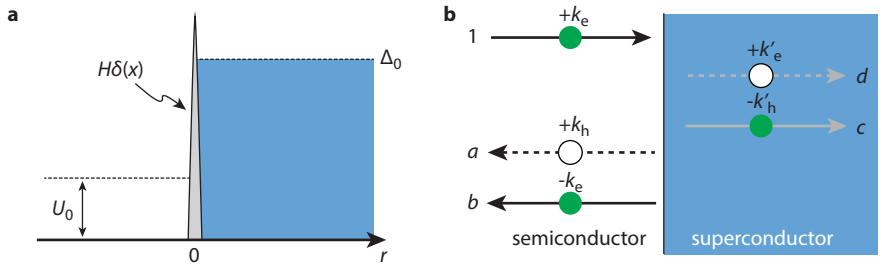

FIGURE 4.2: **a**, The more realistic picture of an SN interface with a degraded interface modeled by a δ–function and potential U_0 due to Fermi velocity mismatch. **b**, Definition of the plane–wave coefficients used in the BTK analysis of an SN interface.

potential in the Bogoliubov-de Gennes equation (2.14) is therefore modified to

$$U(r) = \underbrace{U_0\theta(-r)}_{\substack{\text{fermi velocity}\\ \text{mismatch}}} + \underbrace{H\delta(r)}_{\substack{\text{interface}\\ \text{transparency}}} \tag{4.1}$$

We will also assume that the pair potential increases in a steplike manner $\Delta(r) = \Delta_0 e^{-i\phi}\theta(r)$, where $\theta(r)$ is the step function. The scenario is sketched in Figure 4.2a. The strength of the the barrier at the interface can be recast in dimensionless units by introducing

$$Z = H\frac{m_e}{\hbar k_{Fs}} \tag{4.2}$$

The "height" of the barrier is given by Z. We will use Z synonymously with the quality of the SN interface, so that $Z = 0$ corresponds to perfect Andreev reflection.

An electron impingent on the super/semi interface now has four options: scatter as an electron, scatter as a hole (Andreev reflect), transmit as a (quasi) hole or transmit as a (quasi) electron. Using the plane–wave ansatz these options give rise to the following wavefunction

$$\Psi_{\text{incoming}} = \begin{pmatrix} 1 \\ 0 \end{pmatrix} e^{ik_e r} \tag{4.3a}$$

$$\Psi_{\text{reflected}} = a\begin{pmatrix} 0 \\ 1 \end{pmatrix} e^{ik_h r} + b\begin{pmatrix} 1 \\ 0 \end{pmatrix} e^{-ik_e r} \tag{4.3b}$$

$$\Psi_{\text{transmitted}} = c\begin{pmatrix} u \\ v \end{pmatrix} e^{ik'_e r} + d\begin{pmatrix} u \\ v \end{pmatrix} e^{-ik'_h r} \tag{4.3c}$$

The incoming/outgoing waves are shown in Figure 4.2b.

The wavenumbers for the electrons and holes can be found by considering the eigenenergies of the BdG equation, introduced back in Equation 2.20. Isolating k yields the four solutions

$$k_\tau = \pm\tfrac{1}{\hbar^2}\sqrt{2m(\mu - U_0 + \tau\sqrt{E^2-\Delta^2})}, \tag{4.4}$$

where $\tau = 1(-1)$ corresponds to solutions for electrons (holes). The wavenumbers for the planewaves are thus

$$k_\tau = \sqrt{k_{Fn}^2 + \tau E\tfrac{2m}{\hbar^2}} \quad , \quad k'_\tau = \sqrt{k_{Fs}^2 + \tau\sqrt{E^2-\Delta^2}\tfrac{2m}{\hbar^2}}, \tag{4.5}$$

where $k_{Fn} = \sqrt{\frac{2m}{\hbar^2}(\mu - U_0)}$ and $k_{Fs} = \sqrt{\frac{2m}{\hbar^2}\mu}$. For $E < \Delta$, k'_τ is imaginary, corresponding to evanescent waves in the superconductor. Imposing appropriate boundary conditions on the wavefunctions and wrangling Equations (4.3a)–(4.3c) sufficiently, allows the determination of the Andreev reflection probability $A(E) = a^*a$ and normal reflection probability $B(E) = b^*b$ [57, 1]. We quote the hard labor in Table 4.

	$A(E)$	$B(E)$
$Z = 0$		
$E < \Delta$	1	0
$E > \Delta$	$\frac{v_0^2}{u_0^2}$	0
$Z > 0$		
$E < \Delta$	$\frac{\Delta^2}{E^2+(\Delta^2-E^2)(1+2Z^2)^2}$	$1 - A(E)$
$E > \Delta$	$\frac{u_0^2 v_0^2}{\gamma^2}$	$\frac{(u_0^2-v_0^2)^2 Z^2(1+Z^2)}{\gamma^2}$

TABLE 4: The probability $A(E)$ of Andreev reflection and the probability $B(E)$ of normal reflection, for the case of ideal Andreev reflection $Z = 0$ and degraded interface $Z > 0$.

The factors v_0 and u_0 are given in Equations (2.18) and (2.19), and

$$\gamma = u_0^2 + \left(u_0^2 - v_0^2\right) Z^2 \tag{4.6}$$

and the Z–parameter is modified to an effective version, including Fermi velocity mismatch,

$$Z \to Z_{\text{eff}} = \sqrt{Z^2 + (1-r)^2/4r} \tag{4.7}$$

where $r = v_{Fn}/v_{Fs}$. This effective parameter Z_{eff} includes both the effects of interface degradation and Fermi velocity mismatch. From here on out, whenever we discuss the Z parameter, we'll have in mind the effective version, but without explicitly writing Z_{eff}. In Figure 4.3 the quantities $A(E)$ and $B(E)$ is plotted for several values of Z.

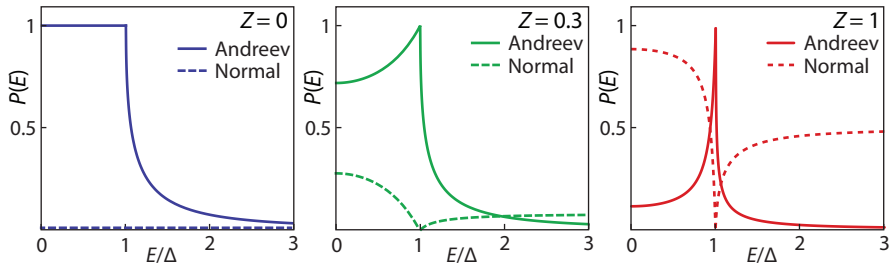

FIGURE 4.3: Probabilites of Andreev reflection and normal reflection as a function of energy of an incoming electron, for a few values of the barrier parameter Z

So far, the phase of the incoming electrons/outgoing holes have been ignored. The phase of the hole after Andreev of an electron is dependent on the energy of th incoming state, the superconducting gap, and the phase of the superconductor in the following way

$$\phi_h = \phi_e + \arccos(E/\Delta) + \phi_s \tag{4.8}$$

and similarly for a hole Andreev reflected into an electron:

$$\phi_e = \phi_h + \arccos(E/\Delta) - \phi_s \tag{4.9}$$

The significance of the phase properties of the Andreev reflection will become particularly important in the next chapter, where we study bound states in an SNS junctions.

4.1.2 *Why does a tunnel probe measure the density of states?*

In light of the theoretical considerations in the previous section, it's now reasonable to ask: How does the behavior of Andreev reflection and the shape of $A(E)$ manifest itself in experiments? Electrical transport through a constriction between two reservoirs with a voltage drop V applied across them is given by [60]

$$I = \frac{G_N}{e}\int_0^\infty dE\,[f(E) - f(E - eV)]\,, \tag{4.10}$$

where $f(E)$ is the Fermi function and G_n is a characteristic conductance of the system. In 2-dimensional systems, G_N is given by the Sharvin resistance [1]:

$$G_N = G_{Sh} = \frac{2e^2}{h}\frac{W}{2\lambda_F}, \tag{4.11}$$

Blonder, Tinkham and Klapwijk adapted Equation (4.10) to include the effects of the proximal superconductor and showed that the current through the SN is given by

$$I_{\mathrm{NS}} = \frac{G_n}{e}\int_0^\infty dE\,[f(E) - f(E-eV)]\,(1 + A(E) - B(E)), \tag{4.12}$$

where $A(E)$ is the contribution to the current by Andreev reflections and $B(E)$ is the normal scattering that reduces the current. In the tunneling limit (i.e. large Z) Equation (4.12) reduces to a particularly useful form from an experimental perspective. In this limit, the last term in parenthesis reduces (with some algebra) exactly to the superconducting density of states

$$(1 + A(E) - B(E))\Big|_{\text{large } Z} \longrightarrow \frac{E}{\sqrt{E^2 - \Delta^2}} = \rho_s(E) \tag{4.13}$$

Calculating the differential conductance ($G = dI/dV$) of an NS interface in the tunneling regime yields

$$G_{\mathrm{NS}} = \frac{dI}{dV}\Big|_{\text{large } Z} = G_{\mathrm{Sh}}\int dE\left(-\frac{df(E-eV)}{dV}\right)\rho_s(E) \tag{4.14}$$

The derivative of a fermi function is a bell–shaped function with full width half max $\sim 4k_BT$ and an area of unity. In the $T \to 0$ limit, $df(E-eV)/dV$ reduces to a δ–function that picks out the value of the density of states at eV. Thus, in the low T limit Equation (4.16) reduces to

$$G_{\mathrm{NS}}(V) = \frac{dI_{\mathrm{NS}}}{dV} = G_{\mathrm{Sh}} \times \begin{cases} \rho_s(eV) & Z \gg 1, \quad \text{(tunneling regime)} \\ 1 + A(eV) - B(eV) & Z = 0, \quad \text{(open regime)} \end{cases} \tag{4.15}$$

Thus, a measurement of the conductance in an NS structure is an important spectroscopic tool to study the density of states and the Andreev reflection processes. We will use this method extensively below. In Figure 4.4a and 4.4b we plot the current and differential conductance respectively. It's evident that the differential conductance in the tunneling regime shown in Figure 4.4b is equivalent to the superconducting density of states shown in Figure 2.8c. In the case of an ideal interface ($Z = 0$), the subgap conductance is twice the normal state conductance, because the Andreev process involves the transfer of $2e$ across the interface. From the shape of the current in Figure 4.4a it is evident that the Z–parameter also influences the normal state conductance, even for energies $E > \Delta$. By setting $\Delta = 0$ in Equation (4.4) we see that the normal state conductance is given by

$$G_{\mathrm{NS}}|_{\Delta=0} = G_{\mathrm{Sh}}(1 - B(E)) = G_{\mathrm{Sh}}\frac{1}{1+Z^2} = G_{\mathrm{Sh}}\mathcal{T}. \tag{4.16}$$

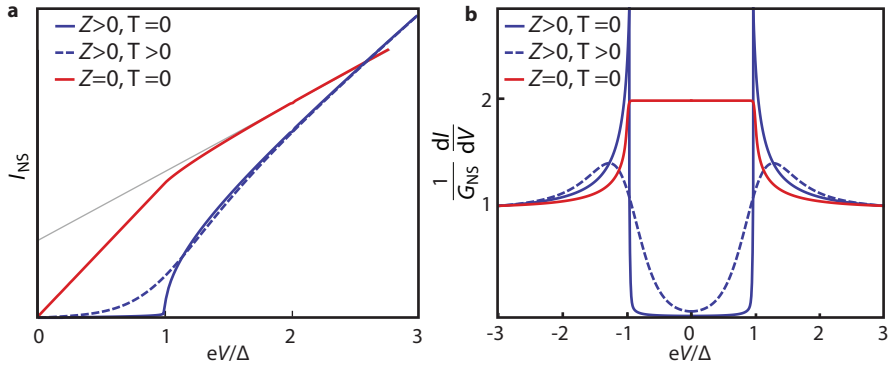

FIGURE 4.4: **a**, Current through an NS junction calculated using Eq.(4.12) in the open ($Z = 0$) and tunnel ($Z \gg 1$) regimes. The gray line indicate the excess current (see main text). **b**, Differential conductance in the open and tunneling regime. Calculated using Eq.(4.14).

Therefore Z also changes the normal state transmission, and is related to the transmissivity of the junction. The Andreev reflection adds a net current when a voltage is applied. This is the excess current, and can be used to deduce the transparency of the interface [57, 61]. The role of the excess current will be discussed in greater detail in Chapter 5.

4.2 EXPERIMENTAL SETUP OF THE ANDREEV QUANTUM POINT CONTACT

The BTK model predicts that for a sufficiently transparent NS interface, the conductance for $eV_{sd} < \Delta$ increases. In the ideal case of $Z = 0$ the conductance is exactly doubled due to Andreev reflection. As the interface becomes more like a tunnel barrier, the conductance at $eV_{sd} < \Delta$ is suppressed. An example of a system that can be tuned between the these two regimes is the geometry shown in Figure 4.9. The constriction formed by the QPC can be thought of as an effective, tunable Z–parameter between the normal region (2DEG) and the superconductor. We will refer to such a device as an Andreev Quantum Point Contact, and it is the subject of study for the remainder of the chapter. This tunable Z–parameter is, to some extent, bounded by the intrinsic Z–value of the SN interface. The simulations of the effective mass used in Chapter 2 yields a Fermi velocity $v_F \approx 10^6$ m/s, which in turns means that the fermi velocity mismatch is $r \approx 0.5$ (Fermi velocity in aluminum is $v_{F,\mathrm{Al}} = 2 \cdot 10^6$ m/s [62]). This gives a lower bound on Z via Equation (4.7) of $Z \geq 0.35$. However, since for $Z > 0$ an electron impingent on the NS interface can normal reflect, followed by another normal reflection on the backside of the QPC (or an impurity) giving it yet another chance at Andreev reflection on the NS interface, the Z of the Andreev QPC is not strictly bounded by the materials interface.

In Figure 4.6 we present finite bias measurements of the device in Figure 4.5a measured at base temperature of a dilution refrigerator, for two differ-

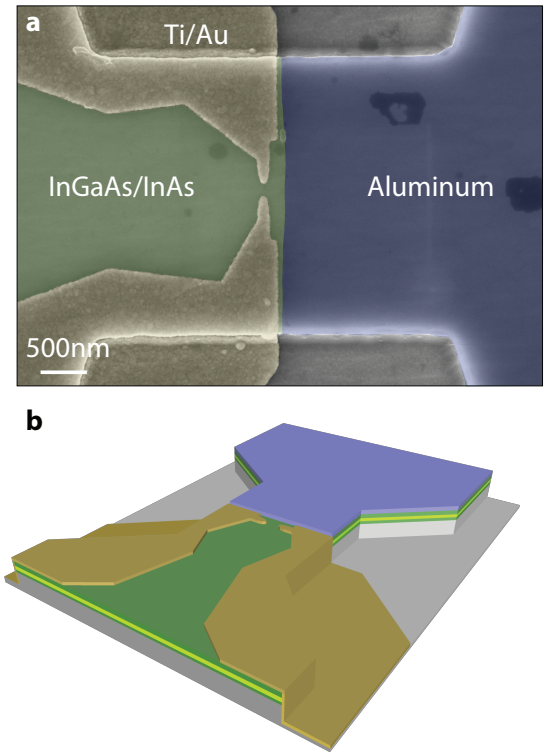

FIGURE 4.5: **a**, False color SEM image of the Andreev QPC device, fabricated on the wafer with 10 nm aluminum film and 10 nm InGaAs barrier between InAs and the aluminum film. **b**, 3D schematic of the Andreev QPC highlighting the 2DEG extending under the aluminum contact.

ent values of the QPC gate voltage. The measurement setup is discussed in detail in section 3.2.2. While the detailed shape of the curves do not map exactly onto the prediction from BTK–theory in Fig.4.4b, it is evident that for $V_g = -8.2$ V the conductance is enhanced by a factor of two at $V_{\text{sd}} = 0$ mV, while for $V_g = -8.87$ V there is gap in the local density of states of the InAs. The peak–to–peak width (highlighted with two vertical arrows) corresponds to a gap $\Delta^\star = 190$ μeV, which is commensurate with the gap in the aluminum film $\Delta_{\text{Al}} = 225$ μeV. In section 4.3 we discuss in greater detail the properties of the gap in the 2DEG and justify identifying it with the superconducting gap (as opposed to coulomb charging physics), and in section 4.4 the properties of the enhanced subgap conductance is discussed.

The best of our knowledge, this is the first observation of a superconducting gap in the density of states of a semiconducting 2D electron gas measured via tunnel spectroscopy in an open channel, as well as the first observation of conductance enhanced by exactly a factor of 2 in an Andreev QPC geometry. The properties of S-quantum dot-S using a 2DEG has previously been reported using a gate–defined quantum dot formed in a proximitized region [63, 64]. Before studying the finite bias properties in greater detail we concentrate on the zero–bias properties of the Andreev QPC.

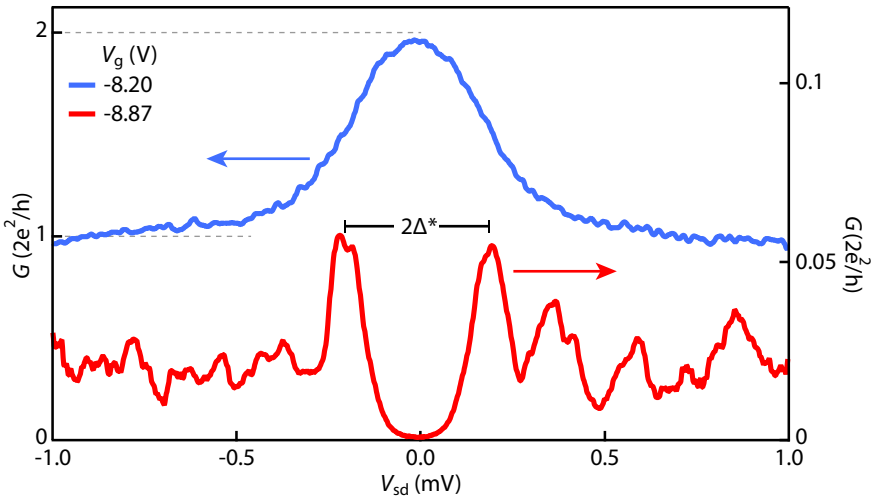

FIGURE 4.6: Finite–bias properties of the Andreev QPC at two different gate voltages. At $V_{sd} = 0$ V the device transitions from the enhanced conductance regime $G_{NS} \approx 2G_{NN}$ to the gapped regime with $G_{NS} \ll G_{NN}$ as the gate is used to tune the transmission through the constriction.

4.2.1 *Beenakkers prediction*

In a seminal paper from 1992 Carlo Beenakker studied in detail the zero bias properties of a geometry identical to the Andreev QPC, shown in Figure 4.7. One of the key results in that paper is the observation that a QPC placed proximal to a superconductor should have quantization in steps of $4e^2/h$. The added factor of two comes from the Andreev reflection at the SN interface. If we consider just a single mode, and perfect Andreev reflection at the SN interface, Beenakkers result can be derived quite nicely. Consider an electron traversing the constriction and the region of the 2DEG after the QPC with transmission t_e. It is now Andreev reflected (with probability 1) at the SN interface and is reflected as a hole, which has a phase $-ie^{i\phi}$ (see Equation (4.8)). Finally, the hole escapes the constriction with transmission t_h. This process is outlined in Figure 4.7. However, after the first Andreev reflection, the hole may scatter at an impurity (or the backside of the constriction), with a reflection r_h. The hole will then impinge on the NS interface, and is again Andreev reflected into an electron (again, costing a phase) which will traverse the same path back towards the impurity. After scattering with reflection r_e on the impurity it is finally hitting the SN interface for the 3rd time, and can Andreev reflect to finally leave the constriction with t_h. The two processes just outlined is the 0'th and 1'st order

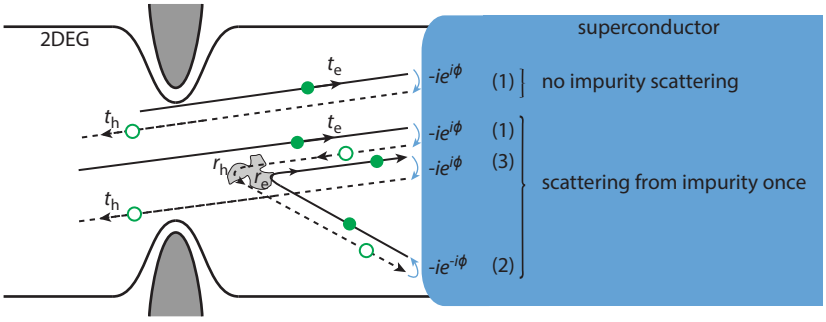

FIGURE 4.7: Cartoon depicting trajectories contributing to the Andreev reflection probability $\mathcal{A}$. The sum is carried out explicitly in Eq.(4.17).

contributions to the Andreev transmission through the constriction:

$$\begin{aligned}\mathcal{A} &= t_e(-ie^{i\phi})t_h + t_e(-ie^{i\phi})r_h(-ie^{-i\phi})r_e(-ie^{i\phi})t_h + \cdots \\ &= -ie^{i\phi}t_e\left(1 - r_h r_e + \cdots\right)t_h \\ &= -ie^{i\phi}\frac{t_e t_h}{1 + r_h r_e}\end{aligned} \tag{4.17}$$

In the last line the geometric series was was summed. By particle–hole symmetry of the s–matrix we have $r_h(E) = r_e^*(-E)$ and equivalent for t. Since we're at zero energy we can write $t_e t_h = t_e t_e^\star = \mathcal{T}$ (and similar for r_e), which yields

$$\mathcal{A} = -ie^{i\phi}\frac{\mathcal{T}}{1+\mathcal{R}} = -ie^{i\phi}\frac{\mathcal{T}}{2-\mathcal{T}} \tag{4.18}$$

where we used $\mathcal{R} = 1 - \mathcal{T}$. Finally, since each term in Equation 4.17 entails the net transfer of $2e$ across the constriction, the conductance is given by

$$G_{\text{Andreev QPC}} = 2\frac{2e^2}{h}|\mathcal{A}|^2 = \frac{4e^2}{h}\frac{\mathcal{T}^2}{(2-\mathcal{T})^2}, \tag{4.19}$$

which is the single–channel version of Beenakkers result. In Figure 4.8a, the conductance in a single channel Andreev QPC is compared with the conductance in a single channel normal QPC, with conductance $G = G_0\mathcal{T}$. The point marked G' indicates the transmission at which conductance through the Andreev QPC is greater than the conductance in the normal QPC. The remarkable factor–of–two doubling of the Andreev QPC is strikingly visible if we assume the QPC can be modeled by saddle point potential (as in section 2.1.4), in which case the $\mathcal{T}$'s are well known [42]. Figure 4.8b compares the Andreev QPC and the normal QPC in the multichannel case.

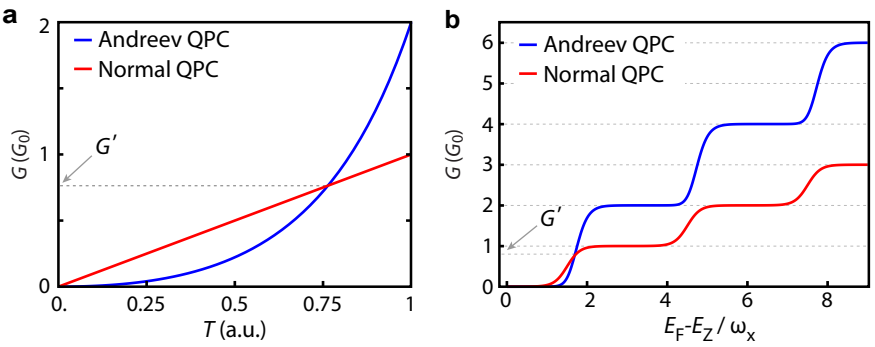

FIGURE 4.8: **a**, The conductance through a normal QPC and an Andreev QPC as the transmission is increased. By setting $G_{\text{NN}} = G_{\text{NS}}$, we find $G' = 0.76G_0$. **b**, By assuming a saddlepoint potential in the constriction to model the $\mathcal{T}$'s, the factor-of-two increase in conductance is particularly clear.

The pinchoff traces of two lithographically identical Andreev QPC devices is shown in Figure 4.9. The data labeled *Device 1* is the device imaged using SEM in Figure 4.5. The conductance at the first plateau of the QPC (corresponding to $\mathcal{T} = 1$) is clearly doubled in the superconducting case. The aluminum film can be driven normal by three different methods: Applying a field $B_\perp > B_{\perp,c}$, raising the temperature $T > T_c$ or applying a bias much larger than the gap $eV_{\text{sd}} \gg \Delta_{\text{Al}}$. In each of these regimes, the normal state QPC's show steps at NG_0 for $N = \{1, 2, 3\}$. For *Device 2* there is an extra step at $G = 1.8G_0$ of unknown origin, but with no corresponding conductance increase in the superconducting state.

The steps in the superconducting state are not particularly flat, except for the first plateau. This can be explained in part by the dependence of G on the transmission coefficients, $G \sim \mathcal{T}^2/(2-\mathcal{T})^2$. The non–linear dependence of conductance on transmission makes the conductance in the Andreev QPC particularly susceptible to resonances that decrease $\mathcal{T}$. Furthermore, the geometry of the 2DEG billiard after the constriction will also lead to resonances. We cannot deploy the trick of applying a field, or in-

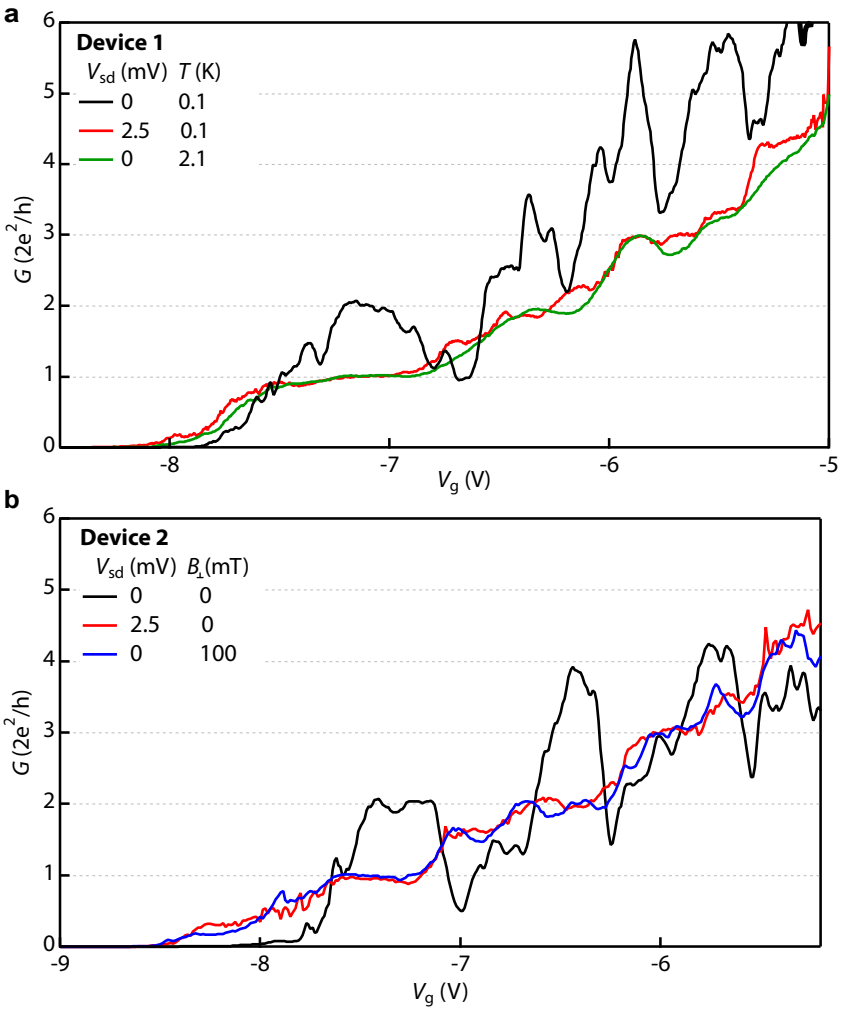

FIGURE 4.9: Conductance through two lithographically identical Andreev QPC devices. **a**, Device 1 (on which the remaining data in this chapter is taken). By increasing temperature above $T_c = 1.6$K or by applying a large bias, the QPC is in the normal state and the conductance is quantized in units of G_0. **b**, A different device, but lithographically identical the device measured in **a**, showing qualitatively the same behavior.

creasing the temperature since this will change (and ultimately destroy) the superdonducting properties of the film. Despite these shortcomings, for *Device 1* we extract $G' = 0.7G_0$ and for *Device 2* we extract $G' = 0.8G_0$, in good agreement with the Beenakkers prediction.

Some comments on the measurements are in order. Since the voltage probes are not located immediately after the constriction, there is a finite series resistance R_s not accounted for, despite the 4–terminal measurement setup (see Figure 3.11). This series resistance is in principle slightly gate–voltage dependent, since the size of the 2DEG region contributing to conductance is effectively changed when the gate is energized. However, we have chosen to counter this by subtracting only a *constant* series resistance, chosen to move the first plateau in the normal state to $G = 2e^2/h$. This is achieved for both devices by subtracting $R_s = 1.35$ kΩ from the pinchoff

curves. The same series resistance is subtracted from the superconducting state. As discussed in Section 2.1.4 asymmetrically gating the device can help understand spurious resonances, and avoid them. For device 1 the QPC gates have an offset $V_{\text{offset}} = +1\ V$ between them, so that when setting e.g. $V_g = V_0$ means $V_{g,\text{left}} = V_0 - 0.5\ V$ and $V_{g,\text{right}} = V_0 + 0.5\ V$. The data on asymmetrically gating this device is shown in Figure 2.7c. Device 2 has no offset between the gates.

Beenakkers result can be recast in a particularly illuminating form [24], which allows quantifying to what extent the conductance in the Andreev QPC is governed by Equation (4.19). By writing Equation (4.19) as

$$G_{\text{NS}} = 2G_0 \frac{G_{\text{NN}}^2}{(2G_0 - G_{\text{NN}})^2} \tag{4.20}$$

Beenakkers formula can be used to answer the question "For a given normal–state conductance, what is the subgap conductance in the superconducting state if Andreev reflection is perfect?". If the subgap conductance is close to that given by Equation 4.20 then the superconducting gap is said to be "hard".

From the pinchoff traces in Figure 4.9a, we see that applying a bias across the QPC is equivalent to driving the superconducting film normal, and we can therefore use $G(eV_{\text{sd}} > \Delta_{\text{Al}})$ as the normal state conductance G_{NN}. To this end, we have have measured the finite–bias conductance through the Andreev QPC as a function of gate–voltage, shown in Figure 4.10a. The characteristic superconducting gap in the density of states is visible for $V_g < -8.4\ V$, while at more positive gatevoltages the enhanced conductance is visible. The finite–bias data in Figure 4.6 is cuts in the dataset from Figure 4.10, indicated by the red, blue rectangles above the 2D plot. We extract the normal state conductance as the average conductance in the range $|V_{\text{sd}}| > 0.8$. By using this value for G_{NN} in Equation (4.20), we are able to compare our measured data to the prediction, as shown with green line in Figure 4.10b. The model has no fitting parameters, and the data mimics the prediction over almost four orders of magnitude. It is presently unclear if the systematic deviation of the measurement from the prediction at $G_{\text{NN}} < 0.1 \times 2e^2/h$ is an artifact of the device geometry (the QPC is located a distance $\sim$230 nm from the SN interface) or if it presents a fundamental limit on the finite subgap conductance in this wafer. However, the deviation may stem from something as mundane as our definition of G_{NN}. We strove to choose a fair definition of G_{NN} that would not evoke feelings of cherry picking, and we tested that if the averaging is changed to include more or less of the data for $|eV_{\text{sd}}| > 0.5$ mV the results are largely unchanged.

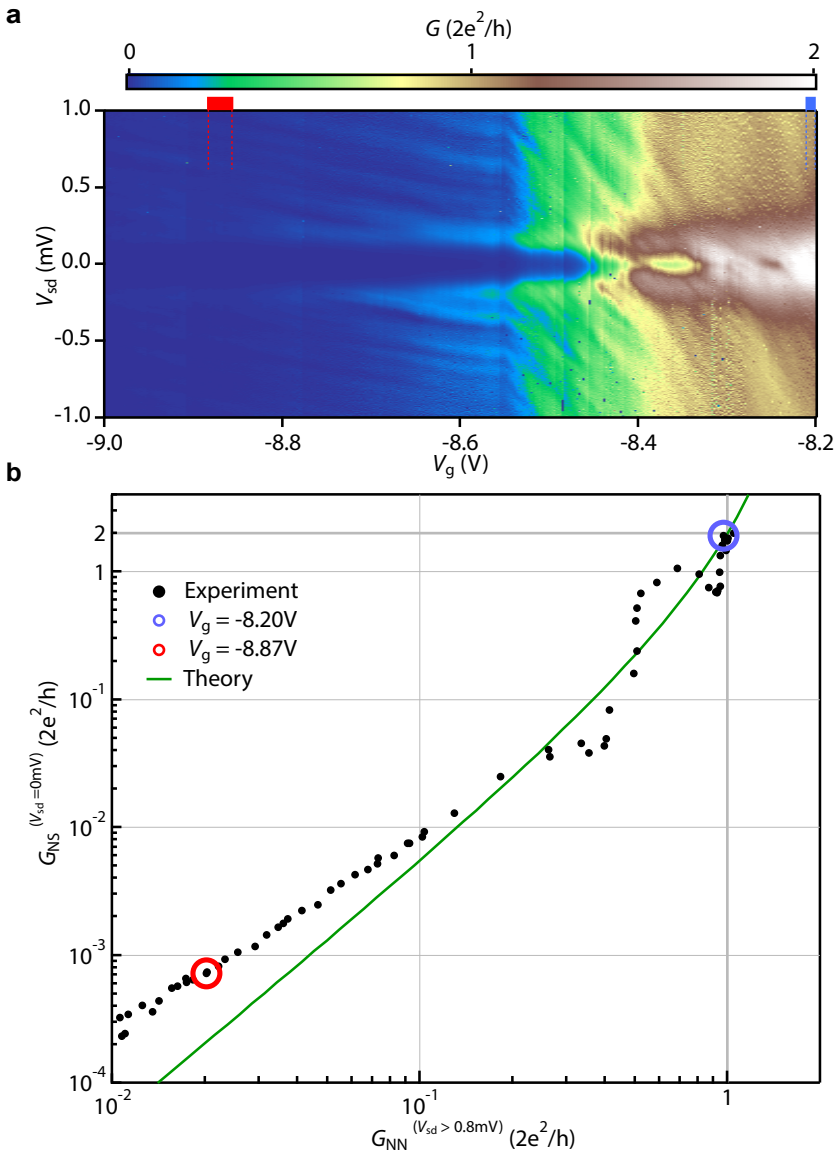

FIGURE 4.10: **a**, Finite–bias spectroscopy of the Andreev QPC. The transition from conductance enhancement to conductance suppression at zero bias is clearly visible. **b**, The conductance in the superconducting state as a function of the conductance in the normal state. The Beenakker theory (Equation (4.20)) is shown in the green curve. The normal state conductance is calculated as the average conductance for $|eV_{sd}| > 0.8$ mV.

Finally, before studying in detail the properties of the superconducting gap and the enhanced conductance, we briefly mention a detail of the measurement presented in Figure 4.10. Since the conductance in the superconducting gap is strongly suppressed, we are measuring a (very) large resistance. The input impedance on the voltage preamplifiers is 100 MΩ DC and approximately 10MΩ when measured using AC voltages. Since at $G = 0.01G_0$ the resistance is $\sim$10 MΩ, we change instead to a two–terminal measurement. Using only DC voltage we sample with a spacing of 4 μV. The data is then smoothed over 30 μV range and the derivative is calculated

numerically. Finally, the resistance of the lines is $R_{\text{line}} = 4.1\ \text{k}\Omega$ and a series resistance $R_s = 800\ \Omega$ is subtracted from the data. This value of R_s is chosen to move the plateau at $V_g = -8.2$ V at large bias to $2e^2/h$, similarly to how R_s was chosen in Figure 4.9.

4.3 TUNNEL SPECTROSCOPY AND THE HARD SUPERCONDUCTING GAP

For applications to Majorana devices, the possibility to locally probe the density of states in the topological superconductor is a key tool. Here we present detailed data on the gap in the local density of states. From the large–range gate–scan and the comparison to Beenakkers prediction in Figure 4.10 it is evident that there are no quantum dot–physics obscuring the measurement of the gap. This is in contrast to many of the superconductor/semiconductor nanowire experiments, where one sometimes has to disentangle a coulomb blockade gap and the superconducting gap [13, 24, 65, 66].

First we elevate the temperature and study the behavior of the gap, as shown in Figure 4.11. The critical temperature of the suppressed conductance exactly matches the aluminum film $T_c = 1.58$K. At finite temperatures the density of states is smeared by $\sim 2k_BT$ due to the Fermi functions in Eq.(4.14), the conductance at zero bias is dependent on the temperature according to

$$\frac{G_{\text{NS}}}{G_{\text{NN}}} = \sqrt{\frac{2\pi\Delta^\star}{k_BT}}e^{-\Delta^\star/k_BT} \tag{4.21}$$

for temperatures $k_BT \ll \Delta$ [3]. We have plotted the zerobias conductance in Figure 4.11b and compared to Equation (4.21). If we offset to match the finite subgap conductance at $T = 0.1$ K, we extract a $\Delta^\star = 150\ \mu$eV (the fit is shown in inset of Figure 4.11), in rough agreement with the peak–to–peak gap $\Delta^\star \approx 190\ \mu$eV.

The finite–bias shape of the density of states, Figure 4.11, deviates from that of the ideal BTK prediction (Figure 4.4). The thermal energy scale is $k_BT_e = 8\ \mu$eV, so it cannot be attributed to a broadening due to temperature. It could be a manifestation of the "soft" gap due to a less–than–stellar interface [67, 68]. However, this would not be reconcilable with the factor–of–two enhancement (which requires a close–to–stellar interface), nor with the good agreement at zero bias with Beenakkers prediction in Figure 4.10. Instead, we propose the separation of the QPC to the NS interface as well as the billiard in front of the NS interface as the reason for the deviation.

To quantify this, we consider the level spacing (i.e. Thouless energy) in the billiard formed between the QPC and the NS interface. The Thouless energy is related to the dwell in the region via,

$$E_{\text{Th}} = \frac{\hbar}{\tau_D} \tag{4.22}$$

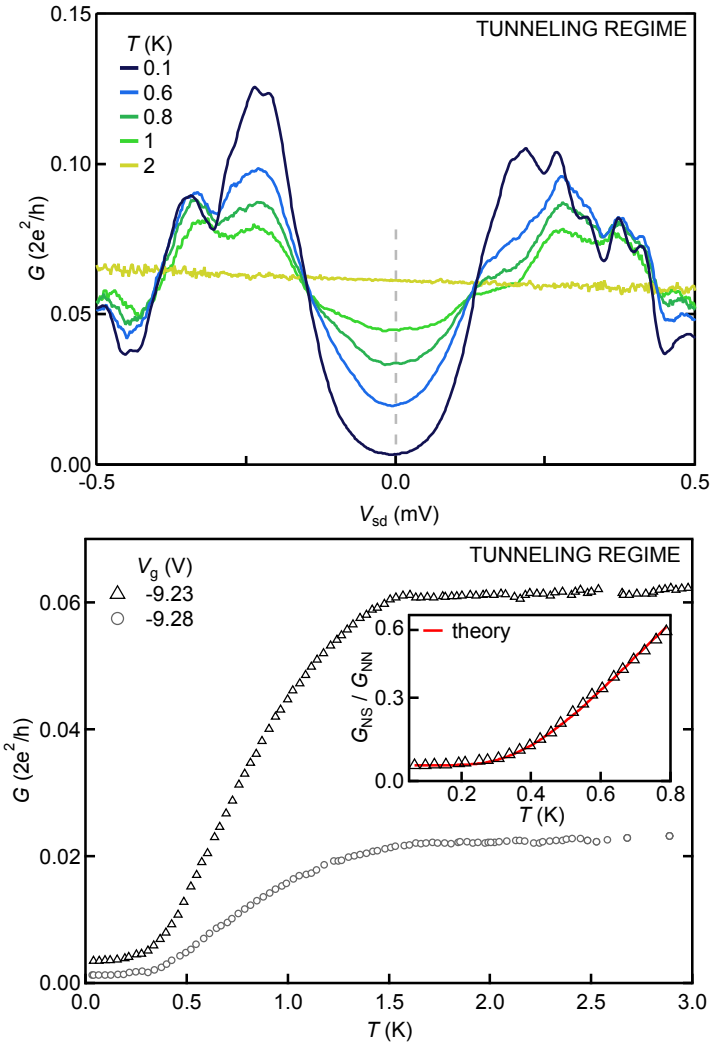

FIGURE 4.11: **a**, Finite bias spectroscopy as the temperature is elevated. **b**, Conductance at $V_{sd} = 0$ mV as the temperature is increased, for two different values of the gate voltage. The critical temperature matches that of the aluminum film, as measured in Section 2.2.1. Inset shows a fit to Equation (4.21) for the data at $V_g = -9.23$ V. The fit gives identical values for $V_g = -9.28$ V.

where in the diffusive case, the dwell time is $\tau_D = (L \cdot W)/D$ and in 2D the diffusion constant is $D = v_F l_e/2$. Using $L = 230$ nm and $W = 1.1\mu$ m from the SEM image in 4.5a the Thouless energy is $E_{\text{Th}} = 290$ μeV, slightly larger than the gap. However, to account for the finite lifetime of electrons penetrating under the aluminum in the InAs, we define an effective length $L_{\text{eff}} = L + \xi_d$, where $\xi_d = \sqrt{\frac{\hbar D}{\Delta^\star}}$ is the superconducting coherence length in the semiconductor (in the diffusive case). This coherence length for $\Delta^\star = 190$ μeV is $\xi_d = 620$ nm and consequently the Thouless energy becomes $E_{\text{Th,eff}} \approx 80$ μeV. The spacing of the level in the billiard can thus lead to the smearing we observe. Since the decay length under the superconductor is not a quantity we know with certainty, the value of $E_{\text{Th,eff}}$ should only be used for a qualitative assessment. Finally, we mention that in experiments

on S–S'–S systems, it was demonstrated the the finite–bias shape of the gap is dependent on the position of the tunnel probe relative to the S–S' interface, but the zero–bias conductance was unchanged [69, 70, 71].

We also study the in–plane magnetic field dependence of the gap, shown in Figure 4.12. For a superconductor/semiconductor device to transition

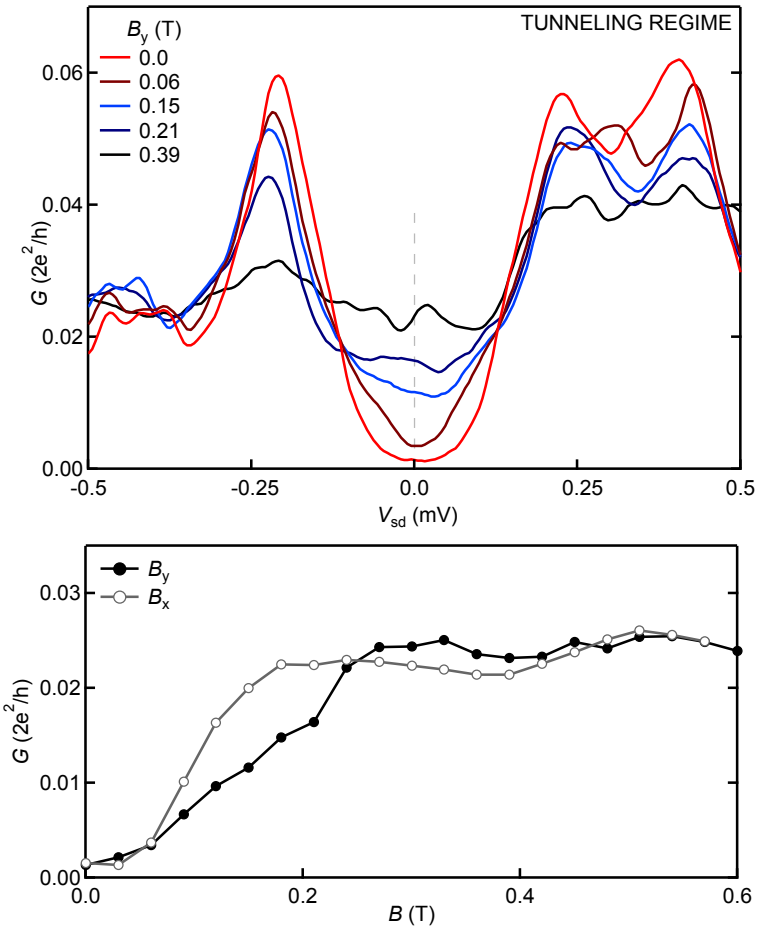

FIGURE 4.12: **a**, Finite bias spectroscopy as the in–plane field is increased. **b**, Conductance at $V_{sd} = 0$mV as the field is increased in the two different in–plane direction. B_x is perpendicular to the direction of motion in the QPC and B_y is along the constriction. The difference in $B_c^\star$ for the two directions could be due to an anisotropic g–factor.

to the topological regime, which harbors Majorana fermions, it is a requirement that the Zeeman energy should close the gap in the 2DEG (we'll explicitly derive this result in Chapter 6). Despite the gap in the 2DEG closing, the parent superconductor should retain its gap. To investigate the feasibility of reaching this regime, we apply a field in the plane of the chip, as shown in Figure 4.12 with B_x perpendicular to the direction of motion in the QPC and B_y along the constriction. At an in–plane field of $B_c^\star = 350$ mT the sub-gap conductance is no longer dependent on the field magnitude, indicating Andreev reflections in the 2DEG region is suppressed due to the Zeeman field. From the measurements of the aluminum film in section 2.2.1, the in–plane critical field of the bare film was measured to be $B_c = 1.65$ T, so

the aluminum itself is still superconducting. If we assume the gap is closed solely by Zeeman effect in 2DEG, then $B_c^\star = 350$ mT would correspond to a g–factor

$$g\mu_B B_c^\star = \Delta^\star \Rightarrow g \approx 9 \tag{4.23}$$

roughly consistent with measurements in similar InGaAs/InAs heterostructures [72, 73, 74]. The reduced value of the g–factor from that of bulk InAs ($g_{\text{InAs}} \sim -14$) could be due to the extension of the wave function into the InGaAs regime [74, 75]. It thus seems feasible to drive a device, with suitable geometry, fabricated on the epi–Al/InAs wafer, into the topological regime and use electrostatic gates as a tunable probe of the local density of states in the proximitized InAs.

4.4 ONE–CHANNEL REGIME OF THE ANDREEV QPC

We now turn to the one–channel regime of the Andreev QPC. Here, one channel with a transmission of approximately unity leads to the $2 \cdot G_0$ conductance at zero bias, as predicted by Beenakker [76]. In Figure 4.13a the finite bias behavior of the enhanced conductance is shown. Since the conductance at zero bias is enhanced by a factor very close to two, we would expect $Z \approx 0$ in the naive BTK model. If the system could be described exactly by the BTK formalism, we then expect the shape of the finite bias to be peaked at $|eV_{\text{sd}}| = \Delta^\star$ (c.f. Figure 4.4b). On the contrary, we observe a monotonic decrease of conductance down to $2e^2/h$ at $|eV_{\text{sd}}| \gtrsim 2\Delta^\star$. This deviation is believed to stem from the Thouless smearing effect discussed for the tunneling regime in the previous section.

From Figure 4.13b, the temperature dependence exhibits a sharp cusp at $T \approx 1.6$ K, again in good agreement with the superconducting film. In the inset of Fig.4.13b we have produced a naive model to understand the qualitative features of the temperature dependence. To this end, we have calculated the conductance through an idealized 1D NS junction using Equation (4.16), with perfect Andreev reflection $Z = 0$, and used $A(E)$ from Table 4. The temperature dependence is implemented with a Fermi–function derivative and the gap scales with temperature as $\Delta(T) = \Delta_0\sqrt{1-(T/T_c)^2}$, where we used $T_c = 1.6$ K. Despite the model neglecting all geometrical factors, we capture the qualitative feature of the kink and can understand the shape in terms of Andreev reflection from a gap suppressed by thermal population.

We pause to comment on two details of the measurement presented in Figure 4.13, related to the scaling of the voltage–drop across the device. The measurement is done in a 4–terminal voltage bias setup (same as for the tunneling regime). However, unlike in the tunneling regime, the voltage drop in the 2DEG out to the voltage probes is no longer negligible compared to the voltage drop across the device. To correct this, we have introduced a series resistance similar to that of the QPC. The measured voltage can be

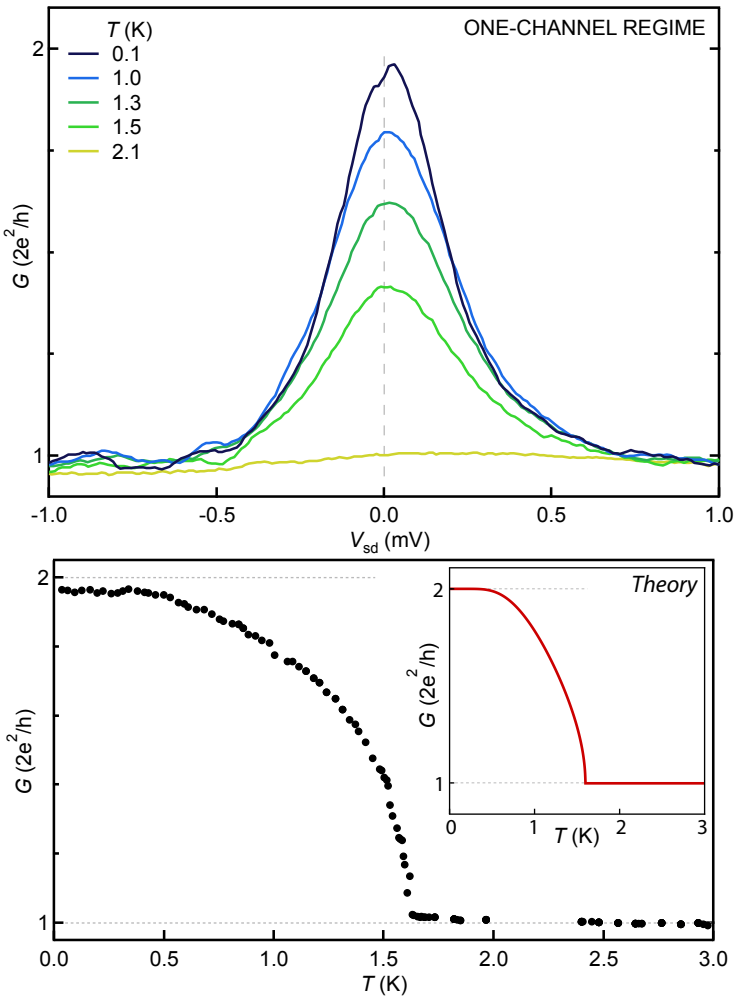

FIGURE 4.13: **a**, Temperature dependence of the enhanced conductance in the Andreev QPC. **b**, Zero bias data for the temperature dependence. The kink happens exactly at $T = 1.6$K, in good agreement with T_c of the 10nm aluminum film.

decomposed into two components $V_{\text{measured}} = V_{\text{device}} + \widetilde{V}$, where $\widetilde{V}$ is the voltage drop in the 2DEG out to the probe. The voltage across the device is therefore

$$V_{\text{device}} = V_{\text{measured}} - \widetilde{V} = \left(R_{\text{measured}} - \widetilde{R}\right) I_{\text{dc}} \tag{4.24}$$

Since I_{dc} is measured, the voltage drop across the device is determined by fixing $\widetilde{R}$. We set $\widetilde{R} = R_{\text{s}} = 1\ \text{k}\Omega$, the series resistance subtracted to move the plateau in the normal state to G_0. The x–axis in Figure 4.13a is calculated using Equation (4.24). The kink structure in Figure 4.13b is measured by simultaneously recording the temperature and conductance as a function of time while the fridge is cooling. Since $T = 1.6\ \text{K} = T_c$ is close to the critical point where the dilute He^3–He^4-mixture is unstable, temperature measurements in this regime are tricky. We therefore swept the temperature through this value several times, and finally plotted the conductance and

temperature parametrically. For this data set we have again chosen an R_s such that the conductance at $T > T_c$ is G_0.

Finally, we measured the in–plane field dependence of the enhanced conductance, shown in Figure 4.14. The enhanced conductance decays on a magnetic field scale comparable to the superconducting gap.

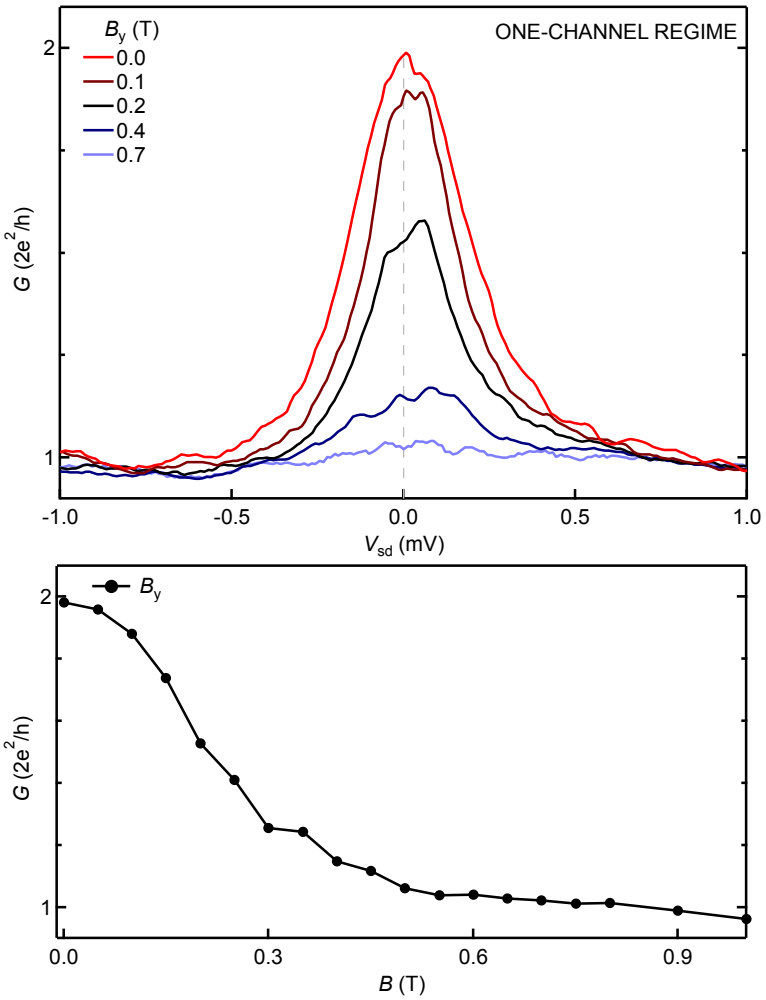

FIGURE 4.14: **a**, Finite–bias spectroscopy of the one–channel regime as a function of in plane magnetic field. **b**, Conductance at zero bias as the field is increased.

4.5 CONCLUSION

In this chapter we have introduced the mechanism of Andreev reflection and the BTK formalism to understand how a normal metal (semiconductor) can inherit properties of a superconductor. By studying the conductance of a quantum point contact placed proximal to the superconductor/2D electron gas interface in the epi–Al/InAs wafers, we demonstrated increased conductance by a factor of two, as well as suppressed conductance, depend-

ing on gate–voltage on the QPC. Finally, we investigated the temperature and in–plane magnetic field dependence of this Andreev QPC geometry.

This electrostatically controllable tunnel probe of the local density of states in a 2D electron gas with a hard superconducting gap is, to the best of our knowledge, the first of its kind. Besides observing the quantization in terms of $4e^2/h$, due to Andreev reflection, it is a key technological device for measuring Majorana fermions.

5

JOSEPHSON JUNCTIONS IN EPI–AL/INAS

In this chapter we focus on the properties of a device with two superconducting banks and an exposed region of InAs quantum well in between. Such "SNS" structures can pass a supercurrent through the normal region, and go by the name of Josephson Junctions, after Brian Josephson who predicted the presence of the supercurrent through the SNS sandwich despite the non–superconducting patty (Josephsons original work was on S–thin insulating layer–S structures, but the S–semiconductor–S cousins have retained the name). The magnitude and temperature dependence of the supercurrent carried through the junction, as well as the conductance at finite bias, reveal properties of the coupling between the N and S layer. We'll study those properties in detail below.

The analysis of the data presented in this chapter is still a work in progress, so all facets of the data cannot be presented in a coherent framework. The last section is devoted to a discussion and speculations on the more puzzling features.

5.1 THE SUPERCURRENT CARRYING BOUND STATE

For simplicity we start by considering an SNS junction in an ideal 1D system with no barriers at the SN and NS interfaces, as shown in Figure 5.1. We'll subsequently generalize this model to account for non–ideal interfaces. The supercurrent in the junction is carried by bound states of electron/hole pairs, formed by Andreev reflection at the left and right superconducting banks [44, 77]. The value of the supercurrent is dependent on the phase difference between the superconductors via

$$I = \frac{2e}{\hbar}\frac{dE}{d\phi} \tag{5.1}$$

where E is the energy of the bound state. To calculate the magnitude of the maximal supercurrent (the critical current), we have to work out how the energy of the bound state depends on the phase across the junction. To

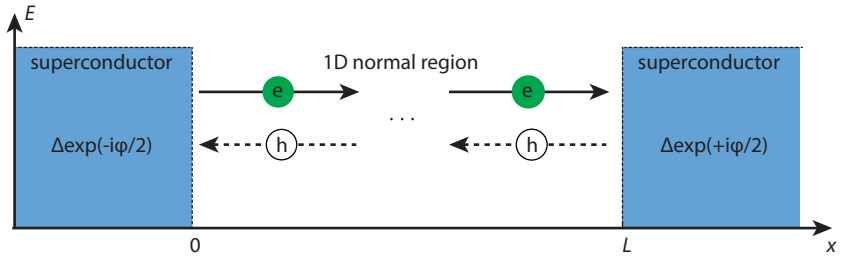

FIGURE 5.1: Schematic of an ideal 1D SNS junction

derive the eigenstates of the SNS system, we are looking for solutions to the 1D Bogoliubov-de Gennes equation (2.14) with the superconducting order parameter given by

$$\Delta(x) = \begin{cases} \Delta_0 e^{-i\phi/2} & x < 0 \\ 0 & 0 < x < L \\ \Delta_0 e^{+i\phi/2} & x > L \end{cases} \tag{5.2}$$

For $|E| > \Delta_0$ there will be a continuum of solutions while for $|E| < \Delta_0$ there is a discrete set of bound states, carrying the supercurrent. Since there are no states allowed within the gap, states with energy $|E| < \Delta_0$ will be exponentially decaying solutions in the superconducting region. Following the original treatment by Kulik [78], the ansatz for the wavefunctions of the left $(-)$ and right $(+)$ moving states in such an SNS sandwich can be written as

$$\Psi_+ = \begin{cases} A_+ \begin{pmatrix} v_0 e^{-i\phi/2} \\ u_0 \end{pmatrix} e^{+ik'_h x} & x < 0 \\ B_+ \begin{pmatrix} v_0 e^{-i\phi/2} \\ 0 \end{pmatrix} e^{+ik_e x} + B_+ \begin{pmatrix} 0 \\ u_0 \end{pmatrix} e^{+ik_h x} & 0 < x < L \\ C_+ \begin{pmatrix} v_0 e^{+i\phi/2} \\ u_0 \end{pmatrix} e^{+ik'_e (x-L)} & x > L \end{cases} \tag{5.3}$$

$$\Psi_- = \begin{cases} A_- \begin{pmatrix} v_0 e^{-i\phi/2} \\ u_0 \end{pmatrix} e^{-ik'_e x} & x < 0 \\ B_- \begin{pmatrix} v_0 e^{-i\phi/2} \\ 0 \end{pmatrix} e^{-ik_e x} + B_- \begin{pmatrix} 0 \\ u_0 \end{pmatrix} e^{-ik_h x} & 0 < x < L \\ C_- \begin{pmatrix} v_0 e^{+i\phi/2} \\ u_0 \end{pmatrix} e^{-ik'_h (x-L)} & x > L \end{cases} \tag{5.4}$$

where k is the wave vector in the normal metal and k' is the wavevector in the superconducting region. Both are defined in Equation (4.5), and the subscript e ($\tau = -1$) and h ($\tau = 1$) refers to electrons and holes, respectively. For energies $|E| < \Delta_0$ the definition of k'_τ has imaginary components, corresponding to the evanescent waves in the superconductor. Imposing boundary conditions on the wavefunction yields the following equation for the energy [44]

$$\frac{E}{\Delta_0}\frac{L}{\xi_0} = 2\pi n \mp \phi + 2\arccos\frac{E}{\Delta_0}, \tag{5.5}$$

where we have introduced the superconducting coherence length for the carriers in the semiconductor,

$$\xi_0 = \frac{\hbar v_F}{2\Delta_0}, \tag{5.6}$$

and v_F is the Fermi velocity in InAs. Deriving Equation (5.5) requires a little footwork, but the result is very appealing. We can interpret each term as contributions to Bohr–Sommerfeld quantization in the SNS structure: The term $\arccos(E/\Delta_0)$ is the phase acquired from the evanescent waves penetrating into the superconductor, the term $EL/\Delta_0\xi_0$ is the phase shift from traversing the N region, and ϕ is the superconducting phase picked up from the Andreev reflection. In the limit of a *short junction* where the phase acquired on traversing the normal region is negligible, i.e.

$$L \ll \xi_0, \tag{5.7}$$

the two lowest eigenvalues of Equation (5.5) have a simple form

$$\begin{aligned} E^+(\phi) &= \Delta_0 \cos\phi/2 \\ E^-(\phi) &= -\Delta_0 \cos\phi/2 \end{aligned} \tag{5.8}$$

and the supercurrent carried by these two modes can now be calculated by plugging the energies in Equation (5.8) into Equation (5.1). The resulting equations

$$\begin{aligned} I^+(\phi) &= -\tfrac{e\Delta}{\hbar}\sin\phi/2 \\ I^-(\phi) &= \tfrac{e\Delta}{\hbar}\sin\phi/2 \end{aligned} \tag{5.9}$$

gives the current–phase relationship (CPR), and is a key construct for analyzing an SNS junctions [79].

The ideal interface between the normal- and superconducting metal is not sufficient to capture key experimental observations about supercurrents in SNS junctions. P.F. Bagwell extended this ideal model to include scattering from a δ–function impurity in the SNS region [80]. The effect of a degraded SN interface (due to processing) was tackled by Beenakker who introduced δ–barriers at the interface (similar to the BTK treatment of the SN interface) [81]. Similar results were obtained by Tang *et al.* [82]. Here we'll settle for quoting the result of these more sophisticated treatments. The model of a degraded interface in an SNS junction is sketched in Figure 5.2, and the potential in the BdG equation is modified to

$$U(x) = \frac{\hbar^2 k_{Fs}}{m} Z\left(\delta(x) + \delta(x-L)\right) \tag{5.10}$$

The barriers lead to the possibility of normal state reflection which reduces

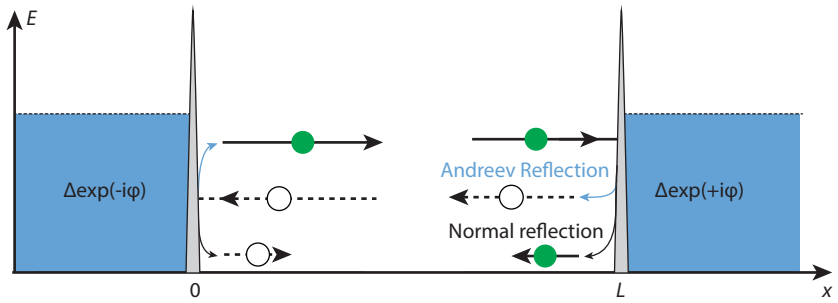

FIGURE 5.2: Schematic of an SNS junction with impurities at the interfaces, leading to both normal and Andreev reflection at the interface.

the supercurrent through the constriction. Introducing the Z parameter again, the energies of the bound states in the short junction limit ($L \ll \xi_0$) are now given by [44]

$$E^{\pm}(\phi) = \pm\Delta_0\sqrt{\frac{\cos^2(\phi/2)+Z^2}{1+Z^2}} = \pm\Delta\sqrt{1-\mathcal{T}\sin^2\phi/2} \tag{5.11}$$

where we introduced the transmissivity $\mathcal{T} = 1/(1+Z^2)$ from section 4.1.2. Equation (5.11) reduces to the ideal case in Equation (5.8) for $Z \to 0$. The supercurrent is found similarly to the ideal case and yields

$$\begin{aligned} I^+(\phi,\mathcal{T}) &= -\frac{e\Delta}{2\hbar}\frac{\mathcal{T}\sin\phi}{\sqrt{1-\mathcal{T}\sin^2(\phi/2)}} \\ I^-(\phi,\mathcal{T}) &= \frac{e\Delta}{2\hbar}\frac{\mathcal{T}\sin\phi}{\sqrt{1-\mathcal{T}\sin^2(\phi/2)}} \end{aligned} \tag{5.12}$$

The energies of the bound states in Equation (5.11) and the corresponding current-phase relationships from Equation (5.12) is plotted in Figure 5.3. The

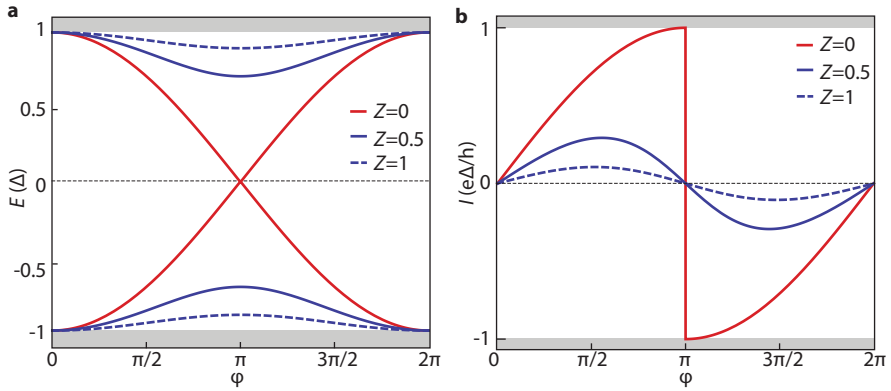

FIGURE 5.3: **a**, The energy of the bound state for different values of the interface scattering parameter Z. **b**, The current phase relation with interface scattering.

critical current of an SNS structure is the current through the system when the phase maximizes the current–phase relationship,

$$I_c = \max_\phi \left[I(\phi)\right] \tag{5.13}$$

We now see how a barrier adversely affects the supercurrent in an SNS junction: The critical current scales with the maximal value of the CPR, and the maximal value of the CPR is dependent on $\mathcal{T}$. The study of the current–phase relationship (which is to say, the study of bound states in an SNS junction) is a vast subject with numerous refinements and additions to the simple picture outlined above [79]. For the qualitative discussions below, this picture will suffice.

5.2 MEASUREMENTS AND PROPERTIES OF THE SUPERCURRENT

We are now in a position to understand the basic behavior of the SNS junction. Figure 5.4 shows an SEM image of of a junction fabricated in the epi-Al/InAs wafer. Details of the measurement setup is given back in section 3.2.2. As the driving current is increased from zero, the device will switch from the supercurrent carrying state to a state with a dissipative current. The maximal current the junction can support without dissipation

is the critical current, I_c, from the previous section. Due to heating upon switching from the resistive branch to the superconducting state [83], or dynamics of an underdamped Josephson junction [3] the critical current is not identical when switching from resistive state to superconducting state, as when switching from superconducting state to resistive state. The analysis and discussion below will focus on I_c measured at $I > 0$, and increasing the current from zero. The junction studied here has separation between the electrodes of $L = 200$ nm and a width $W = 3$ μm. The critical current is $I_c = 1.78$ μA. We can estimate the theoretical maximal supercurrent in

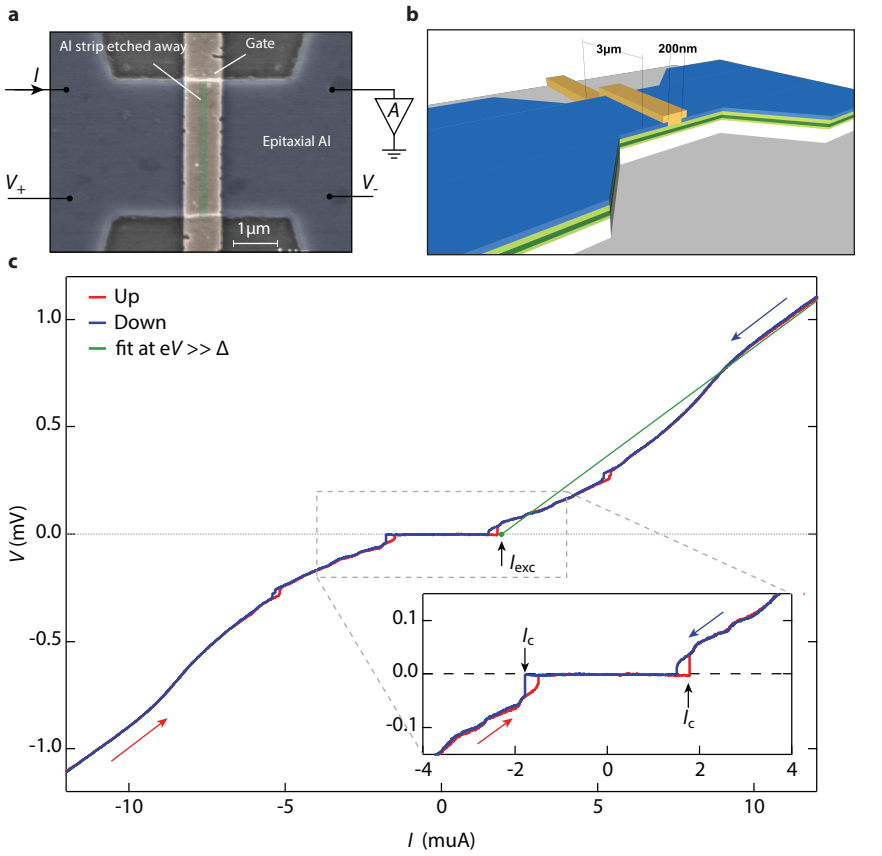

FIGURE 5.4: **a**, False-color SEM micrograph of the device measured in this chapter. The region with the aluminum etched away is underneath the gate. **b**, 3D schematic of the device. **c**, IV curve of the SNS junction. The inset shows a zoomin close to transition from the superconducting state to the normal state. The green line is a linear fit at voltages larger than Δ and its intercept with x–axis defines the excess current.

the junction as follows. In a short impurity free constriction which satisfies $\xi \ll L$ each mode will carry a critical current $\Delta I_c = \frac{e\Delta}{\hbar}$ [84, 85]. The number of modes can be roughly estimated by $N = 2W/\lambda_F \approx 430$, which yields a maximal critical current $I_c^{\text{theory}} = 23.5$ μA, a far cry from the measured value. However, this simple argument assumes all modes transmit with equal probability and that there is no disorder in the junction. I_c is usually significantly lowered due to a non–ideal interface between the superconductor and semiconductor and impurities in the normal region [86]. A rough

estimate for the transmissivity through the junction is usually found by comparing the Sharvin resistance $R_{\text{sh}} = h/(2e^2) \cdot 2\lambda_F/W = 30\Omega$ to the normal state resistance $R_n = 100\Omega$, which yields a rough per–mode transmissivity of $\mathcal{T} \sim 1/3$. The Z parameter from the BTK model can be is estimated from $\mathcal{T}$ via [87]

$$R_{\text{Sh}} = \mathcal{T} R_n = \frac{1}{1+Z^2} R_n \Longrightarrow Z \approx 1.5 \tag{5.14}$$

This value cannot be explained by Fermi velocity mismatch in the normal metal and the semiconductor, as discussed back in section 4.2. This back–of–the–envelope result is in stark contrast to the observations made about the enhanced conductance in the Andreev QPC, indicating the junction properties are not well described in such a simple picture of many non–interacting modes with identical transmission. This discrepancy between Z estimated by other means and Z estimated as the ratio of Sharvin– to normal state–resistance, was also observed by Taboryski *et al.* in a Al-GaAs-Al systems [33].

Another figure of merit for the quality of an SNS junction is the product of the normal state resistance and the critical current. SNS junctions are classified by the ordering of the parameters l_e (mean free path of 2DEG), L (separation between the electrodes) and ξ (coherence length in the semiconducting region). These values along with other characteristic length scales is tabulated in Table 5. Since l_e sets the shortest length the junction is in the

L (μm)	W (μm)	l_e (μm)	ξ_b (μm)*	ξ_d (μm)†
0.2	3.0	0.23	1.5	0.6

TABLE 5: Geometrical parameters of the SNS junction. $^\star\xi_b = \hbar v_F/2\Delta$ is the coherence length in the ballistic case. †The coherence length in the diffusive case $\xi_d = \sqrt{\hbar D/\Delta}$. Both values calculated using the bulk gap of the aluminum film $\Delta_{\text{Al}} = 225$ μeV.

short, *quasiballistic* and *dirty* regime ($L \ll \xi$, $l_e \sim L$, $l_e < \xi_{d,b}$). In the dirty regime, the supercurrent and normal state resistance is dominated by scattering in the junction, not at the interface, and the value of $I_c R_n$ is related to the gap via $I_c R_n = \pi\Delta/2e$ (sometimes nicknamed the "KO-II" result [88], in contrast to "KO-I" which is the clean limit [89]). For the present junction $I_c R_n = 178$ μeV, which yields an estimate of $\Delta_{\text{KO-II}} = 112$ μeV, in decent agreement with the gap from the tunneling experiments of the previous chapter. However, the $I_c R_n$ value should only be used as a rough estimate of the gap, and experimentally, the $I_c R_n$ often significantly underestimates the gap in S–2DEG–S junctions [49, 51, 90, 91].

Another stab at understanding the properties of the junction can be derived from the excess current [57]. Roughly, the excess current is the current due to the Andreev scattering process involving a charge transfer of $2e$ across the junction. Experimentally we find it by fitting a line to the linear

part of the *IV* curve in Figure 5.4c for $eV \gg \Delta$. The intercept with the x–axis is the excess current and in this case we find $I_{\text{exc}} = 2.0\ \mu$A. For the ideal case of no normal reflection, the excess current was worked out analytically in the case of a clean junction in the original BTK treatment for an NS junction, $I_{\text{exc}}^{Z=0} R_n = (4/3)(\Delta/e)$ [57]. A similar result was derived in the case of a diffusive junction, $I_{\text{exc}} R_n = (\frac{\pi^2}{4} - 1)\Delta/e$ [92, 93]. Using $\Delta^\star$ the theoretically expected $I_{\text{exc}} R_n$ product for a diffusive junction is 280 μeV, in good agreement with our data, for which $I_{\text{exc}} R_n = 200\ \mu$eV. The electronic properties of the Josephson junction is tabulated in Table 6.

Δ_0 (μeV)	$\Delta^\star$ (μeV)	I_c (μA)	I_{exc} (μA)	$I_c R_n$ (μeV)	$I_{\text{exc}} R_n$ (μeV)
225	190	1.78	2.0	178	200

TABLE 6: Electronic parameters of the SNS junction. Δ_0 refers to the gap of the aluminum inferred by $\Delta(0) = 1.76 k_B T_c$ and $\Delta^\star$ refers to the gap inferred via tunnel spectroscopy in Chapter 4.

5.2.1 *Gateability of the supercurrent*

We now proceed to energize the topgate covering the entire SNS region. Figure 5.5a shows the differential resistance as the gate is used to deplete the 2DEG. The critical current and the $I_c R_n$ product is shown in Figure 5.5b. The critical current is unchanged down to $V_g = -1.7$ V despite the density changing by a factor of ~ 2 (c.f. Figure 2.5)). This is consistent with the observation of the previous section that the critical current cannot be understood as N ballistic modes, each contributing ΔI_c, but rather, is limited by scattering in the junction.

Figure 5.5d shows a zoom–in on the critical current in the gate range 0 V to -1.2 V (the corresponding area is highlighted in the light green box in 5.5a). This behavior again supports the our interpretation of a diffusion–limited critical current. Finally, the oscillations in the supercurrent as the 2DEG is depleted was investigated theoretically for a clean junction by Chrestin *et al.* [94] and are attributed to a changing interference criteria between Andreev– and normal–reflected particles in the junction. The oscillations were subsequently observed in two works by Takayanagi *et al.* [95, 96]. The quantitative theory for these oscillations have, to the best of our knowledge, only been developed for a clean, ballistic junction, and is thus not applicable to our system, except for use as a general statement about their origin.

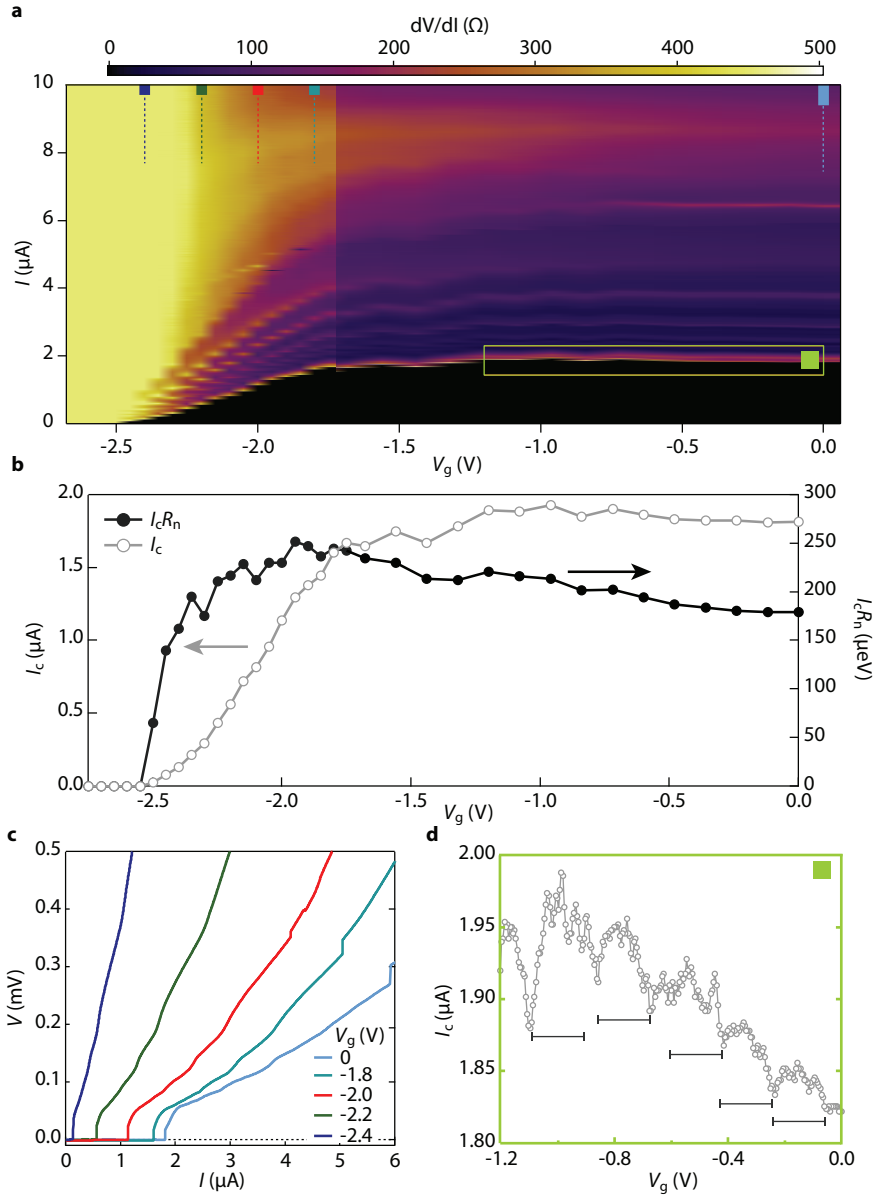

FIGURE 5.5: **a**, Differential resistance through the device as the gate is used to deplete the 2DEG. **b**, I_c and I_cR_n extracted from the plot in **a**. **c**, linecuts of the DC component for different values of V_g. The position of the cuts is indicated by dashed lines of same color in panel **a**. **d**, Zoomin on the oscillations of I_c, highlighted with the light green box in panel **a**. The horizontal bars are guides to the eye, all with identical lengths.

5.2.2 *Temperature dependence of the critical current*

To further elucidate the nature of the epi–Al SNS junction we have measured the temperature dependence of the critical current, as shown in Figure 5.6. For these measurements the gate is parked at $V_g = 0$ V. The temperature

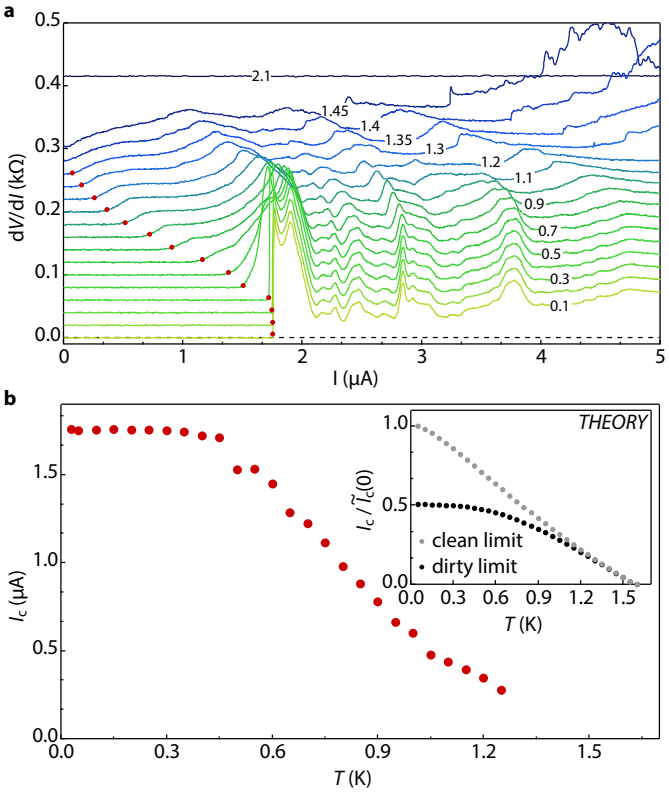

FIGURE 5.6: **a**, Resistance through the junction as the bias current is swept. The I_c is measured as the threshold when $dV/dI > 10\Omega$. At $T = 1.25$K there is no longer a zero voltage state, but the resistance is still decreased relative to the normal state. Each curve is offset by 20Ω except for $T = 0.1$K. **b**, Critical current extracted from data in panel **a**. Inset shows Equation (5.15) for $\mathcal{T} = 1$ (clean limit) and $\mathcal{T} = 0.01$ (dirty limit) with $T_c = 1.58$K and $\Delta = \Delta_{\mathrm{Al}}$.

dependence of the critical current was worked out in the clean limit and the dirty limit in the two original KO papers [88, 89]. Harberkorn and collaborators combined the two results a year later [97] and showed that for a junction with arbitrary transparency, the temperature dependence of the critical current is given by

$$I(\phi) = \max\left[\frac{\pi\Delta(T)}{2eR_n}\frac{\sin\phi}{\sqrt{1-\mathcal{T}\sin^2(\phi/2)}}\tanh\left(\frac{\Delta(T)}{2k_BT}\sqrt{1-\mathcal{T}\sin^2(\phi/2)}\right)\right] \tag{5.15}$$

For unity transmission, the Harberkorn result yields a critical current $\tilde{I}_c(0) = 5.7\ \mu$A using $\Delta = 230\ \mu$eV and $R_n = 100\ \Omega$. In the inset in Figure 5.6b we

have plotted Eq.(5.15) in the clean ($\mathcal{T} = 1$) and dirty ($\mathcal{T} \ll 1$) limit. Despite the quantitative difference in the value of I_c, it is clear that the measured junction exhibits a saturation of the critical current as the temperature is decreased, indicating the junction is best described by the diffusive limit [86, 93, 98]. The rich structure at finite voltage is the subject of Section 5.3.

5.2.3 *The Fraunhofer pattern*

If we expose the SNS to a perpendicular magnetic field, the role of the relative phases of the two superconductors become apparent in a beautiful diffraction–like pattern. In the simplest case of a short junction the origin of this diffraction can be seen as follows. The supercurrent *density* is related to the phase difference between the two superconducting banks via $J = J_c \sin\phi$, and the critical current is then

$$I_c = \max_\phi \left[\iint dydx J_c \sin\phi \right] \tag{5.16}$$

If a magnetic field is applied perpendicular to the SNS, the phase difference acquires an additional term

$$\phi \to \phi_0 + \frac{2\pi}{\Phi_0}\Phi, \tag{5.17}$$

where $\Phi = BWL$ is the flux through the junction with dimension $L \times W$, and $\Phi_0 = h/2e = 2.05\text{mT}/\mu\text{m}^2$ is the magnetic flux quantum. If the supercurrent density is assumed to be uniform across the junction, insertion of the phase in Equation (5.17) into Equation (5.16) yields the form of the critical current

$$I_c = I_c(0) \left| \frac{\sin(\pi\Phi/\Phi_0)}{\pi\Phi/\Phi_0} \right| \tag{5.18}$$

Thus, the supercurrent will oscillate with a period related to the area of the junction (via $\Phi = BWL$). In Figure 5.7a we have measured these oscillations for the device shown in Figure 5.4a. The interference pattern shows oscillating, but not periodic, behavior. We have extracted $I_c(B_\perp)$ as plotted in Figure 5.4b. Superimposed on the extracted critical current is Equation (5.18) for an area calculated using the values in Table 5. Only at larger fields do we find a rough agreement between the measurement and Equation (5.18) for $A = W \cdot L$. If we set an effective area $A^\star = 3.2A$ the first lobes line up with the theoretical prediction. We attribute this discrepancy at low fields to a flux focusing effect from the superconducting banks. Due to the Meissner effect, field lines will be expelled from the superconductor and lead to a larger effective field in the junction region, which in turn nullifies the simple interpretation offered by the width of the lobes reflecting the size of the junction [99, 100, 101]. As the field is increased the focusing

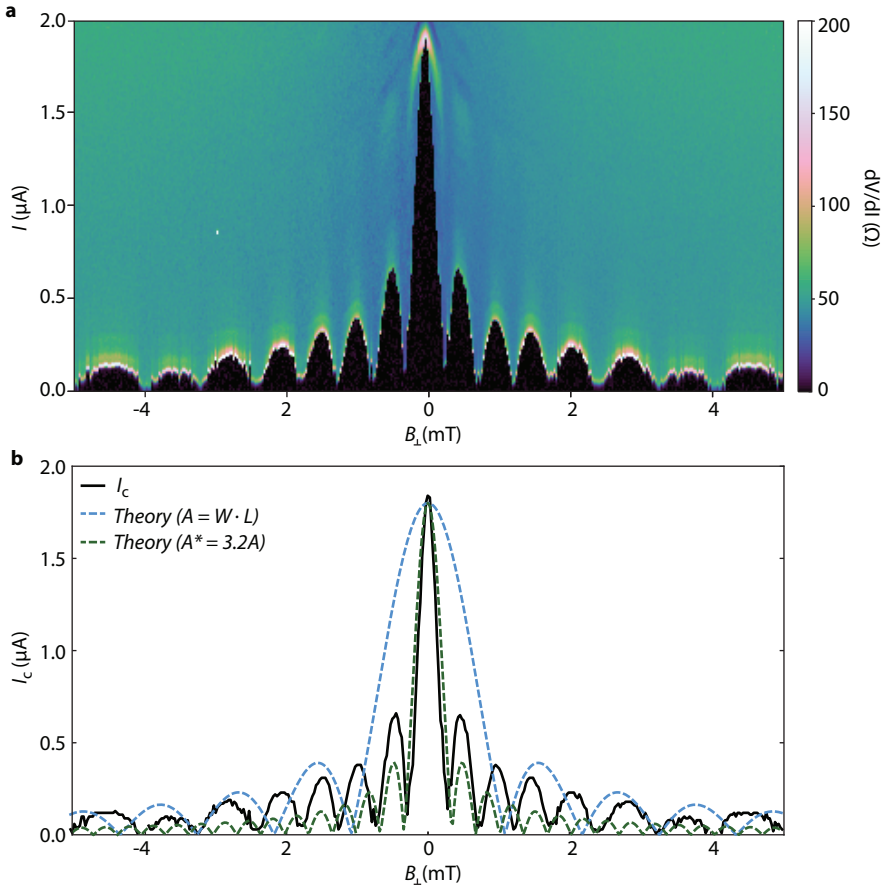

FIGURE 5.7: **a**, The measured Fraunhofer pattern. **b**, I_c vs $B_\perp$ extracted from the data in panel **a**. Equation (5.18) is superimposed using $A = W \cdot L$ from the lithographic dimensions, as well as a version of Equation (5.18) with an area $A^\star = 3.2A$, which matches the position of the first 3 minima.

effect will be less pronounced compared to the overall applied field, and the period for $A = W \cdot L$ matches the data better.

5.3 THE FINITE–VOLTAGE REGIME: MULTIPLE ANDREEV REFLECTION

We now focus on the finite–bias properties of the SNS structure. When there is a finite bias across the junction, the phase will wind according to

$$V_{\mathrm{dc}} = \frac{\hbar}{2e}\frac{d\phi}{dt} \tag{5.19}$$

This oscillating phase difference between the superconductors will average the AC supercurrent to zero. In Figure 5.8a an SNS structure with a bias eV_{sd} is shown. The sketch can be slightly misleading, since the density of states of the superconducting refer to quasiparticles while the density of states in the normal region is electrons. However, we can think of the N region as simply a region in which a quasiparticles from the filled negative band in the superconductor can be injected as an electron (or a hole). If a bias $eV_{\mathrm{sd}} > 2\Delta$ is applied, a charge can thus be transfered from the left to right

superconductor, since the kinetic energy offered to the carrier is greater than 2Δ. This will lead to a dissipative quasiparticle current. This is sketched in Figure 5.8b, where we have leveled the Fermi energy and instead include the bias by incrementing the energy in each traversal by eV_{sd}.

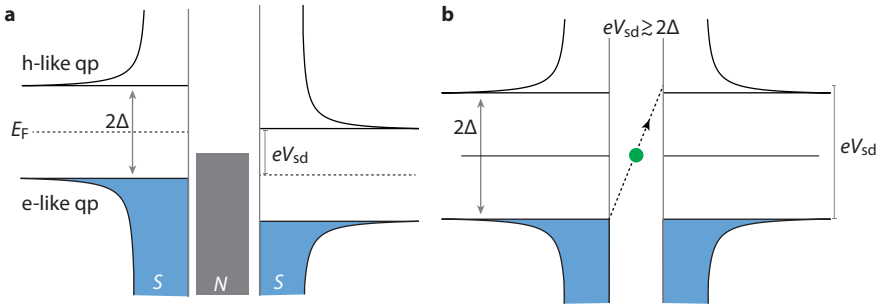

FIGURE 5.8: **a**, The SNS junction in a convoluted "real space / density of state"–space. The density of states i the superconductor is that of quasiparticles and the density of states in the normal region is for electrons. A bias eV_{sd} is applied across the junction. **b**, The SNS junction with an applied voltage eV_{sd} larger than the superconducting gap.

As the bias is lowered below Δ a particle will no longer be able to go directly from the quasiparticle band in the left superconductor, to the quasiparticle band in the right superconductor. Instead, it will Andreev reflect, have its energy mirrored around E_F at the cost of an added cooper pair in the right superconductor and gain an additional eV_{sd} on its way back as hole. The process is continued a number n times, until $neV_{sd} > 2\Delta$ and the particle can get out. This phenomenon of multiple Andreev reflection (MAR) was studied within a semi–classical picture [87, 102] and subsequently a full microscopic model was worked out [103, 104]. The $n = 2$ and $n = 3$ MAR processes is shown in Figure 5.9a and 5.9b. An n'th order multiple Andreev

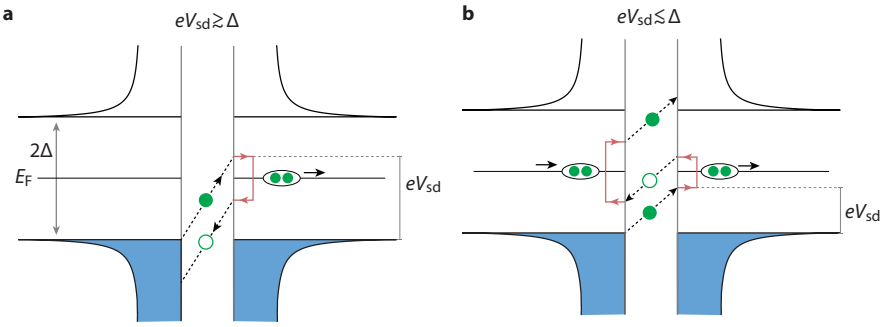

FIGURE 5.9: **a**, 2nd multiple Andreev reflection. **b**, 3rd order multiple Andreev reflections.

reflection process involves $n-1$ Andreev reflections and n traversals of the normal region. Thus, whenever the bias is swept through a value

$$eV_{sd} = \frac{2\Delta}{n} \tag{5.20}$$

a new resonance peak will occur in the conductance. Equation (5.20) is in principle satisfied for arbitrarily small V_{sd}, since n can be arbitrarily large. In practice, however, the MAR signature is limited by the transmission through the junction. The n'th order MAR scales with the transmission as $\mathcal{T}^n$, so that non–ideal interfaces severely limit the number of MARs observable.

By simultaneously recording the DC and AC voltage drop on the device in Figure 5.4a, we are able to map out these resonances. Figure 5.10a is the DC and AC components of the voltage drop as the bias current is ramped, and Figure 5.10 shows the MAR signature, by plotting the two components parametrically. Overlaid on the MAR resonance plot are vertical lines cor-

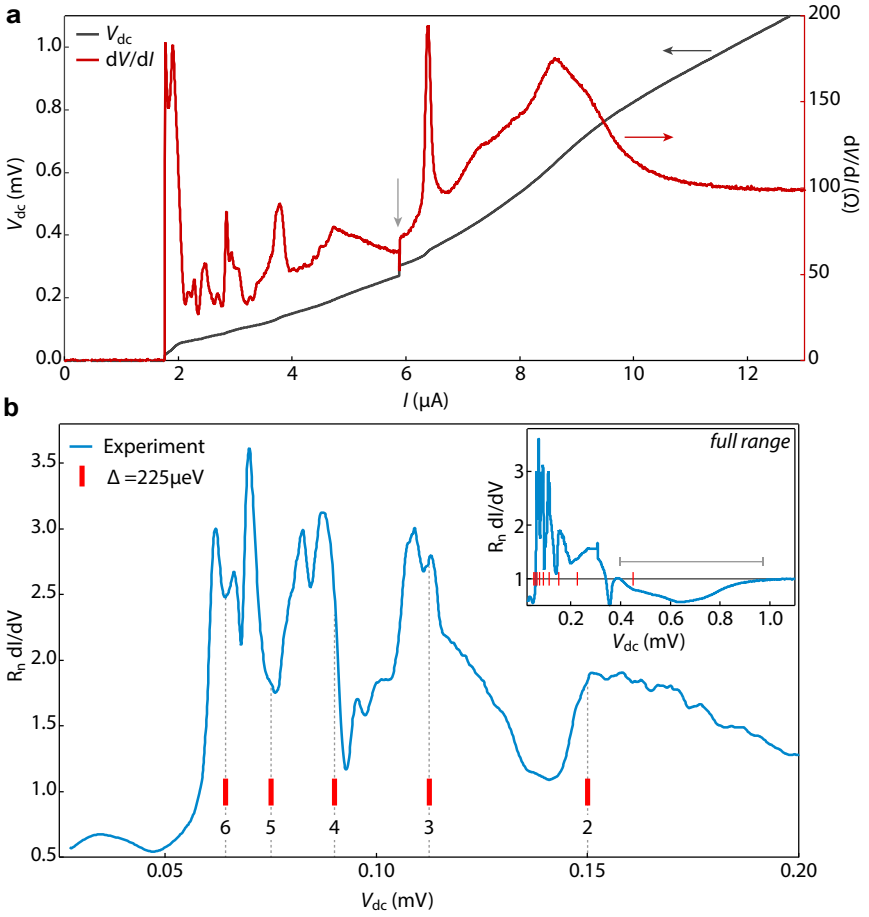

FIGURE 5.10: **a**, The DC and AC component of the voltage drop across the SNS device in current–bias configuration. The vertical gray arrow indicates the position we attribute to the aluminum film going normal. **b**, Resonant peaks in the conductance indicating the onset of multiple Andreev reflection normalized to $R_n = 100\ \Omega$. The numbers indicate the corresponding order of MAR. The prolonged dip below R_n for $eV_{sd} > 2\Delta$ is discussed in section 5.4.

responding to $n = \{2, 3, 4, 5, 6\}$ of Andreev reflections from $\Delta_{Al} = 235\ \mu$eV. It is evident that the MAR resonances measured in the experiment does not scale with Δ_{Al} as expected within the naive picture outlined above. Furthermore, we note that there are several more resonances than can be described

by a series of the form Δ/n, regardless of which single Δ is used. We'll defer a discussion of these observations to the next section.

Finally, the temperature dependence of the MAR resonances is shown in Figure 5.11. We observe that the bias value of the resonances decay and tend toward a temperature $T \approx 1.6$ K, close to the critical temperature of the aluminum film. For $T < 1$ K the temperature dependence is very weak,

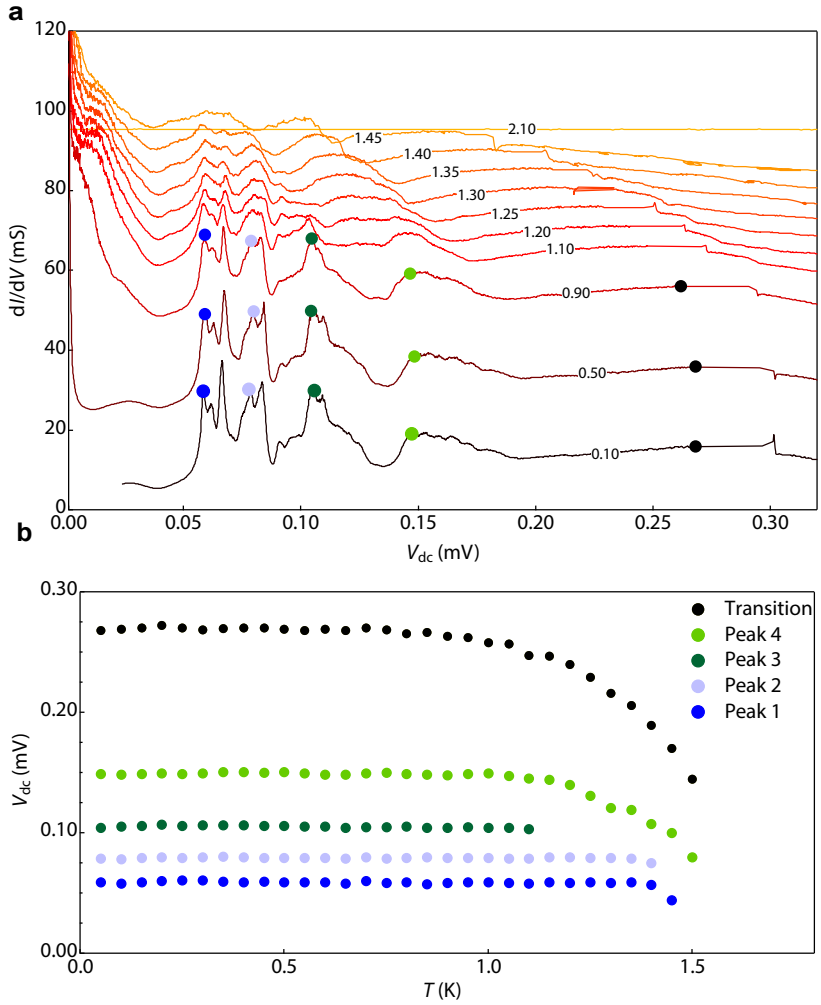

FIGURE 5.11: **a**, Temperature dependence of the MAR resonances as the temperature is increased. Labels indicate temperature at mixing chamber. All curves except $T = 0.1$ K are offset vertically. **b**, Tracking the peaks of the MAR resonances as the temperature is increased. The points labeled 'transition' correspond to the jump at 6 μA in Figure 5.9a.

and at higher temperatures, the unambiguous determination of the position of a peak is not possible (hence the different truncations of the curves in Figure 5.11). Efforts to understand the weak temperature dependence is currently underway. The low–bias conductance enhancement at $T > 1$ K is a precursor to the supercurrent [105]. At low temperatures, the very low–bias voltage signal is dominated by the first datapoint acquired as the voltage drop because finite, whose value is compounded by the heating effect of

switching to dissipative state. For this reason, the low temperature data is truncated below 0.025 mV.

5.4 WHERE IS THE SN INTERFACE IN EPI–AL/INAS DEVICES?

We devote this last section to a qualitative discussion of the nature of the SN interface in the epi–Al/InAs wafers. The majority of theoretical work on SN and SNS junctions consider a geometry where the N region *terminates* at the interface between the two materials. For the epi–Al/InAs devices this is manifestly not the case. Figure 5.12a,b compares the two geometries. An NS structure with an extending normal region, denoted SN′-N-N′S, was studied theoretically by several groups [106, 107, 108] and more recently in [109, 110]. Historically, some experimental observations on extended superconducting 2DEG geometries could not be reconciled with the picture of the S-N-S junction, but by invoking the SN′-N-N′S models, several features of the data were explained [27, 111, 112]. In the paper by Volkov and collab-

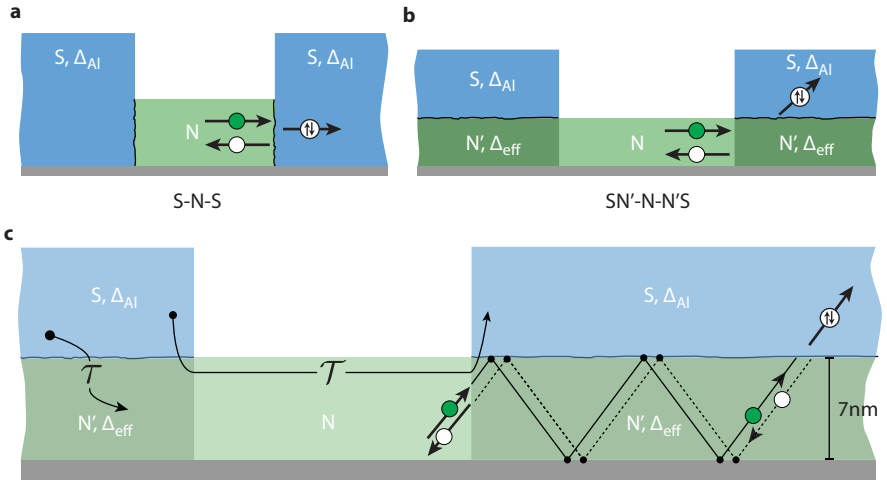

FIGURE 5.12: **a**, The canonical S-N-S geometry. Here, the interface between the materials is well–defined. **b**, The extended geometry studied in this thesis. **c**, Zoomin on the SN′-N-N′S geometry. The transmissivity going from left superconducting bank to right superconducting bank is denoted $\mathcal{T}$, while the transmissivity of the interface between S and the 2DEG immediately under it is denoted τ.

orators [108], the geometry of an S–planar 2DEG–S was explicity studied, and they demonstrated that the Green function in the normal region under the superconductor is renormalized to have an effective gap, denoted Δ_{eff} in its excitation spectrum. The phenomenon of effective gap was first introduced by McMillan [113]. The intuitive picture is that the properties of the standing wave in the z–direction under the aluminum is modified due to the boundary conditions, which admit Andreev reflections (with some probability) on one side, and a potential wall on the other side. The value of Δ_{eff} depend on the transmissivity τ of the interface underneath the superconductor. τ should be distinguished from the phenomenological $\mathcal{T}$ of the

previous section (see also Figure 5.12). It is interesting to note that there is still no pairing potential Δ_N due to phonon interactions within the quantum well, the appearance of Δ_{eff} is only a manifestation of Andreev reflections on one side of the quantum well.[1]

As sketched in Figure 5.12, electrons(holes) can extend deep into the region under the superconductor. As long as the process remain phase coherent, an electron can perform many attempts at undergoing Andreev reflection, before eventually coming out as a hole. With a phase coherence length of $l_\phi \sim 2\mu$m, and with a quantum well thickness of 7nm, the electron can scatter $\sim$300 times before geometry–enhanced retroreflection no longer occurs. Thus, even if the probability of single Andreev reflection is low, the geometry can assist the system so it appears (to carriers in the normal region N) that an electron going under the superconductor will be emitted as hole with a probability close to unity, despite the single–Andreev reflection probability is far from unity. Within this model we can somewhat reconcile the observations of the Andreev QPC and the results of the previous section: The Andreev QPC only probed the N-N′ interface, which, up to Fermi velocity mismatch, is an ideal interface where there is no barrier for momentum to be dumped in a normal reflection.

In a beautiful and simple experiment using the geometry from Figure 5.12b, Nguyen *et al.* [112] were able to deduce the average distance traveled in the N′–region before an Andreev process occurred. In an identical system, the same authors observed MAR behavior [111]. While their experiment did not show the rich resonance structure of Figure 5.10, they observed another salient feature of the data in Figure 5.10. When the bias voltage is between 0.4 mV and 1 mV the conductance is decreased relative to the normal state, as highlighted with the horizontal gray bar in the inset in Fig.5.10b. When a large bias is applied across the SN′-N-N′S system, the chemical potential difference between SN′ will vary locally as a function of distance from the N-N′ interface. At a certain point x' the chemical will fall below Δ_{Al}, and to the left of this point the current will be carried by dissipative quasiparticles, while to the right Andreev reflection will occur. The Andreev reflected electron now has to traverse back to the N-N′ interface, and during that time can recombine with either electrons in the InAs bulk or undergo Andreev reflection again. Nguyen *et al.* speculate the reduction in conductance can be attributed to Andreev reflected particles at $x > x'$ being recaptured by the superconductor, before reaching the N-N′ region.

1 There is an unfortunate collusion of words in this context. Sometimes the *proximity effect* refers to a modification of a pre–existing pairing potential, as in the case of two superconductors with different T_c's coupled. Recently, using STM techniques the spatial profile of the pairing potential in two superconducting materials with $T_{c1} > T_{c2}$ was measured at an intermediate temperature and the proximity effect had altered the gap in the density of states both superconductors [71]. For the NS and SNS structures, there is never a phonon–interaction within the semiconductor that is renormalized due to the proximity effect. Rather, the density of states in the semiconductor is modified and will have a gap in the local density of states commensurate with the superconducting gap. This is sometimes referred to as an induced gap and it appears because of the proximity effect.

The result of two gaps in the density of states Δ_{Al} and Δ_{eff} would also lead to the addition of a new set of MAR resonances: $2\Delta_{eff}/n$, $(\Delta_{Al} - \Delta_{eff})/n$ and $(\Delta_{Al} + \Delta_{eff})/n$ [107, 27]. By setting $\Delta_{Al} = 225\mu$eV as measured from T_c of the film, we choose $\Delta_{eff} = 165\mu$eV, which lines up with several of the resonance, as shown in Figure 5.13. Setting $\Delta_{eff} = \Delta^\star = 190\mu$eV (the gap measured by tunnel spectroscopy in Chapter 4) does not line up with any of the measured resonances. Despite the litany of vertical lines in Figure 5.13, there are still several unexplained resonances in the data. At the time of writing the origin of these is unresolved, but we are working on numerical and analytical approaches to understand these features in greater detail.

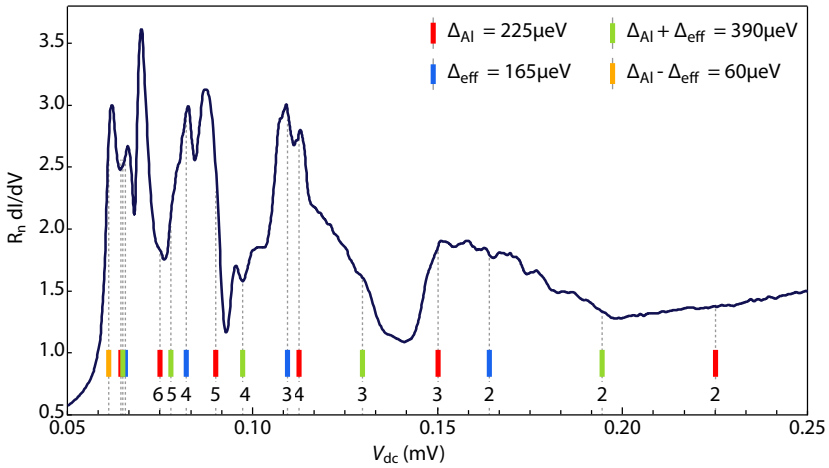

FIGURE 5.13: Multiple Andreev reflections due to the appearance of two superconducting gaps in the system. The resonance corresponding to Δ_{eff} and the combinations $\Delta_{Al} - \Delta_{eff}$ and $\Delta_{Al} - \Delta_{eff}$ is shown. Despite including these extra terms, there are still several resonances that seem unexplained.

5.5 CONCLUSION

The supercurrent in our 200 nm long Josephson junction in the epi–Al/InAs material is dominated by diffusive transport, as evident through the gating–properties and temperature dependence of the critical current. The excess current in our junction is comparable to theoretical estimates for an SNS junction in the diffusive regime, but with ideal Andreev reflection [92], which indicates that reflection from the NS interface is dominated by Andreev processes.

The model of multiple Andreev reflection as coherent scattering from the sides of an S-N-S junction with a well–defined Δ is not able to account for the resonances we observe when a bias is applied across the epi-Al/InAs junction. There are several outstanding questions regarding the interpretation of the resonances, and we are currently developing a coherent theoretical framework to understand this behavior.

Part III

MAJORANA FERMIONS IN NANOWIRES WITHOUT SPIN–ORBIT COUPLING

This part is dedicated to a theoretical exploration into the feasibility of realizing Majorana bound states in nanowires without spin–orbit coupling. We explicitly show the topological properties of Kitaevs *p*–wave nanowire toy model, and proceed to derive analytically, and simulate using realistic parameters, that a nanowire with *s*–wave superconductivity exposed to a locally oscillating magnetic field also supports a topological phase.

6

MAJORANA FERMIONS IN 1D QUANTUM WIRES

The experimental work in the preceding chapters was broadly motivated by the notion that exotic quasiparticles (Majorana bound state) exist at the interface between a semiconducting material with spin–orbit coupling (InAs/InGaAs), in the presence of an external magnetic field, coupled to an *s*–wave superconductor (aluminum). In this chapter we dig into the detailed microscopic theory for the existence of Majorana fermions at this interface. In particular, we will study the Kitaev model of a nanowire proximal to a *p*–wave superconductor [4]. Such a system can, for specific parameters, harbor unpaired Majorana fermions at its ends. We will then introduce the notion of a topological quantum number, used to quantify the existence or absence of Majorana fermions. Two proposals that realizes the Kitaev model without using the elusive *p*–wave superconductor came independently from Oreg *et al.* [5] and Lutchyn *et al*. [6]. These proposals form the basis of many of the recent experimental signatures of Majorana bound states [12, 13, 14]. Some general features of these proposals are reviewed, before presenting our main theoretical result: Majoranas can exist in quantum wires without intrinsic spin–orbit coupling, when the latter is instead imitated by a locally rotating magnetic field, realized by micromagnets. In developing the model we have taken care to use experimentally realistic parameters.

6.1 KITAEVS *p*–WAVE TOY MODEL

Consider a 1D quantum wire placed on top of a 3D spinless superconductor. By "spinless" we mean that spins of the cooperpairs are aligned, as is the case for *p*–wave superconductors where the condensate is made of triplet–paired electrons. The setup is sketched in Figure 6.1. The proximity to the superconductor will induce a gap in the density of states of the wire. In order to interpret the recent experimental results on nanowires coupled to superconductors, a considerable effort has been put into how to properly model this proximity gap in the hamiltonian describing the nanowire [67,

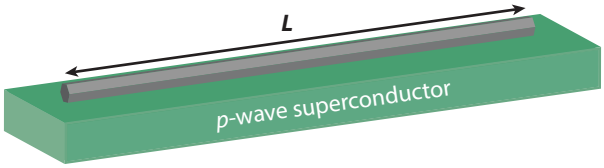

FIGURE 6.1: The semiconducting nanowire has, by the proximity to the p–wave superconductor, an effective gap in the density of states.

114, 115]. However, for the present purposes, we simply stick a Δ in the lattice hamiltonian for the wire,

$$H = \sum_{j=0}^{L} \left(-t \left(c_j c_{j+1}^\dagger + c_{j+1}^\dagger c_j \right) - \mu \left(c_j^\dagger c_j - \frac{1}{2} \right) + \Delta_p c_j c_{j+1} + \Delta_p^* c_j^\dagger c_{j+1}^\dagger \right), \tag{6.1}$$

where Δ_p is the p–type pairing term, t is the kinetic energy and μ is the chemical potential in the wire. The need for the p–wave superconductivity for this model to have any hope of realizing Majorana fermions can be seen as follows: For the quasiparticles to obey $\gamma^\dagger = \gamma$, they should be effectively spinless, i.e. formed by combinations of electrons and holes with identical spin. For s–wave superconductivity the pairing term is given by $\Delta_s = \langle \psi(\boldsymbol{r})_\sigma^\dagger \psi(\boldsymbol{r})_{-\sigma}^\dagger \rangle e^{i\phi}$, so Andreev reflection from the interface will entail a spin–flip. Since Majoranas are build by standing waves from Andreev reflection on the superconducting interface (see section 6.3.1) the quasiparticles from an interface to an s–wave superconductor have no hope of forming Majorana bound states. As we shall see below, with the help of a Zeeman field + spin orbit coupling, or Zeeman field + rotating magnetic field, the quasiparticles can become effectively spinless. In any case, for the toy model here, the use of p–wave systems which has pairing of the form $\Delta_p = \langle \psi(\boldsymbol{r})_\sigma^\dagger (-i\hbar\nabla) \psi(\boldsymbol{r})_\sigma^\dagger \rangle e^{i\theta(\boldsymbol{r})}$, the standing waves formed by retroreflected electrons and holes involved in the Andreev process have identical spin. For the p–wave the asymmetry of the overall wavefunction is ensured not by opposite spin, but by the oddness of the real space wavefunction. The non–local nature of the p–wave pairing is evident in Equation (6.1) where neighboring sites are coupled. We can now build Majorana operators in this system, made from fermionic operators c and $c^\dagger$ and safely disregard the spin. The phase–dependence of the order parameter can be absorbed with the following basis change

$$\begin{aligned} \gamma_{2j-1} &= e^{i\theta/2} c_j + e^{-i\theta/2} c_j^\dagger \\ \gamma_{2j} &= -ie^{i\theta/2} c_j + ie^{-i\theta/2} c_j^\dagger, \end{aligned} \tag{6.2}$$

note that γ_{2j-1} and γ_{2j} act on the same fermionic site and satisfy $\gamma^\dagger = \gamma$. In this basis the Hamiltonian Equation (6.1) is

$$H = \frac{i}{2}\sum_{j}^{L}\left(-\mu\gamma_{2j-1}\gamma_{2j} + (t+|\Delta|)\,\gamma_{2j}\gamma_{2j+1} + (-t+|\Delta|)\gamma_{2j-1}\gamma_{2j+2}\right) \quad (6.3)$$

Two limiting cases serve to show a remarkable feature of Equation (6.3):

$|\Delta| = t = 0$ AND $\mu < 0$: In this limit Equation (6.3) reduces to

$$H_0 = -\mu\frac{i}{2}\sum_{j}^{L}\gamma_{2j-1}\gamma_{2j} = -\sum_{j=0}^{L}\mu\left(c_j^\dagger c_j - \frac{1}{2}\right) \quad (6.4)$$

This corresponds to pairing each Majorana operator on every site with its partner, as shown in Figure 6.2c.

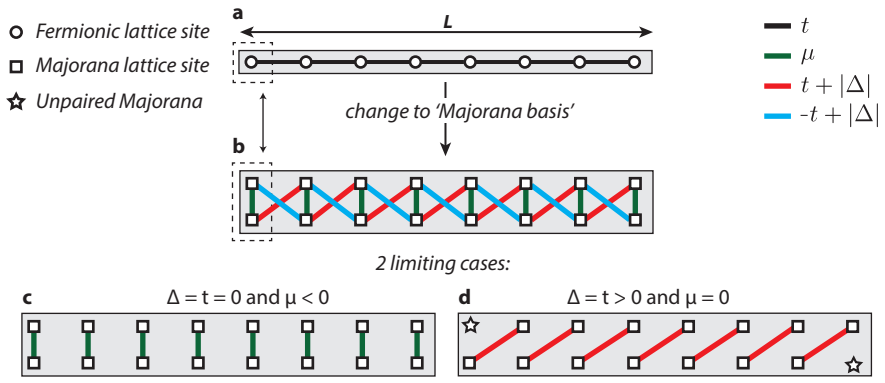

FIGURE 6.2: Illustration of the Majorana basis change in Equation (6.3). **a**, Lattice sites on the wire in the fermionic basis. **b**, Doubling the number of lattice sites and introducing the Majorana basis. **c**, The limit of no superconducting gap. **d**, The limiting case of $\Delta = t$ which has unpaired Majorana end states.

$|\Delta| = t > 0$ AND $\mu = 0$: In this case, the hamiltonian for the wire is given by

$$H_m = it\sum_{j}^{L}\gamma_{2j}\gamma_{2j+1} \quad (6.5)$$

This shows more interesting features, since now a Majorana from site j is paired with a Majorana from site $j+1$, c.f. Equation (6.2). A basis change back to regular fermionic sites yields

$$\left.\begin{aligned}\tilde{c}_j &= \tfrac{1}{2}\left(\gamma_{2j} + i\gamma_{2j+1}\right)\\ \tilde{c}_j^\dagger &= \tfrac{1}{2}\left(\gamma_{2j} - i\gamma_{2j+1}\right)\end{aligned}\right\} \rightarrow H_m = 2t\sum_{j=1}^{L-1}\left(\tilde{c}_j^\dagger\tilde{c}_j + \frac{1}{2}\right). \quad (6.6)$$

Note that site $j = 0$ and $j = L$ does not appear in the sum. At these sites there is still half a fermion, i.e. a Majorana particle, see

Figure 6.2d. We denote the corresponding operators by $\gamma_L = \gamma_{j=0}$ and $\gamma_R = \gamma_{j=L}$

It is now possible to build a (non–local) fermion of these two states as $c_{\mathrm{nl}} = N(\gamma_L + i\gamma_R)$, with N appropriate normalization. Since the ground state satisfies $\tilde{c}_j|\psi\rangle = 0$ for $j = 1, \ldots, L-1$ there are *two* states (denote them $|\psi^e\rangle$ and $|\psi^o\rangle = c_{\mathrm{nl}}^\dagger|\psi^e\rangle$) that satisfy this property. In the limit $L \to \infty$ these two states are degenerate, since the overlap of the wavefunctions of $|\psi^e\rangle$ and $|\psi^o\rangle$ is exponentially suppressed with L. The two states can be distinguished by the occupancy of the non–local fermion. To quantify the parity we introduce the operator P

$$P = 1 - 2c_{\mathrm{nl}}^\dagger c_{\mathrm{nl}} = -i\gamma_L\gamma_R \tag{6.7}$$

The last equality follows from insertion of the definition of c_{nl}. It is easily verified that P distinguishes between $|\psi^e\rangle$ and $|\psi^o\rangle$ with a sign

$$P|\psi^e\rangle = |\psi^e\rangle \quad , \quad P|\psi^o\rangle = \left(1 - 2c_{\mathrm{nl}}^\dagger c_{\mathrm{nl}}\right) c_{\mathrm{nl}}^\dagger|\psi^e\rangle = -|\psi^o\rangle \tag{6.8}$$

Kitaevs toy model thus harbors a degenerate groundstate with two quasiparticle excitations that obey $\gamma^\dagger = \gamma$. The parity of the ground state is determined by the eigenvalue of P.

For a Hamiltonian H describing non–interacting electrons in a translationally invariant system, the transition to the topological phase, with unpaired Majoranas, can be quantified by calculating the topological quantum number $\mathcal{M}(H)$ [116, 117]:

$$\mathcal{M}(H) = \mathrm{Pf}(\mathcal{U}H(k=0)) = \begin{cases} < 0 & \text{Topological regime} \\ > 0 & \text{trivial regime} \end{cases} \tag{6.9}$$

Here $\mathrm{Pf}(\cdot)$ is the Pfaffian, which is defined via $\mathrm{Pf}^2(A) = \det A$ for A skew–symmetric, i.e. $A_{ij} = -A_{ij}$ and zeros on the diagonal. $\mathcal{U}$ is the unitary part of the particle–hole operator. In the present basis, without spin degrees of freedom, the particle–hole symmetry operator is $\Xi = \tau_x K$, where τ_x is a Pauli matrix in p–h space, and K is the operator of complex conjugation. A p–h invariant Hamiltonian satisfies $\Xi H(k)\Xi^{-1} = -H(-k)$. The unitary part of Ξ is thus simply τ_x.

To evaluate $\mathcal{M}$ we start by a fourier–transformation of Equation (6.1) using

$$c_j = \sum_k e^{-ikj} c_k, \quad c_j^\dagger = \sum_k e^{ikj} c_k^\dagger, \tag{6.10}$$

which yields

$$H = \sum_k \left(-2t\cos(k) - \mu\right) c_k^\dagger c_k + \Delta\left(c_k^\dagger c_{-k}^\dagger e^{ik} + c_k c_{-k} e^{-ik}\right). \tag{6.11}$$

Introducing the spinor $\Psi_k = (c_k \; c_{-k}^\dagger)^T$, rearranging indices and restricting the sum to run over positive k, Equation (6.11) can be written as $H = \sum_{k>0} \Psi_k^\dagger \mathcal{H}(k) \Psi_k$, where

$$\begin{aligned} \mathcal{H}(k) &= \begin{pmatrix} -2t\cos(k) - \mu & -2\Delta i \sin(k) \\ 2\Delta i \sin(k) & 2t\cos(k) + \mu \end{pmatrix} \\ &= -\xi_k \tau_z + 2\Delta \sin(k) \tau_y \end{aligned} \tag{6.12}$$

This equation is a variation on the general Bogoliubov-de Gennes equation introduced back in Equation (2.14). Sandwiching $\mathcal{H}$ between Ξ and Ξ^{-1} shows that $\mathcal{H}(k)$ is particle–hole symmetric (as it better be).

The spectrum of $\mathcal{H}(k)$ is found by direct diagonalization to be

$$\epsilon(k) = \pm\sqrt{(2t\cos(k) + \mu)^2 + 4\Delta^2 \sin^2(k)} \tag{6.13}$$

In Figure 6.3a and 6.3b the spectrum is plotted for two different values of μ. At $\mu = -2t$ the gap closes and the wire undergoes a topological phase transition. We see this by evaluating the quantum number $\mathcal{M}$ from Equation (6.9). First the Hamiltonian is rotated with the unitary part of the particle–hole operator and the limit $k = 0$ is taken,

$$\mathcal{U}H(k=0) = \tau_x H(k=0) = \begin{bmatrix} 0 & 2t + \mu \\ -2t - \mu & 0 \end{bmatrix} \tag{6.14}$$

This matrix is 2×2 and skew–symmetric so the is Pfaffian well–defined and particularly easy to evaluate since $\mathrm{Pf} \left(\begin{smallmatrix} 0 & -c \\ c & 0 \end{smallmatrix}\right) = c$, so we get

$$\mathcal{M} = -2t - \mu = \begin{cases} < 0 & \text{for } \mu > -2t \\ > 0 & \text{otherwise} \end{cases} \tag{6.15}$$

Which shows the phase transition at $\mu = -2t$. The topological phase is also bounded from above when $\mu = 2t$. At this point the gap closes at $k = \pm\pi$ and since $\cos(k \pm \pi) = -\cos(k)$ evaluation of $\mathcal{M}$ yields the condition $\mu < 2t$ to be in the topological phase.

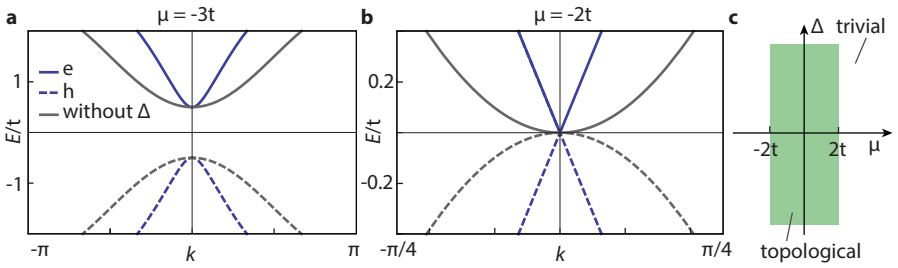

FIGURE 6.3: **a**, Spectrum of the Kitaev wire outside the topological regime. **b**, Dispersion of the Kitaev wire exactly at the phase transition. **c**, Schematic of the topological regime for $\mu < |2t|$.

Now that we've established that the Kitaev toy model is in the topological state for $\mu < |2t|$, the next question is: What are the zero–energy eigenstates associated with this phase? As is evident from Figure 6.3b, the superconducting gap Δ serves to linearize the spectrum close to the phase transition, and we can use this as the starting point.

If the chemical potential varies as a function of position, the nature of the zero–energy states associated with the phase transition are particularly illuminating. To this end, we set $\mu = -2t + \mu(x)$, such that for $\mu(x) > 0$ the wire is topological and for $\mu(x) < 0$ the wire is in the trivial state. If we linearize around $k \sim 0$, then Equation (6.12) in real space reads

$$H(x) = \begin{bmatrix} -\mu(x) & -2\Delta\frac{d}{dx} \\ 2\Delta\frac{d}{dx} & \mu(x) \end{bmatrix} \tag{6.16}$$

where the basis is $\varphi(x) = (u(x)\ v(x))^T$. The zero–energy states are the solutions to the coupled differential equations

$$\begin{aligned} -\mu(x)u(x) - 2\Delta\frac{d}{dx}v(x) &= 0 \\ 2\Delta\frac{d}{dx}u(x) + \mu v(x) &= 0 \end{aligned} \tag{6.17}$$

which admits two solutions,

$$\phi_1 = e^{\beta(x)}\begin{pmatrix} 1 \\ 1 \end{pmatrix} \quad , \quad \phi_2 = ie^{-\beta(x)}\begin{pmatrix} 1 \\ -1 \end{pmatrix} \tag{6.18}$$

where $\beta(x) = \int^x dx'\delta(x')/2\Delta$. Whether ϕ_1 or ϕ_2 is the normalizable solution depends on details of the shape of $\mu(x)$. However, the states in Equation (6.18) have three crucial features. They are their own particle–hole partner, i. e. $\phi_1^\dagger = \Xi\phi_i$, they live at zero energy and they are located around wherever $\mu(x)$ changes sign. In the physical picture of a wire, this would correspond to the ends of the wire, or at the ends of regions where the density is modulated by an electrostatic gate. These are the unpaired Majorana end states. If $\mu(x)$ has the opposite sign in Eq.(6.17) (i.e. the wire is in the trivial regime), there exists no normalizable solutions at zero energy. Finally, to see that the states satisfy the "canonical Majorana relation" ($\gamma^\dagger = \gamma$) from Chapter 1, we can rewrite the states in Equation (6.18) in k–space, $\gamma_i = \int dx\phi_i^\dagger\Psi_k$, with $\Psi_k = (c_k\ c_{-k}^\dagger)^T$ and we see that indeed the zero–energy solutions to Kitaevs toy model are Majorana quasiparticles.

6.2 NANOWIRES WITH SUPERCONDUCTIVITY AND SPIN ORBIT COUPLING

In this section we study the proposal due to Oreg, Refael & von Oppen [5]. A related idea was introduced at the same time by Lutchyn, Sau & Das

Sarma [6]. The former is the most closely related for our proposal, and we proceed by investigating their model, and in particular show that it maps to the Kitaev model, indicating that for certain parameter–values the Oreg model supports Majorana Fermions. Oreg *et al.* considered a geometry as the one shown in Figure 6.4. A nanowire with Rashba–type spin–orbit coupling is deposited on a slab of s–wave superconductor. Again, it is assumed that the Andreev reflection process is ideal, and the effect of the superconductor can be included by naively sticking a Δ in the hamiltonian. The electron is confined in the transverse direction, and we consider only states propagating along y.

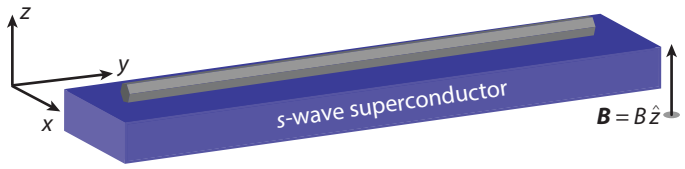

FIGURE 6.4: The system discussed by Oreg *et al.*, with the Hamiltonian given by Equation (6.19). The wire is superconducting due to the proximity–effect with the s–wave superconductor.

Using the Nambu basis $\Psi = \left(\psi_\uparrow \ \psi_\downarrow \ \psi_\downarrow^\dagger \ -\psi_\uparrow^\dagger\right)^T = \left(\bar{\psi} \ \Theta\bar{\psi}^\dagger\right)^T$, where Θ is the time–reversal operator, $\Theta = i\sigma_y K$, and σ_y is a Pauli matrix in spin–space, the Hamiltonian for the system in Figure 6.4 is given by $H = \int dy \Psi^\dagger \mathcal{H} \Psi$ where

$$\begin{aligned} \mathcal{H} &= \left[\frac{k_y^2}{2m} - \mu + \alpha(\boldsymbol{k} \times \boldsymbol{E}) \cdot \boldsymbol{\sigma}\right] \tau_z + B\sigma_z + \Delta\tau_x \\ &= \left[\frac{k^2}{2m} - \mu + uk\sigma_x\right] \tau_z + B\sigma_z + \Delta\tau_x \end{aligned} \tag{6.19}$$

where in the last equation the subscript y was dropped and it is assumed that the electrical field that gives rise to the Rashba spin–orbit interaction is oriented along the x–axis (see Figure 6.4). The velocity u is related to Rashba parameter by $\alpha = \hbar u$. Throughout this section we take the B field perpendicular to the Rashba field. In the basis of time–reversed states the p–h symmetry operator is now given by $\Xi = \sigma_y \tau_y K$, where σ_y is included because of the spin–component. Inspection shows $\Xi \mathcal{H}(k) \Xi^{-1} = -\mathcal{H}(-k)$. We again expect all eigenenergies to come in $\pm$ pairs.

6.2.1 *The helical state in nanowires*

Even without the superconducting pairing the spectrum of Eq.(6.19) is exceedingly interesting, and exhibits rich features which precede the Majorana physics. The spectrum is given by

$$E_\pm = \frac{k^2}{2m} + s\sqrt{B^2 + (uk)^2}, \tag{6.20}$$

where $s = \pm 1$ for spin up/down. The spectrum is plotted in Figure 6.5. For $u > 0$ the minima of the dispersion is offset, and the new k for $E(k)$ minimal is

$$\frac{d}{dk}\left(\frac{k^2}{2m} \pm up\right) = 0 \Rightarrow k_{so} = \mp mu \tag{6.21}$$

which yields $E_{so} = E(k_{so}) = \frac{1}{2}mu^2$. If the externally applied magnetic field is perpendicular to the spin–orbit field, it opens a gap in the spectrum at $k = 0$. If we park the chemical potential in this gap, the carriers will have their spin locked to the momentum. This helical mode is the 'su-

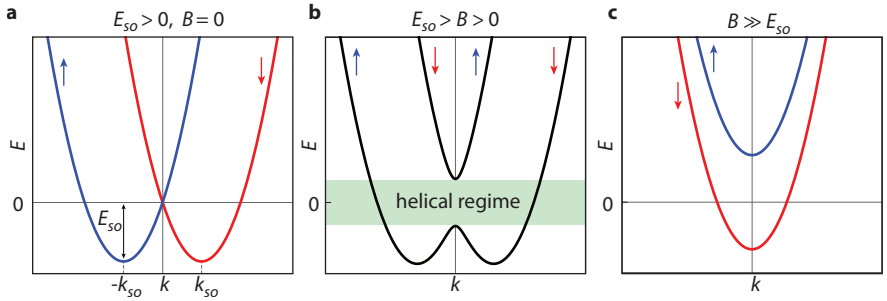

FIGURE 6.5: **a**, The spin–orbit interaction shifts the parabolas of each spin species. **b**, The combination of magnetic field and spin–orbit interaction creates an avoided crossing the spectrum. The arrows indicate the spin–direction far from the avoided crossing. **c**, For fields much greater than the spin–orbit field, each band is fully polarized along the external field.

perconductorless' prelude to the Majorana fermion in the Oreg model. An experimental signature of the helical gap is a non–monotonic increase in the conductance through a quantum point contact [118, 119] as μ is varied. The initial project undertaken as part of the experimental work in this report was focused on observing the helical state. By using the 2D electron gas in InSb – a material with a nominally large g–factor and large spin–orbit coupling – we hoped to form a QPC and observe the non–monotonic behavior indicative of the helical gap. However, InSb 2DEGs is a notoriously finicky class of materials, and even the mesoscopic basics (such as good, reproducible ohmic contacts and gating without appreciable hysteresis) is still not trivial [120, 121, 122]. At QDev we never succeeded in making stable gateable structures without significant hysteresis (and not for want of trying). However, we fabricated a hallbar in a wafer grown by Mike Santos of University of Oklahoma, and measured the weak antilocalization signature. A collaborator used the ILP model [123] to fit weak antilocalization data and extracted $E_{so}^{InSb} = 2.9\ \mu$eV$= 33$ mK. With such a small E_{so}, we abandoned hope of measuring the helical gap in this InSb wafer. It is currently not understood why the we measured spin–orbit was so significantly reduced from the theoretical expectation, given that from a pure band structure calculation $\alpha_{InSb} \approx 4.5\alpha_{InAs}$ and $\gamma_{InSb} \approx 28\gamma_{InAs}$ [36]. In a separate InSb wafer, fabricated by HRL Laboratories [122], we succeeded in measuring the pinchoff curve in a split–gate QPC geometry with $W = 300$ nm and no

gate leakage. The measurements were performed at 6 K in a dunker setup, and all device processing and fabrication was done by HRL, except for QPC gate deposition. The pinchoff was still hysteretic, see Figure 6.6, and we observed no signs of quantized conductance, despite the InSb wafers having a mobility $\mu_{\text{InSb}} \approx 200.000\text{cm}^2/\text{Vs}$ and density $n_{\text{InSb}} \approx 2 \cdot 10^{11}\text{cm}^{-2}$ [122]. As

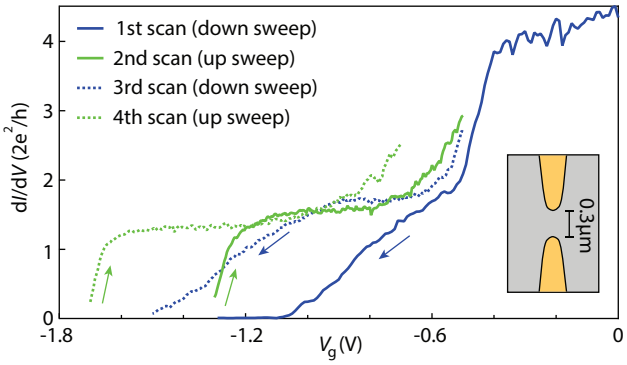

FIGURE 6.6: Pinchoff curve in a 30nm InSb quantum well with a standard split–gate QPC geometry with a separation of 300nm measured at 6K in a helium dunker setup.

mentioned in the introduction, the compounding materials problems with the InSb 2DEG lead us to abandon those wafers in favor of the epi–Al/InAs wafers.

6.2.2 *Majorana fermions in the Oreg model*

We now return to the full Oreg model, and show that it maps to the Kitaev model, and thus supports Majorana bound states. The dispersion of the full Oreg hamiltonian in Equation (6.19) is

$$E_{\pm}^2 = \xi^2 + B^2 + (uk)^2 + \Delta^2 \pm \sqrt{(uk)^2\xi^2 + B^2(\Delta^2 + \xi^2)}, \tag{6.22}$$

where $\xi = \frac{k^2}{2m} - \mu$. At small k the gap in the spectrum is particularly clear

$$\begin{aligned} E_{\pm}(k \sim 0) &= \sqrt{B^2 + \Delta^2 + \mu^2 \pm 2B\sqrt{\Delta^2 + \mu^2}} \\ &= \sqrt{\Delta^2 + \mu^2} - B \end{aligned} \tag{6.23}$$

This indicates that the gap closes exactly when $B = \sqrt{\Delta^2 + \mu^2}$. In Figure 6.7 the dispersion is plotted for three different cases: 1; in the absence of the superconducting pairing, 2; in the presence of the pairing and 3; at the gap–closing point $B = \sqrt{\Delta^2 + \mu^2}$. The linearity of the spectrum at small k at this phase transition looks very similar to the behavior of the Kitaev wire at $\mu = 2t$, see Figure 6.3. To confirm this we proceed to linearize the Oreg model for the two lowest bands, highlighted in the dashed box in Figure 6.7b and show that this subspace maps onto the Kitaev model.

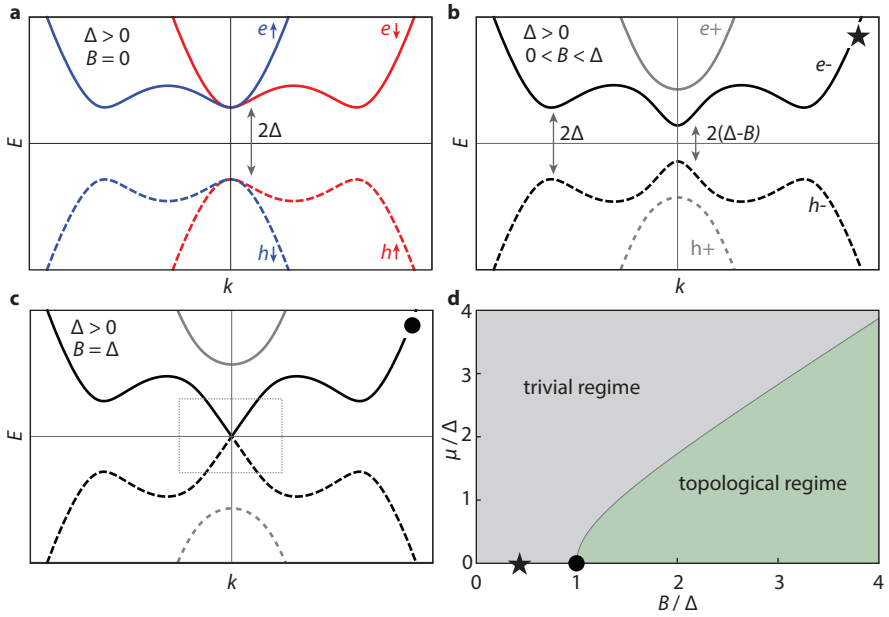

FIGURE 6.7: **a**, The dispersion relation of the Oreg wire with $E_{so} > 0$ in the absence of an applied magnetic field. The superconducting pairing makes a gap in the spectrum. The dashed lines are the hole–bands. **b**, When a magnetic field is applied perpendicular to the spin–orbit field, the gap at $k = 0$ closes. **c**, At the phase–transition $B = \Delta$ the dispersion is linear at $k = 0$ and the low–energy sector can system can be mapped onto the Kitaev chain. **d**, The phase diagram of the Oreg wire. The $\star$ and $\bullet$ indicate the parameters used in **b** and **c**.

We start by leaving aside the superconductivity, so that electron and hole blocks decouple,

$$\mathcal{H}_0 = \tau \frac{k^2}{2m} + \tau up\sigma_x + B\sigma_z, \tag{6.24}$$

with $\tau = \pm 1$ corresponding to electrons/holes respectively. $\mathcal{H}_0$ is diagonalized by the unitary transformation

$$U = \exp\left(-i\gamma/2\sigma_y\right) = \cos\frac{\gamma}{2} - i\sigma_y \sin\frac{\gamma}{2}, \tag{6.25}$$

where $\sin\gamma = up/\sqrt{(uk)^2 + B^2}$ and $\cos\gamma = B/\sqrt{(uk)^2 + B^2}$. In the new basis, $\mathcal{H}_0$ takes the form

$$\widetilde{\mathcal{H}}_0 \to U\mathcal{H}_0U^{-1} = \tau\frac{k^2}{2m} - \sqrt{(uk)^2 + B^2}\sigma_z \tag{6.26}$$

This basis is sometimes referred to as the *helical basis*, with elements denoted $\{|e+\rangle, |e-\rangle, |h-\rangle, |h+\rangle\}$ (labeled in Figure 6.5b), and the eigenstates are given by

$$|\tau+\rangle = U^\dagger \begin{pmatrix} 1 \\ 0 \end{pmatrix} = \begin{pmatrix} \cos\gamma/2 \\ -\tau\sin\gamma/2 \end{pmatrix}, |\tau-\rangle = U^\dagger \begin{pmatrix} 0 \\ 1 \end{pmatrix} = \begin{pmatrix} \tau\sin\gamma/2 \\ \cos\gamma/2 \end{pmatrix} \tag{6.27}$$

The gap between the two helical states $|e-\rangle$ and $|h-\rangle$ at $k = 0$ scales with $\Delta - B$, as highlighted in the dashed box in Figure 6.5c, for the special case $\Delta = B$. By projecting the original Hamiltonian in Equation (6.19) onto the subspace spanned by $\{|e-\rangle, |h-\rangle\}$ yields the 2×2 matrix describing the low–energy sector of the system:

$$\widetilde{\mathcal{H}}_{2\times 2} = \left(\frac{k^2}{2m} + \sqrt{(uk)^2 + B^2} \right) \tau_z + \frac{uk}{\sqrt{(uk)^2 + B^2}} \Delta \tau_x. \tag{6.28}$$

The final step is to take the limit $k \to 0$. In the limit $B \gg E_{so}$, the two other helical modes are far removed, and the low–energy sector takes the form

$$\widetilde{\mathcal{H}} = B\tau_z - \frac{uk}{B} \Delta \tau_x \tag{6.29}$$

This is 2×2 equation linear in k, so it already looks promising. Rotating the Pauli matrices by $\pi/2$ around the z axis with the operator

$$\mathcal{R} = e^{i\frac{\pi}{4}\tau_z} \tag{6.30}$$

and recalling the identity $\sigma_i \sigma_j = i\epsilon_{ijk}\sigma_k$ and that Pauli matrices anticommute, we see that Equation (6.29) becomes

$$\widetilde{\mathcal{H}}_R = \mathcal{R}\widetilde{\mathcal{H}}_R\mathcal{R}^{-1} = B\tau_z + \frac{u}{B} k \Delta \tau_y, \tag{6.31}$$

which is indeed equivalent to Equation (6.12), for which we explicitly derived the topological quantum number $\mathcal{M}$ and the existence of the edge states.

Confident that the Oreg model maps onto Kitaev model, this concludes our discussion of Majorana Fermions in nanowires with spin–orbit coupling. The goal of the next section is to present an alternative route to the Oreg model.

6.3 MAJORANA BOUND STATES IN WIRES WITHOUT SPIN–ORBIT COUPLING

We will now discuss in detail our model for realizing Majorana fermions in nanowires without intrinsic spin orbit coupling. The idea is inspired by a proposal due to Choy *et al.* [124] who showed that an array of magnetic nanoparticles, with non–collinear arrangements of the magnetic moments, could harbor Majorana quasiparticles. Related, Braunecker *et al.* [125] showed that in one dimension, a spiralling magnetic field is equivalent to a Rashba–type spin–orbit interaction. We take these two works as inspiration and analytically show the the mapping onto the Oreg model, as well numerically calculating the topological quantum number $\mathcal{Q}$ (discussed below), using a model with permanent micromagnets.

The punch–line of our study is the following: For a 1D nanowire, with proximity induced superconductivity, a spatially varying effective magnetic field can be mapped to a Rashba–type spin–orbit interaction term, thus producing the same model as described by Oreg *et al.*. In light of the discussion in the previous section we're confident such a setup will also have Majorana particles. The system we have in mind is depicted in Figure 6.8. We note, that a bent nanowire with an anisotropic g–factor, can also be mapped onto the Oreg model in the presence of uniform external magnetic field. However, the micromagnet proposal allows more flexibility in tuning the fabrication and parameters, so we study this in detail below. In the Nambu basis of

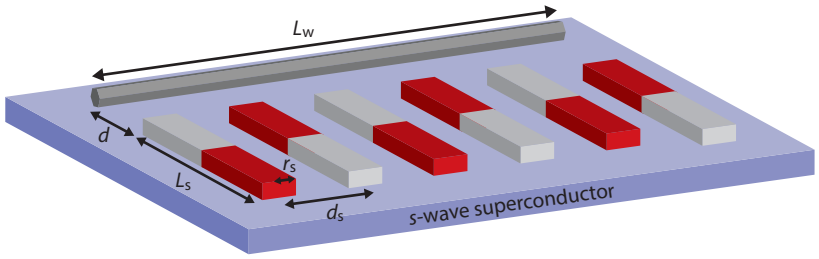

FIGURE 6.8: A nanowire of length L_w deposited on an s–wave superconductor. The in–plane magnetic fingers will produce an effective spin–orbit interaction term in the Hamiltonian of the nanowire.

Section 6.2 the Hamiltonian is written as $H = \frac{1}{2}\int d\xi \Psi^\dagger \mathcal{H} \Psi$, with

$$\mathcal{H} = \left(\frac{p_\xi^2}{2m} - \mu\right)\tau_z + \frac{1}{2} g\mu_B \boldsymbol{B}(\xi)\cdot\boldsymbol{\sigma} + \Delta\tau_x, \tag{6.32}$$

where ξ is the coordinate that parametrizes propagation along the direction of the wire. To keep this section relatively close to experiment I have re–introduced g and μ_B. The part of $\mathcal{H}$ diagonal in particle–hole space is denoted $\mathcal{H}_0$ and superconducting part is denoted $\mathcal{H}_S$. To see that this system is equivalent to a Rashba–type spin–orbit interaction, a little footwork is needed. The following section is essentially the theory equivalent of a fabrication recipe. So, start with a unitary rotation

$$\mathcal{U} = e^{i\phi\sigma_{xy}/2}, \quad \sigma_{xy} = \frac{\boldsymbol{B}\times\hat{z}}{|\boldsymbol{B}\times\hat{z}|}\boldsymbol{\sigma}, \quad \cos\phi = \frac{\boldsymbol{B}}{|\boldsymbol{B}|}\hat{z} \tag{6.33}$$

Applying $\mathcal{U}$ to Equation (6.32) yields

$$\widetilde{\mathcal{H}}_0 \equiv \mathcal{U}\mathcal{H}_0\mathcal{U}^\dagger = \left(\frac{p_\xi^2}{2m} - \mu\right)\tau_z + \frac{1}{2} g\mu_B B\sigma_z + \widetilde{\mathcal{H}}_R + \widetilde{\mathcal{H}}_2, \tag{6.34}$$

where

$$\widetilde{\mathcal{H}}_2 = -\frac{1}{2m}\mathcal{U}^\dagger\partial_x^2\mathcal{U}\tau_z, \quad \widetilde{\mathcal{H}}_R = -\frac{i}{m}\mathcal{U}^\dagger\partial_x\mathcal{U}p_\xi\tau_z. \tag{6.35}$$

Noting $\sigma_{xy}\sigma_{xy} = \mathbf{1}$, the term $\partial_{\tilde{\xi}}\mathcal{U}$ can be evaluated to

$$\begin{aligned}\partial_{\tilde{\xi}}\mathcal{U} &= \partial_{\tilde{\xi}}\left(\cos\phi(\xi)/2 + i\sigma_{xy}(\xi)\sin\phi(\xi)/2\right) \\ &= i\frac{\phi'(\xi)}{2}\sigma_{xy}(\xi)\mathcal{U} + i\sigma'_{xy}(\xi)\sin\phi(\xi)/2, \end{aligned} \tag{6.36}$$

where $'$ denotes derivative with respect to ξ. Plugging back into Equation (6.35) yields

$$\widetilde{H}_R = \frac{1}{m}\left(\frac{1}{2}\phi'\sigma_{xy} + \mathcal{U}^\dagger\sigma'_{xy}\sin\phi/2\right)p_{\tilde{\xi}}\tau_z. \tag{6.37}$$

Before we evaluate $\widetilde{H}_2$ we consider a slightly more concrete model, namely, we choose the field–lines of B to lie in a single plane, and choose $\hat{z}$ to be in this plane, which yields $\sigma'_{xy} = 0$. To avoid a sign–change exactly when $\overline{B} \parallel \hat{z}$ we choose $\sigma_{xy} = \sigma_\perp$ as a constant and let $\phi(\xi)$ vary. In this model we evaluate $\widetilde{\mathcal{H}}_2$ to

$$\widetilde{H}_R = \frac{1}{2m}\left(\frac{i}{2}\phi''\sigma_\perp + \frac{1}{4}\left(\phi'\right)^2\right). \tag{6.38}$$

The first term is an imaginary magnetic field, which keeps the overall Hamiltonian hermitiean, and the second term renormalizes the chemical potential. Using $\sigma_{xy} = \sigma_\perp$ the $\widetilde{\mathcal{H}}_R$ reduces to

$$\boxed{\widetilde{\mathcal{H}}_R = \alpha_{\text{eff}}\sigma_\perp p_{\tilde{\xi}}\tau_z, \quad \alpha_{\text{eff}} = \frac{\hbar}{2m}\frac{d\phi}{d\tilde{\xi}}} \tag{6.39}$$

Where we have reintroduced $\hbar$. This equation is the main result of our analytical work: An in–plane varying magnetic field produces an effective spin–orbit like term in the rotated frame of the electron, and the value is governed by the curvature of the field. The full effective Hamiltonian within this model is thus

$$\widetilde{\mathcal{H}} = \left(\frac{p_{\tilde{\xi}}^2}{2m} - \tilde{\mu} + \alpha_{\text{eff}}\sigma_\perp p_{\tilde{\xi}} - \frac{i}{2}\phi''\sigma_\perp\right)\tau_z + \frac{1}{2}g\mu_B B\sigma_z + \Delta\tau_x. \tag{6.40}$$

The superconducting term is not affected by the rotation in spin–space, since the s–wave superconducting wavefunction is spherically symmetric, so $\widetilde{\mathcal{H}}_s = \mathcal{H}_s$. The chemical potential is renormalized to $\tilde{\mu} = \mu - (1/8m)(\phi')^2$

To estimate the value of α_{eff} for realistic parameters, we assume an (optimal) model, given by a sinusoidally oscillating magnetic field $B^{\text{sine}}(\xi) = B_0\left[\sin\xi/R \;\; 0 \;\; \cos\xi/R\right]^T$. Within this concrete model, $\widetilde{\mathcal{H}}_0$ reduces to [125]

$$\widetilde{\mathcal{H}}_0^{\text{sine}} = \left(\frac{p_{\tilde{\xi}}^2}{2m} - \tilde{\mu} + \frac{\hbar^2}{2mR}p_{\tilde{\xi}}\sigma_y\right)\tau_z + \frac{1}{2}g\mu_B B_c\sigma_3. \tag{6.41}$$

Using values $R \approx 100$ nm and $m = 0.014m_e$ relevant for InSb, the value for $\alpha_{\text{eff}}/\hbar \approx 3\cdot 10^4$ m/s. The effective spin orbit parameter from the si-

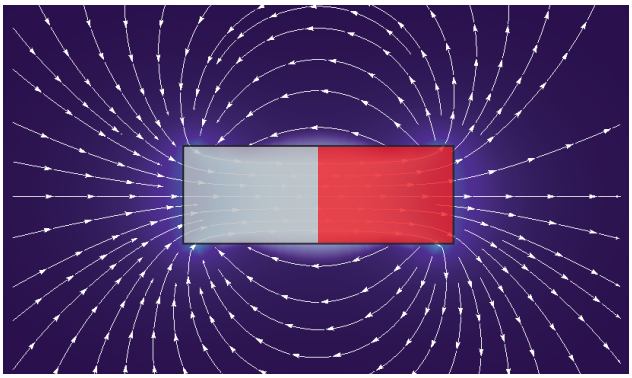

FIGURE 6.9: Magnetic field lines and intensity from a solenoid. The permanent magnet of corresponding dimensions is drawn on top.

nusoidal field is thus comparable to the intrinsic spin orbit coupling in InAs nanowires [126, 127] and the epi–Al/InAs wafers of the preceeding chapters [128]. In the Oreg model, the transition to the topological regime happened when $B > \sqrt{\Delta^2 + \mu^2}$. The renormalization of the chemical potential in the oscillating field model leads to the modified requirement: $B_0 > \sqrt{\Delta^2 + (\mu - \hbar^2/8mR^2)^2}$.

Inspired by the sine–model, we imagine an arrangement of magnetic fingers alternating in their polarization, as in Figure 6.8. The magnetic field from one finger is modeled as the field from a solenoid, $\boldsymbol{B}_{\text{sol}} = B_0 \left[B_\rho \; B_z\right]^T$, with

$$\begin{aligned} B_\rho &= \sqrt{\frac{r_S}{L_s^2 \rho}} \left[\frac{\alpha^2 - 2}{\alpha} \mathcal{E}_1(\alpha^2) + \frac{2}{\alpha} \mathcal{E}_2(\alpha^2) \right]_{\zeta_-}^{\zeta_+} \\ B_z &= -\frac{1}{2\sqrt{L_s \rho}} \left[\zeta \left(\mathcal{E}_1(\alpha^2) + \frac{r_S - \rho}{r_S + \rho} \mathcal{E}_3(\alpha^2, \beta^2) \right) \right]_{\zeta_-}^{\zeta_+}, \end{aligned}$$

where L_s is length of solenoid, r_S is radius of solenoid (see Figure 6.8), $\zeta = z \pm L_S/2$, $\mathcal{E}_i$ is the elliptical integral of the i'th kind, and finally

$$\alpha = \sqrt{\frac{r_S \rho}{(r_S^2 + \rho^2) + \zeta}}, \quad \beta = \sqrt{\frac{r_S \rho}{r_S + \rho)^2}}. \tag{6.42}$$

Figure 6.9 shows the magnetic field from a single finger, using these (unwieldy) expressions.

We proceed by numerically diagonalizing Equation (6.32) in the presence of six solenoids, whose magnetic fields are found using $\boldsymbol{B}_{\text{sol}}$. The exact orientation and placement of the solenoids were chosen to mimic the behavior of $\boldsymbol{B}^{\text{sine}}$. The transition into the topologically non–trivial state is characterized by *i*) a sign–change of the topological quantum number $\mathcal{Q}$, derived from the scattering matrix (see below) and *ii*) the occurrence of a zero–energy state, which remains gapped to the continuum. We will investigate

both these effects for our model. In the next section we derive the quantum number $\mathcal{Q}$, and show that its sign gives the parity of Majorana modes in a wire. The derivation of the scattering matrix used in our numerical models to calculate $\mathcal{Q}$ is derived in Appendix B.

6.3.1 *A topological quantum number*

To quantify the existence of Majorana fermions in the model without spin–orbit coupling, we employ a technique proposed by Akhmerov *et al.* [129] and Fulga *et al.* [130]. The scattering matrix relates incoming wavefunctions impingent on a potential to outgoing wavefunctions, see Figure 6.10a.

$$\begin{pmatrix} \psi_{-,L} \\ \psi_{+,R} \end{pmatrix} = \mathcal{S}(E) \begin{pmatrix} \psi_{+L} \\ \psi_{-,R} \end{pmatrix}, \quad \mathcal{S}(E) = \begin{pmatrix} r(E) & t'(E) \\ t(E) & r'(E) \end{pmatrix} \tag{6.43}$$

The definitions of the components of the vectors are given in Figure 6.10a. Expanding this equation to electron–hole space yields (suppressing depen-

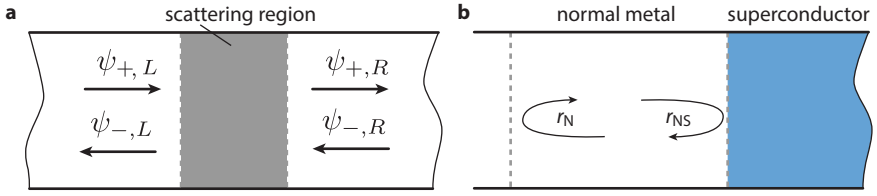

FIGURE 6.10: **a**, Incoming and outgoing waves impingent on a potential. The scattering matrix $\mathcal{S}$ given in Equation (6.43) relates the two wavefronts. **b**, The standard NS sandwich, indicating how Andreev reflection and normal reflection can lead to a standing wave at the interface. See text for details.

dence on E)

$$\begin{pmatrix} \psi^e_{-,L} \\ \psi^h_{-,L} \\ \psi^e_{+,R} \\ \psi^h_{+,R} \end{pmatrix} = \begin{pmatrix} r_{ee} & r_{eh} & & \bar{\bar{t}}' \\ r_{he} & r_{hh} & & \\ & \bar{\bar{t}} & & \bar{\bar{r}}' \\ & & & \end{pmatrix} \begin{pmatrix} \psi^e_{+,L} \\ \psi^h_{+,L} \\ \psi^e_{-,R} \\ \psi^h_{-,R} \end{pmatrix} \tag{6.44}$$

In the following we will be particular interested in the scattering matrix $\bar{\bar{r}}$. In the case of an electron–hole symmetric hamiltonian, the reflection matrix can be simplified. Consider sending in an electron on the left and looking at the reflection

$$\psi^e_{-,L}(E) = r(E)\psi^e_{+,L}(E). \tag{6.45}$$

Applying the electron–hole symmetry operator Ξ yields

$$\Xi\psi^e_{-,L}(E) = \Xi r(E)\Xi^{-1}\Xi\psi^e_{+,L}(E) \Leftrightarrow \tag{6.46}$$
$$\psi^h_{-,L}(-E) = \tau_x r^*(E)\tau_x\psi^h_{+,K}(-E). \tag{6.47}$$

Making the replacement $E \to -E$ allows us to compare coefficients with $S(E)$ and we see that $r_{hh}(E) = r^*_{ee}(-E)$ and $r_{he}(E) = r^*_{eh}(-E)$.

In Figure 6.10b we have sketched the theory–version of an SN interface, and we assume the contacts to be semi–infinite away from the interface, such that there is no transmission of quasiparticles from one end to the other. In this picture, a bound state at the interface at the Fermi–energy E_F (equal to 0 for sake of argument) would correspond to setting a barrier on the left–hand side of the metal, and looking for states that satisfy

$$r_N(0)r_{NS}(0)\Psi = \Psi, \tag{6.48}$$

where r_N gives the scattering from the metal–barrier and r_{NS} gives the scattering of the superconductor interface, i.e.

$$r_N = \begin{pmatrix} N(E) & 0 \\ 0 & N^*(-E) \end{pmatrix}, \quad r_{NS} = \begin{pmatrix} r_{ee} & r_{eh} \\ r_{he} & r_{hh} \end{pmatrix} = \begin{pmatrix} r_{ee}(E) & r_{eh}(E) \\ r^*_{eh}(-E) & r^*_{ee}(-E) \end{pmatrix}. \tag{6.49}$$

Here N is reflection coefficients for electrons, and for the p–h symmetric systems studied here, N^* is the corresponding matrix for holes. As discussed in Chapter 4, for perfect Andreev reflection, the diagonal blocks of r_{NS} are zero. The requirement for a bound state to form at zero energy can be reformulated as a state for which $\det(\mathbf{1} - r_N(0)r_{NS}(0)) = 0$. We will suppress the energy–dependence throughout the remaining of the section. The trick, introduced in [129, 130] is change to the "Majorana" basis, like so

$$r = \Omega r_{NS}\Omega^\dagger, \quad \Omega = \sqrt{\frac{1}{2}}\begin{pmatrix} 1 & 1 \\ -i & i \end{pmatrix} \tag{6.50}$$

The row–vectors of Ω are the Majorana states in electron–hole space that we already saw in the Kitaev model. Inspection shows that r is now a real matrix $r = r^*$, as it should for Majorana states living at zero energy. Determinants are independent of basis, so the basis change of Ω does not alter the determinental requirement to find the bound state. Changing basis on the product $r_N r_{NS}$ in the determinant yields

$$\det(\mathbf{1} - \Omega r_N\Omega^\dagger\Omega r_{NS}\Omega^\dagger) = \det(\mathbf{1} + \mathcal{O}r) = 0. \tag{6.51}$$

By simple insertion, it can be seen that $\mathcal{O}$ is an orthogonal matrix, $\mathcal{O}\mathcal{O}^T = \mathbf{1}$.

A determinant of a matrix $\mathcal{A}$ is the same as the product of eigenvalues of $\mathcal{A}$. Furthermore, if $\mathcal{A}$ is an orthogonal matrix, $\mathcal{A}\mathcal{A}^T = \mathbf{1}$, its determinant must be ± 1, as can be seen from,

$$1 = \det \mathbf{1} = \det \mathcal{A}\mathcal{A}^{-1} = \det \mathcal{A}\mathcal{A}^T = \det \mathcal{A} \det \mathcal{A}^T = \det \mathcal{A} \det \mathcal{A} = (\det \mathcal{A})^2 \tag{6.52}$$

so that $\det \mathcal{A} = \pm 1$. Assume there is $\mathcal{N}$ bound states, corresponding to $\mathcal{N}$ eigenvalues of $\mathcal{O}r$ equal to -1. The remaining eigenvalues must be either 1 or come in pairs $e^{\pm i\theta}$ since $\mathcal{O}r$ is orthogonal. Furthermore, since $\mathcal{O}$ is a unitary transformation of a p–h symmetric scattering matrix r_N, which must preserve probability, its determinant must be unity. Therefore $\det \mathcal{O}r = \det \mathcal{O} \det r = \det r$. Collecting all this, we have

$$\det r = (-1)^{\mathcal{N}} \tag{6.53}$$

which gives the parity of the number of Majorana bound states. For an odd number, there will be an unpaired Majorana at the NS interface, and $\det r$ changes sign. We therefore define

$$\boxed{\mathcal{Q} = \operatorname{sign} \det r = \begin{cases} 1 & \text{No Majorana bound states} \\ -1 & \text{Majorana bound states} \end{cases}} \tag{6.54}$$

In the case of a clean system, in which the momentum is a good quantum number, this result can be mapped to the topological invariant of Kitaev, $\mathcal{M}(H)$ (for details, see [129]). Even though the scattering matrix of the bound state derived in the previous section is real, and the state lives at $E = 0$, we have not formally shown that the bound state is a Majorana state. However, since the underlying Hamiltonian is p–h symmetric, and is devoid of spin–rotation or time–reversal symmetries (due to the external magnetic field) the model is in the Altland–Zirnbauer symmetry class D [131], which in $d = 1$ supports bound states that are Majorana quasiparticles [4].

In the next section we present results and discussion on the topological phase and the associated Majorana end states in the model.

6.3.2 *Numerical results on the zero–energy bound state*

Using the results of the preceeding subsection and the results of the derivation in Appendix B we can quantify what we set out to: Calculate $\mathcal{Q}$ of a nanowire without intrinsic spin–orbit coupling, and study the lowest eigenvalues at the phase transition. Making the replacement

$$\frac{-\hbar^2}{2m}\partial_\xi^2 \psi(\xi) \to -t\left(\psi(\xi + a) - 2\psi(\xi) - \psi(\xi - a)\right), \tag{6.55}$$

where $t = \hbar^2/2ma$ sets the bandwidth, and a is the lattice–spacing, the tight–binding model corresponding to Equation (6.32) is given by

$$\overline{\overline{H}} = \sum_{i=1}^{N} \left(\mathbf{\Psi}_i^\dagger \overline{\overline{h}}_i \mathbf{\Psi}_i + \mathbf{\Psi}_i^\dagger \overline{\overline{t}} \mathbf{\Psi}_{i+1} + \text{h.c.} \right), \tag{6.56}$$

where $\mathbf{\Psi}$ is a four–spinor, and

$$\overline{\overline{h}}_i = (2t - \mu)\tau_z + \Delta\tau_x + \frac{1}{2} g \mu_B \overline{B}(\xi_i) \cdot \overline{\sigma} \tag{6.57}$$

$$\overline{\overline{t}} = -t\tau_z. \tag{6.58}$$

For our specific calculations we have used solenoids with parameters $r_S =$ 600 nm, $L_S = 330$ nm and $d_S = 200$ nm. In the case of alternating alignment of the micromagnets we set $d = 100$ nm, and $d = 50$ nm in the aligned case. These values were chosen to optimize the transition to the topological regime whilst still being possible to microfabricate. The length of the wire L_w is set to 5μm, and the induced superconducting gap is $\Delta = 0.3$ meV. Figure 6.11(a) shows the field–lines of of the alternating and aligned cases, with the micromagnets and wire superimposed. The scale of the device is approximately that used in the calculations. In Figure 6.11b the magnetic field (measured in units of the bare field B_0 of the magnets), is plotted as a function of ξ. We have also calculated the effective value of spin–orbit term in both geometries, shown in blue in figure 6.11b. For the antiparallel alignment we used $N = 1000$ and for the parallel we used $N = 1500$ to ensure proper definition of the discrete version of the derivative involved in calculating α_{eff}. We are indebted to A.P. Higginbotham for pointing out a numerical mistake in the original version of the plot in Figure 6.11. The version of the figure printed here is corrected, and we have published an erratum (M. Kjaergaard *et al.*, Phys. Rev. B., **90**, 059901 (2014))

Using the technique for finding the scattering matrix outlined in Append B, the scattering matrix at $E = 0$, corresponding to a Majorana mode, is found by calculating

$$S(E=0) = \overline{\overline{U}} \left[\mathbf{1} + i\pi\nu \overline{\overline{W}}^\dagger \overline{\overline{H}}^{-1} \overline{\overline{W}} \right]^{-1} \left[\mathbf{1} - i\pi\nu \overline{\overline{W}}^\dagger \overline{\overline{H}}^{-1} \overline{\overline{W}} \right] \overline{\overline{U}}^T, \tag{6.59}$$

where $\overline{\overline{W}}$ is the coupling to the leads, which for the one–channel system we study is a $2 \cdot 4 \times N$–matrix with the structure

$$\overline{\overline{W}} = \begin{bmatrix} \mathbf{1}_{4\times4} & 0 & \cdots & 0 & 0 \\ 0 & 0 & \cdots & 0 & \mathbf{1}_{4\times4} \end{bmatrix}, \tag{6.60}$$

where the identities correspond to the connection to the leads. They are 4–dimensional due particle–hole space and spin space. ν is the density of states of the leads, and due to finite–difference effects, the results presented below are *not* independent of this value, and we have chosen one that most

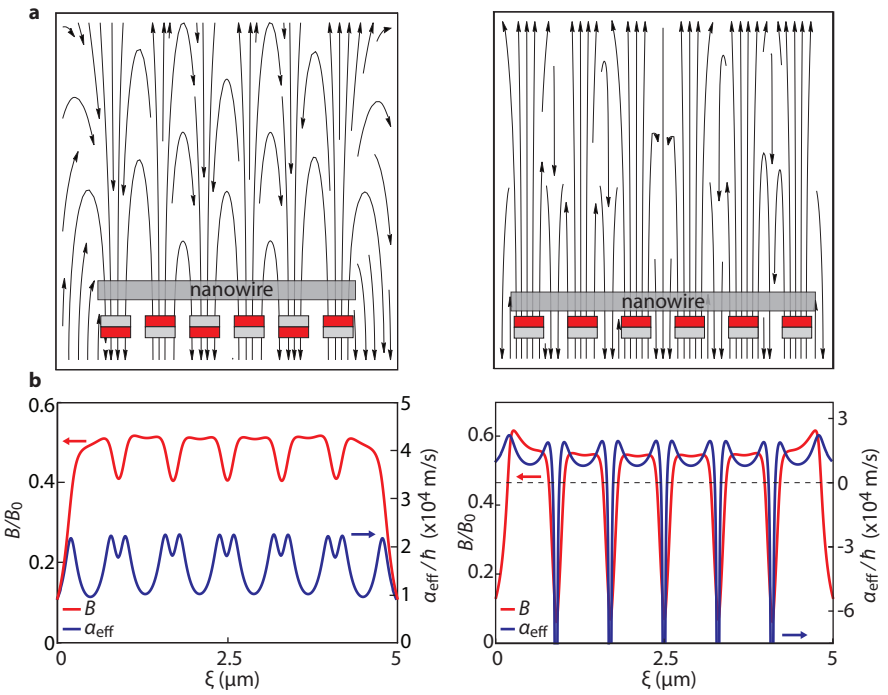

FIGURE 6.11: **a**, The field–lines originating from six solenoids, in two different configurations calculated using our code. The dimensions of the micromagnets is overlayed on the field lines. **b**, The effective magnetic field along the wire (in units of the field at the end of the permanent magnets) and the effective spin–orbit coupling induced by these magnetic fields. Note that in the case of aligned magnets the effective spin–orbit changes sign.

clearly show the transition. Furthermore $\overline{\overline{U}}\,\overline{\overline{U}}^T$ is the scattering matrix in the absence of the coupling to device. In Figure 6.12 we present results for the determinant of r as a function of μ and B_0. r is found by extracting the 4×4 subblock of $S(E = 0)$, calculated via Equation (6.59). A clear transition from the trivial ($\det r = 1$) to the topological ($\det r = -1$) region is seen. For $\mu = 0.3\Delta \approx 0.09meV$ the transition happens at $gB/2\Delta \approx 2.2$ which corresponds to a magnetic field from the magnets of $B \approx 0.3$T for InSb wires with $g \approx 50$. Recently, in the setting of quantum hall interferometry, an experimental setup using permanent magnet fingers of the same size as the ones envisioned in our proposal were fabricated [132]. The authors of [132] report magnetic fields on order comparable to what is needed in this proposal. In Figures 6.12b, 6.12c we show results of a numerical diagonalization of the full tight–binding Hamiltonian. The lowest and next positive eigenvalue is plotted as a function of magnetic field, together with line cuts from the $\det r$–plot. It is evident that the lowest eigenvalue goes to zero, while the other remain gapped, exactly at the transition point predicted from the topological quantum number analysis. This is indicative of the onset of a zero–mode arising in the spectrum. Interestingly, it is clear from Figure 6.12c that also in the model of aligned magnets, a phase–transition occurs, even though the effective spin–orbit term changes sign several times along

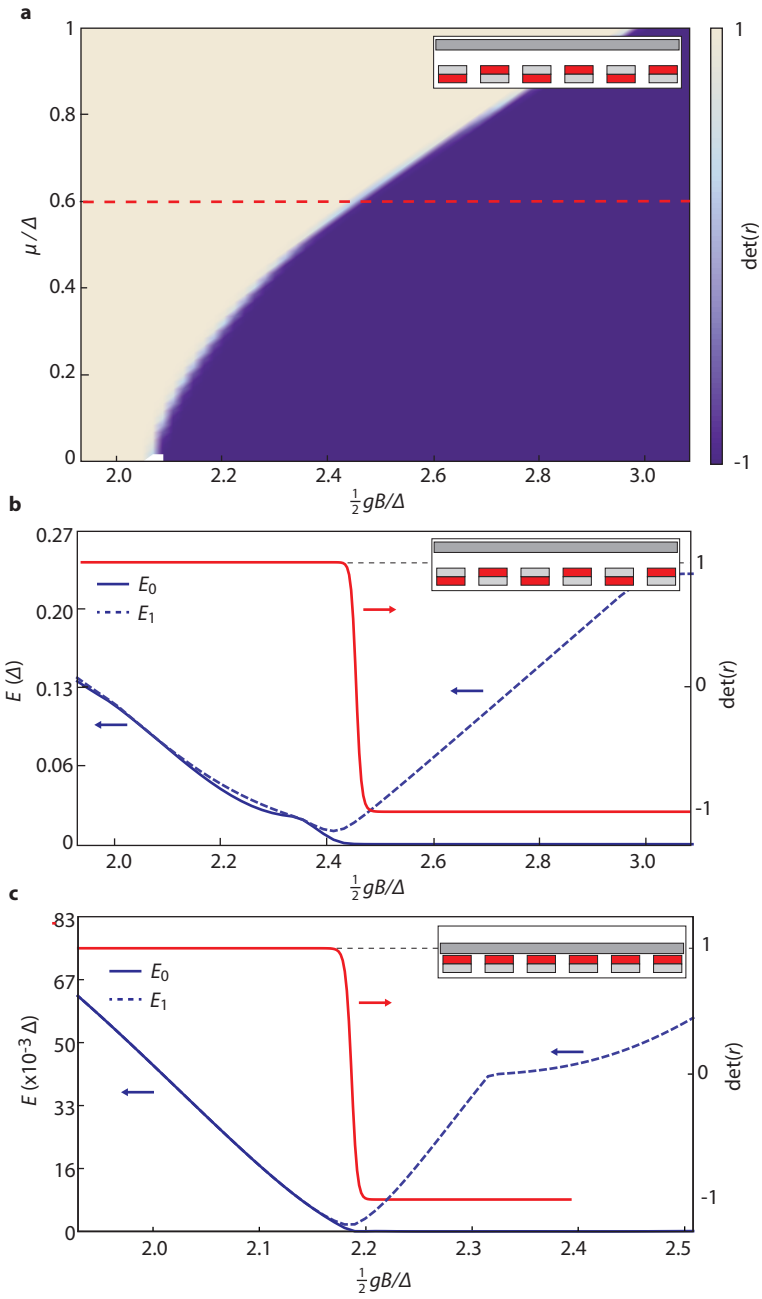

FIGURE 6.12: **a**, The value of det(r) as a function of μ and B (in units of $\Delta = 0.3$ meV) using the alternating orientation of the magnets (see inset). The phase transition into the topological phase is evident. **b,c**, The two lowest positive eigenvalues calculated by numerical diagonalization of the full tight–bind Hamiltonian for aligned and alternating orientation of the micromagnets. The lowest eigenvalue goes to zero at the phase–transition, signaling the onset of a zero–energy mode, simultaneously with det(r) changing sign.

the length of the wire, see Figure 6.11b. This robustness was not studied in greater detail.

Finally we have studied the spin–structure of the Majorana fermion end states. Due to the finite size of the wire, there is a finite, but exponentially

small, overlap between the two lowest eigenmodes. Hence, the lowest eigenstates from the numerical diagonalization procedure, are not localized. Denoting these γ_1 and γ_2, the localized modes are found by $\gamma_a = (\gamma_1 + \gamma_2)/\sqrt{2}$ and $\gamma_b = i(\gamma_1 - \gamma_2)/\sqrt{2}$. In Figure 6.13 we show the weight $|\gamma_{a/b}(\xi)|^2$ of the two localized end–mode. Furthermore, inspired by [133], we numerically calculate the spin–polarization of the Majorana operators via

$$\boldsymbol{S}_{a/b}(\xi_i) = \langle \xi_{a/b} | \xi_i \rangle \langle \xi_i | \overline{\sigma} \otimes \frac{1}{2}(\mathbf{1} + \tau_z) | \gamma_{a/b} \rangle. \tag{6.61}$$

That is to say, we numerically project onto the electronic part of Majorana wavefunctions, and calculate the expectation value of the spin–operator. The inset in figure 6.13 shows the polarization of the Majorana operators. By comparing with Figure 6.11 we note that the polarization follows the field–lines of the permanent magnets. The spin–polarization plays a role for e.g. spin–specific tunneling [134], manipulation [17] and detection [133] of Majorana fermions.

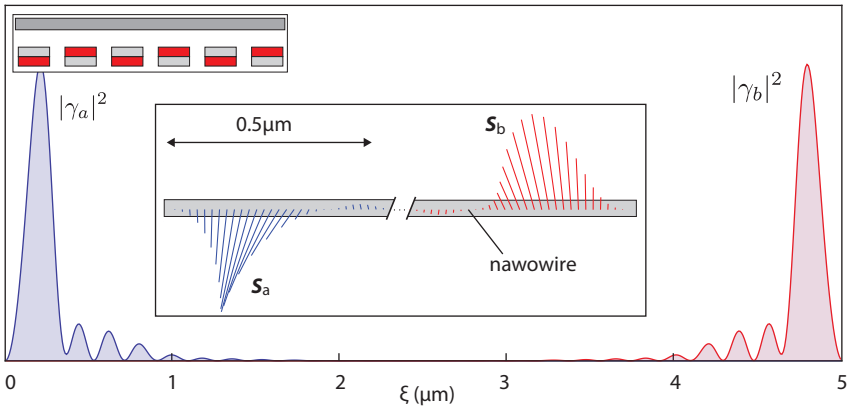

FIGURE 6.13: The density of the two localized Majorana modes for a $L_w = 5\mu$m wire, by numerical diagonalization of the Hamiltonian in Eq.(6.32) subject to the magnetic field from six permanent magnets (see upper left inset). Middle inset: The spin–projection $\overline{S}_{a/b}$ of the two localized Majorana states.

6.4 CONCLUSION

We have shown that in wires subject to a spatially rotating field, the effective Hamiltonian has a spin–orbit like term, scaling with the field–gradient. This model can be mapped back to that discussed by Oreg *et al.* [5], which can again be mapped back to Kitaevs toy model [4], which we showed explicitly has Majorana fermions as its zero–energy solutions in the topological regime. A numerical investigation of a realistic model involving six micromagnets of dimensions and strength that are experimentally feasible showed that for parameters previously reported for such systems, the wire can undergo a phase transition and thereby support Majorana fermions as

its end states. Finally we briefly studied the spin–structure of the localized Majorana modes.

Part IV

APPENDIX

A

SUPERCONDUCTING CONTACTS TO BURIED INAS 2DEG

In this appendix we'll briefly review the fabrication and measurements using a high–mobility, buried InAs 2DEG heterostructure. On a wafer grown under identical conditions to the one discussed in this chapter, the density and mobility was measured to be $n = 3 \cdot 10^{11}$ cm^{-2} and $\mu = 200.000$ cm^2/Vs. The wafer structure is shown in Figure A.1. The growth was optimized for gateability and is described in detail elsewhere [21, 22]. The data on an SN device fabricated on this wafer is discussed in Section A.1 and the fabrication recipe is given in Section A.2.

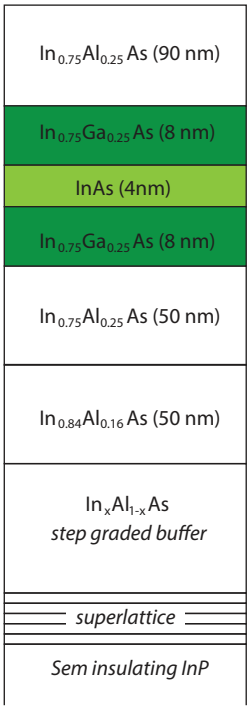

FIGURE A.1: Wafer structure of the high–mobility buried InAs heterostructure.

A.1 GATEABLE SUPERCURRENT AND SOFT GAP

The geometry of the device is shown in Figure A.2a and an SEM picture of the device after measurements is shown in Figure A.2b. The philosophy of the device was to form an effective 1D channel along the superconductcing interface using the plunger gates. The QPC gates on either side would then operate as tunnel probes. The gold extension lines were used to minimize

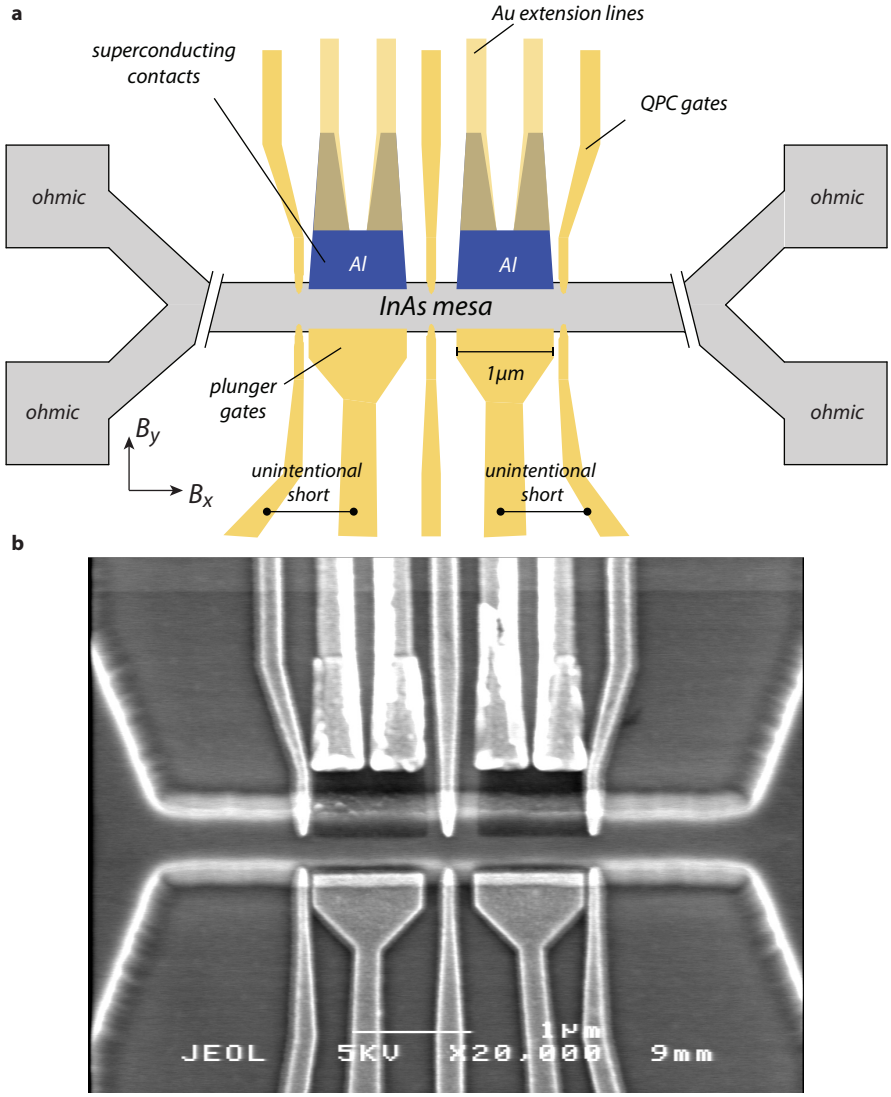

FIGURE A.2: **a**, Device schematic of the quasi 1D wire with superconducting contacts. **b**, SEM image of the device, taken after measurements.

the total area of the aluminum superconducting contacts, to increase B_c. The plunger gates and the bottom QPC gates on either side were unintentionally shorted during fabrication, most likely at the tip, where the gates meet the InAs mesa (see SEM in Figure A.2b). The ohmic contacts are deposited in the same step as the extension lines from the superconducting pads (fabrication details in section A.2), and has a typical contact resistance $R_c \sim 1\ \mathrm{k}\Omega$. Despite the short between plunger and QPC, we could pinch off all 3 QPCs

separately, as shown in Figure A.3. These measurements were done using a 4–terminal voltage bias setup, as indicated on the schematic in Figure A.3, with $V_{ac} = 5\ \mu$V. The drain is connected to a current preamplifier, and the V_+ and V_- are connected to voltage preamplifiers. The superconducting contacts were left floating for these traces. The hysteretic behavior of the gates were less pronounced when the gates were operated close to pinch off point. When we moved the voltage probes to the aluminum pads we observed a

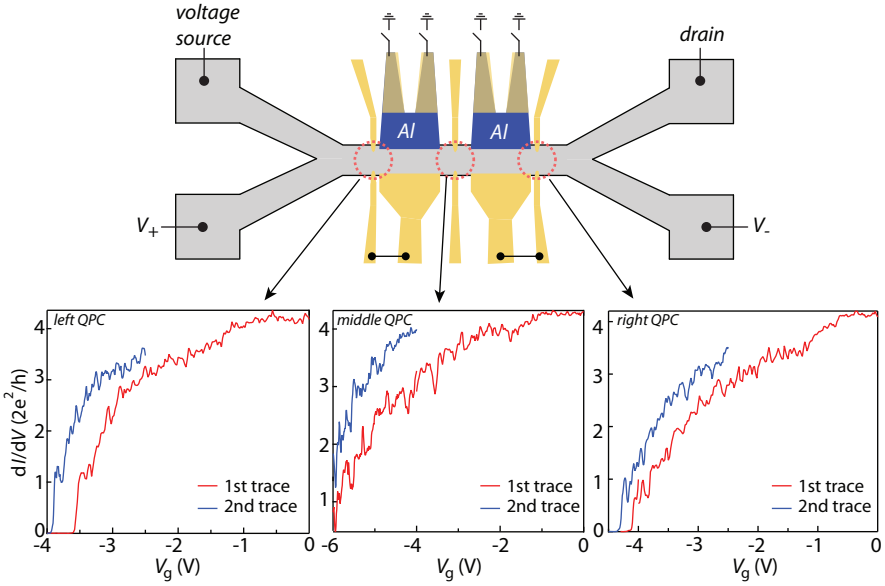

FIGURE A.3: The pinchoff behavior of all 3 QPCs in the device.

supercurrent with $I_c \approx 20$ nA. These measurements were performed in a current biased setup with $I_{ac} = 5$ nA. Engaging the middle QPC the supercurrent pinchoff had a rich behavior, shown in Figure A.4. Finally, the behavior of the QPCs in the highly pinched off (tunnel) regime are shown in Figure A.5. We clearly observe suppressed conductance with an energy scale comparable to, but significantly smaller than, the gap in aluminum. By applying an in–plane field, the gap decays on a scale of $\sim$300 mT, commensurate with expectations for an gap induced from Andreev reflections on InAs/aluminum interface. The middle QPC were too unstable in time to perform proper bias spectroscopy. The amount of subgap conductance (i.e. the "hardness" of the gap) could to some extent be tuned by energizing the plunger gates and using only the top half of the QPC to actively pinch off. The harder we pushed with the plunger gate, the more strongly suppressed the subgap conductance (but the gap would overall remain soft). The most strongly suppressed subgap conductance we were able to measure using this technique is shown in Figure A.6, and was done using the leftmost N–QPC–S device. The gap is approximately $\Delta^\star = 80\ \mu$eV. For reasons unknown, the right side of the device was significantly more unstable and we were never able to generate a 2D map as the one in Figure A.6 for the left side.

It was the plan to fabricate a next set of device using a similar geometry, but replacing aluminum with NbTiN, a high B_c superconductor, as well as optimizing the dielectric for less noise and switching behavior. At this point we were supplied with the epi–Al/InAs wafers of Sections I and II. Given their superior interface and ease of fabrication, all subsequent devices were fabricated on those wafers.

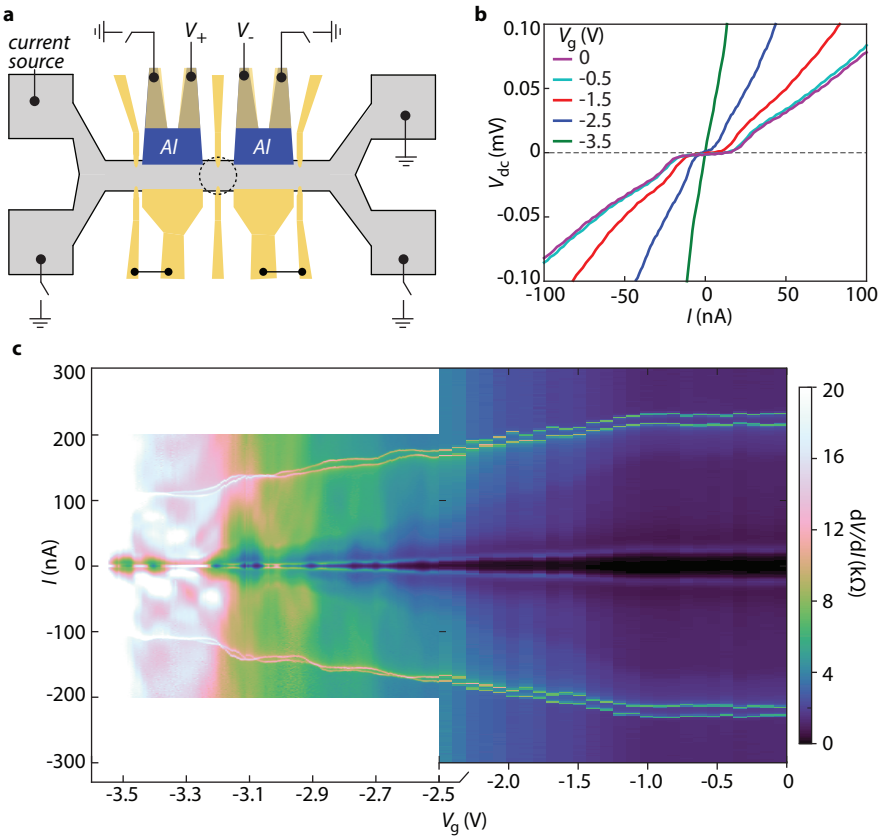

FIGURE A.4: **a**, Indication of measurement setup for measuring the supercurrent between the two tunnel probes. **b**, DC voltage drop as the QPC gates are energized. The magnitude of the critical current decreases, and the normal state resistance increases. **c**, Differential resistance between the superconducting contacts as the middle QPC is energized. The scaling on the x–axes is different in the range $V_g \in [-3.6, -2.5]$ V, to emphasize the structure near pinchoff.

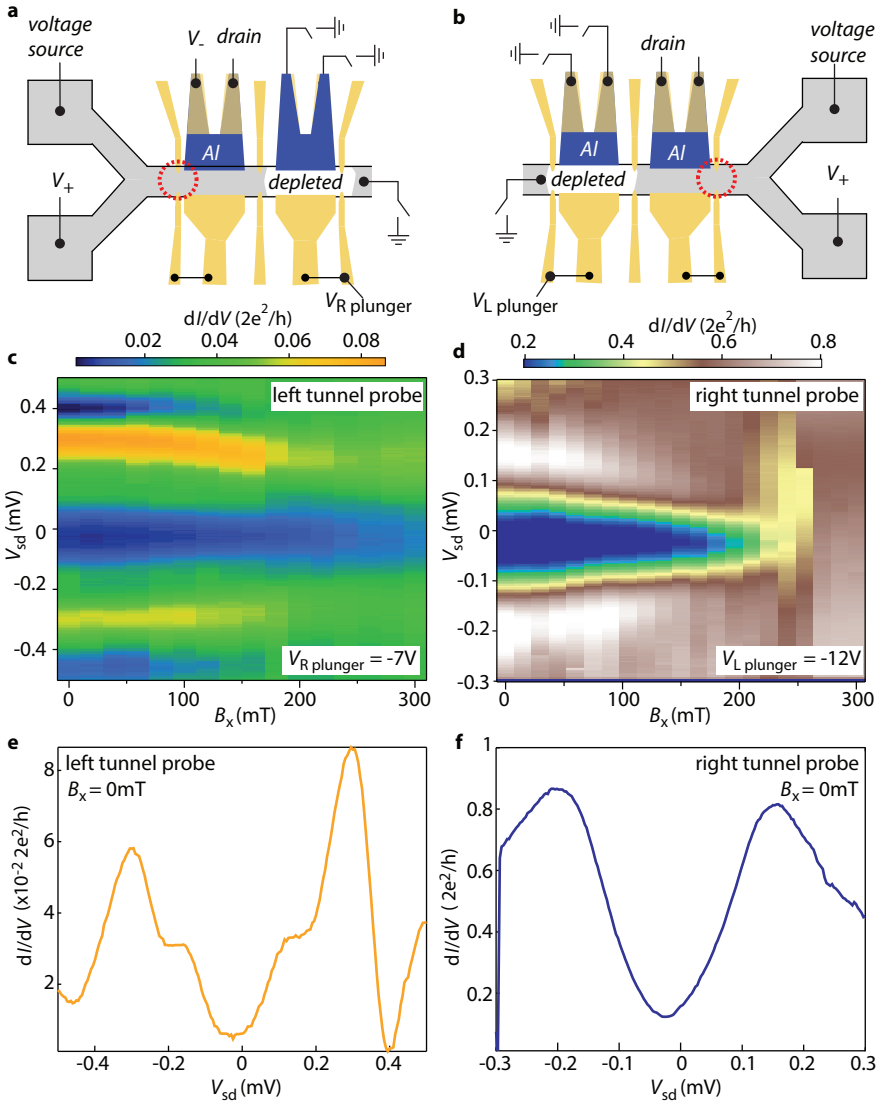

FIGURE A.5: **a**, Measurement setup for measuring density of states on the left device. The red circle indicates the tunnel probe. The right arm of the mesa is depleted using $V_{\text{R plunger}}$. **b**, Measurement setup for measuring density of states on the right device. Red circle indicates the tunnel probe. The left arm of the mesa is depleted using $V_{\text{L plunger}}$. **c**, Density of states on the left side as the in–plane field is ramped. The right plunger gate was parked at $V_{\text{R plunger}} = -7$ V, to suppress any influence from the right side of the device. **e**, Cut at $B_x = 0$mT in **c**. **d**, Density of states measured with the right tunnel probe. This side was significantly more unstable (a switch is also visible in the data), and we had to set $V_{\text{R plunger}} = -12$ V to properly see a gap. The conductance in these measurements is an order of magnitude larger than **a**, because the right side device was unstable at very low conductances. **f**, Cut at $B_x = 0$mT from panel **d**.

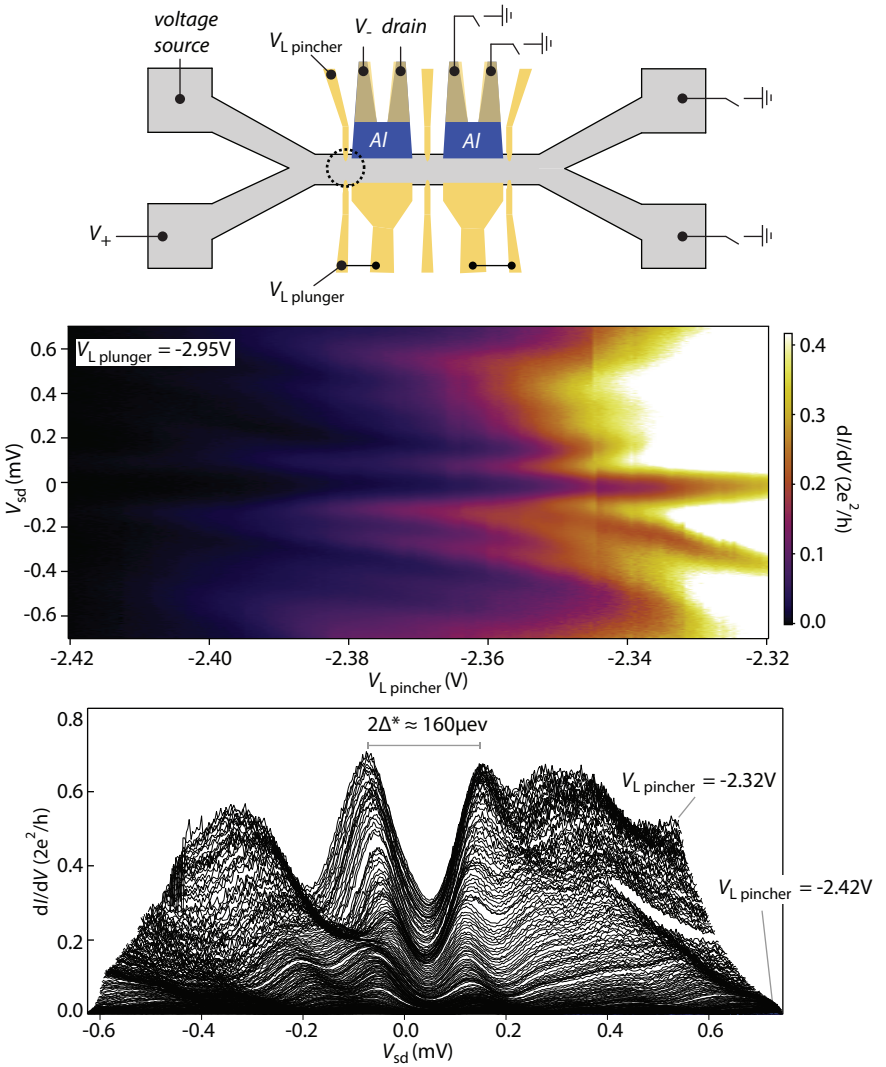

FIGURE A.6: **a**, The "hardest" gap we were able to measure. By parking the bottom QPC (with the accidental short to the plunger) at $V_{\text{L plunger}} = -2.95V$, the properties of the junction over a wide range of conductances could be traced out. **b**, Linecuts in the data in **a**. The curves are not offset. The overall upwards trend of the data as the pincher is pulled back is the background conductance of the device increasing. The data is scaled by the voltage drop measured across the constriction. The horizontal shift on the x–axis (the data is not $\pm$ symmetric) is due to a DC offset on the output of the DAC used to generate the DC signal.

A.2 FABRICATION OF SUPERCONDUCTING CONTACTS TO BURIED INAS

The fabrication of devices with superconducting contacts to the buried heterostructure, as reported in the previous section, follows these 5 steps,

1. Wet etching to define mesas
2. Clean surface and deposit superconductor
3. Deposition of ohmic contacts and gold extension lines from the aluminum contacts
4. Atomic layer deposition
5. Gate deposition

Two steps in particular took significant work to overcome: the problem of the wet etch creeping under the resist, causing bad mesa definition and the problem of forming a clean interface to the superconductor. Both will be highlighted in the recipe below. We note in passing that these wafers also suffered from the surprising problem of leakage between two mesas, after deposition of the ALD (discussed back in Section 3.1.5), if they were not etched deeper than $\sim$ 250 nm. Just as for the epi–Al/InAs the problem was ultimately resolved simply by etching deeper.

In all steps involving e–beam lithography the chip is cleaned prior to depositing resist. The standard 2–solvent clean we use is: 2 min acetone (swirl chip) / 1 min IPA (swirl chip) / blowdry with N_2 / bake for 3 minutes at 185°C. For the e–beam exposure, all high–definition exposures were made with $I = 500$ pA 300 μm writefield, 60.000 points/writefield an varying dosetime depending on the design of what is exposed. For the low–definition large area exposures we use $I = 20$ nA, 500 μm writefield and 20.000 points/writefield. Again, the dose–time is dependent on what is exposed.

Wet etching mesas

CLEAN: Standard 2–solvent clean

SPIN ADHESION PROMOTER: *this step is crucial!* Apply $\sim$3 drops of adhesion promoter AR 300-80 (from AllResist) while spinning at 500 RPM. Then spin 45 seconds at 4000 RPM. Bake 3 minutes at 185°C. Dip in dioxalene for 1 minute to strip excess promoter. IPA for 30 seconds, blowdry and then bake for 3 minutes at 185°C.

SPIN RESIST: Dispense A4 at 500 RPM, then spin at 4000 RPM for 45 seconds. Postbake 3 minutes at 185°C.

E–BEAM LITHOGRAPHY:

High definition: Dwelltime of 0.4 μs/dot. Slightly underexposing the

PMMA, but because of the proximity effect when exposing large regions it will be properly exposed anyway.
Low definition: Dwelltime of 0.36 μs/dot.

DEVELOP: 60 seconds MIBK:IPA followed by 20 seconds IPA and blowdry.

WET ETCH: The wet etch is a variation on the etch used for the epi–Al/InAs wafer:

H_2O	:	H_3PO_4	:	H_2O_2
80	:	1	:	1

As always for H_2O_2 store it in a cool dark place, and *don't use it if it's been open for more than* $\sim$ 4 weeks. Add phosphoric acid to a larger beaker of water on a magnet stirrer. Then add H_2O_2 and let it mix for $\sim$2 mins before dunking chip. Etch rate is approximate 1nm/second, so etch for at least 5 minutes, while keeping magnet stirrer on. Then dip into milliQ water and swirl for 30 seconds. Blowdry and then into hot acetone to strip resist. Measure height using AFM/profilometer and check it is greater then 250 nm.

Surface cleaning and superconductor deposition

CLEAN: Standard 2–solvent clean

SPIN RESIST: Dispense A4 at 500 RPM, then spin at 4000 RPM for 45 seconds. Postbake 3 minutes at 185°C.

E–BEAM LITHOGRAPHY: *High definition*: Dwelltime of 0.6 μs/dot.

DEVELOP: 60 seconds MIBK:IPA followed by 20 seconds IPA and blowdry.

PREDEPOSITION ETCH CLEAN: *crucial step*. Using same etchant recipe as when etching mesas, dip for 20 seconds to clean of oxides from the surface. Move chip into milliQ beaker and swirl. Walk to the deposition machine with chip still in milliQ. Vent the machine. Only when you're ready to load, remove the chip from water, blowdry heavily and make sure *all* water is off (if not, it will boil once loadlock is pumping down). Load into evaporator labeled AJA 2.

PREDEPOSITION PLASMA CLEAN: Rotate to 0 degree and start 50RPM. Open substrate shutter and strike plasma at 100 sccm, 30 mTorr and 50 W power. Once on, change pressure to 3 mTorr. Let run for 60 seconds. Visually inspect that the plasma is on and that the reflected power is $\sim$0 W.

SUPERCONDUCTOR DEPOSITION: Without breaking vacuum now commence following deposition: 5 nm titanium at 5 degree, at 50 RPM. Then tilt to 30 degree and deposit 30 nm aluminum while still rotating. Finally deposit 30nm aluminum at 0 degree.

LIFTOFF: Overnight in room temperature acetone. Corners of the chip can be scratched with a syringe.

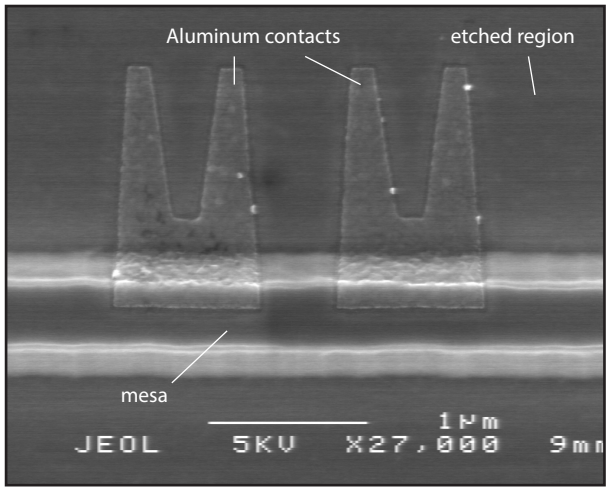

FIGURE A.7: SEM image of 60nm thick aluminum contacts to buried InAs quantum well.

Ohmic contacts and bondpads to superconductors

The ohmic contacts are formed by mechanically removing the surface layer of the exposed InAs meas in large regions, far from the main part of the device. The metals used for the ohmics and bondpads for aluminum superconductors is Ti/Pt/Au. Since Al/Au forms the "purple death" intermetallic at elevated temperatures, we deposit the platinum as a spacer.

CLEAN: Standard 2–solvent clean

SPIN RESIST: Use a bilayer this time: Dispense EL-6 at 500 RPM, then spin at 4000 RPM for 45 seconds. Bake 3 minutes at 185°C, then dispense A-4 at 500 RPM, then spin at 4000 RPM for 45 seconds. Bake 3 minutes at 185°C,

E–BEAM LITHOGRAPHY:

High definition: Dwelltime of 0.6 μs/dot.
Low definition: Dwelltime of 0.44 μs/dot.

DEVELOP: 60 seconds MIBK:IPA followed by 20 seconds IPA and blowdry.

PREDEPOSITION MECHANICAL CLEAN: *crucial step*. We use the argon Kaufmann mill to mechanically remove the oxide from the surface of the aluminum contacts, as well as from the surface of exposed InAs on the ohmics. Rotate stage at 50 RPM with Kaufmann mill pointed perpendicular to the plane of the chip. Use 30 sccm argon, setpoint 0.6 mTorr. Turn on Kaufmann gun with a 300 V and check that emission is $\sim$46 mA. Clean for 150 seconds.

SEMICONDUCTOR DEPOSITION: Without breaking vacuum, rotate the sample to point towards e–beam targets. Use following deposition, all while rotating at 50 RPM: 5 nm titanium at 0 degree / 15 nm platinum at 10 degree tilt / 20 nm gold at 10 degree tilt / 60 nm at 0 degree tilt.

LIFTOFF: Scratch corners with syringe and then overnight in room temperature acetone. The liftoff can be tricky because the MMA/PMMA will have deteriorated from the Kaufmann milling. Check under microscope before blowdrying. If

Atomic layer deposition

Rinse the chip in IPA and blowdry thoroughly before loading. Deposit 400 pulses of TMA at 90 °C with a wait time of 1 minute between each pulse.

Gate deposition

The gate exposure and gate deposition is similar to those in Section 3.1.6, and the dwelltime and resist stack will depend on the detailed design of the gates. For the device reported in the previous section we used same bilayer stack as for ohmic contacts, with 0.72 μs/dot dwelltime for high resolution and 0.44 μs/dot dwelltime for low resolution. The gates are made of Ti(5 nm) / Au(65 nm).

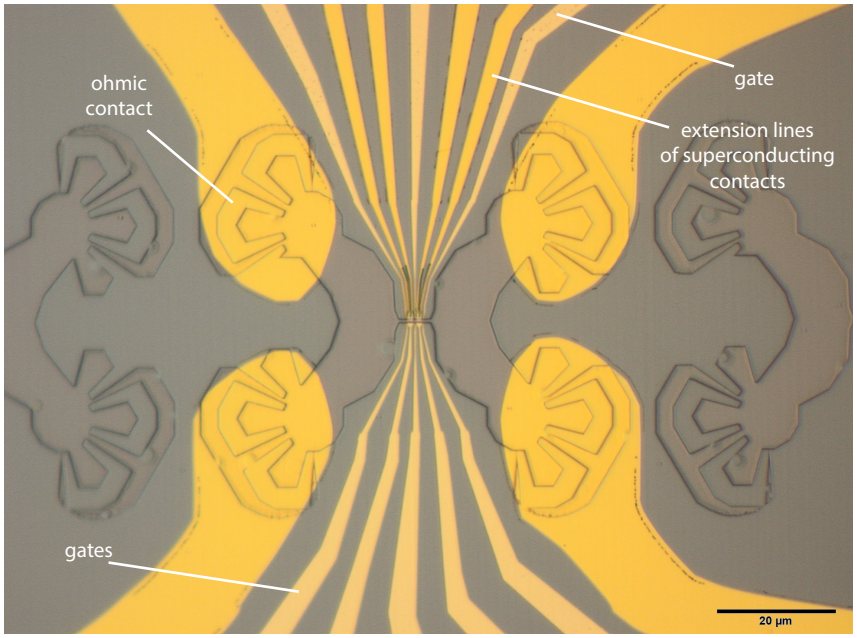

FIGURE A.8: Optical image of the finalized device, whose superconducting contacts are shown in Figure A.7. The SEM image in Figure A.2b is a zoom in on the inner region of this device.

B

DERIVATION OF THE SCATTERING MATRIX FOR A GENERAL 2–LEAD SYSTEM

In this appendix we derive the formula used for numerically calculating the scattering matrix of a device with the general structure "lead–device–lead" needed to calculate $\mathcal{Q}$ in Section 6.3.1. The derivation is a little heavy handed, but the punchline, given in Equation (B.16) is extremely powerful, so we work out the details explicitly in this appendix.

To calculate the scattering matrix we follow Aleiner *et al.* [135]. The electronic states in a 1D model of the "lead–device–lead" device can be written as

$$\psi(x) = \int \frac{dk}{2\pi} \left(\mathcal{U}^* e^{i(k_F+k)x} + \mathcal{U} e^{-i(k_F+k)x} \right) \psi(k) \tag{B.1}$$

The unitary matrix $\mathcal{U}$ describes scattering in leads in the absence of coupling to the device. Note that $\mathcal{U}$ could seem like scattering matrix, but rather $\mathcal{U}^T\mathcal{U}$ is the scattering matrix. The terms $\mathcal{U}\psi(k)$ is to be understood as $\sum_{j,l=1}^{N_{\text{ch}}} \mathcal{U}_{ij}\psi_j(k)$, with N_{ch} being the number of channels. We take the boundary condition that $\psi(x = 0) = 0$ corresponding to a π–phaseshift at the boundary. If we neglect channel mixing $\mathcal{U}$ is a diagonal matrix with i on the diagonal, $\mathcal{U} = i\mathbf{1}$. To generalize the scattering matrix in Equation (6.43) to the case of many modes, we use write the incoming and outgoing states as

$$a^{\text{out}} = \mathcal{S}(\epsilon) a^{\text{in}}, \tag{B.2}$$

where $\mathcal{S}$ is now an $N_{\text{ch}} \times N_{\text{ch}}$–matrix, and a's are $N_{\text{ch}} \times 1$ vectors. At energy $\epsilon = v_F k$ the states in the lead takes the form

$$\psi(x) = a^{\text{in}} e^{i(k_F+\epsilon/v_F)x} + a^{\text{out}} e^{-i(k_F+\epsilon/v_F)x} \tag{B.3}$$

The Hamiltonian for the lead–device system is $H = H_D + H_L + H_{LD}$, where

$$H_L = v_F \int \frac{dk}{2\pi} k\psi^\dagger(k)\psi(k) \tag{B.4}$$

$$H_D = \mathcal{H}\phi^\dagger\phi \tag{B.5}$$

$$H_{LD} = \int \frac{dk}{2\pi} \left(\mathcal{W}\phi^\dagger\psi(k) + \mathcal{W}^\dagger\psi(k)\phi\right) \tag{B.6}$$

States in the device are denoted by ϕ, and $\mathcal{H}$ is an $N \times N$–matrix, describing interactions on the device, such that $\mathcal{H}\phi^\dagger\phi$ is to be understood as $\sum_{\alpha,\beta}^{N} \mathcal{H}_{\alpha,\beta}\phi_\alpha^\dagger\phi_\beta$. The leads are assumed to be metallic so the momentum is linear around k_F. The matrix $\mathcal{W}$ has dimension $N \times N_{\text{ch}}$ and gives the coupling between the states in the leads and states in the device. We are now interested in working out $\mathcal{S}$ in terms of $\mathcal{U}, \mathcal{W}$ and $\mathcal{H}$. To this end, we Fourier–transform the field–operators

$$\psi(k) = \int dx\psi(x)e^{ikx} \quad , \quad \psi^\dagger(k) = \int dx\psi^\dagger(x)e^{-ikx}, \tag{B.7}$$

in the definition of H. We now take $x > 0$ to mean a wave moving towards the device, and $x < 0$ moving away from device see Figure B.1.

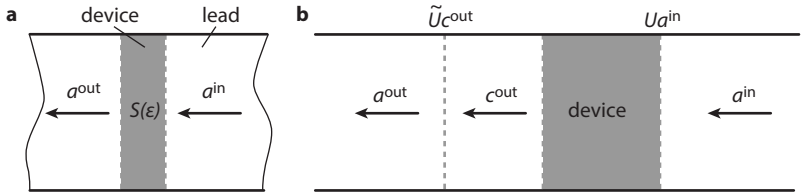

FIGURE B.1: **a**, The generalized multimode scattering matrix. **b**, The journey for a left–moving state as described by Equation (B.12).

The field operators are split into lead and device–space i.e. $\Psi = \psi(x) \otimes \phi$, we evaluate the Schrödinger equation $[H, \Psi] = \epsilon\psi$ term–by–term, to find

$$\begin{aligned} \text{lead:} \quad \epsilon\psi(x) &= iv_F \tfrac{\partial}{\partial x}\psi(x) + \mathcal{W}^\dagger\delta(x)\phi \\ \text{device:} \quad \epsilon\phi &= \mathcal{W}\psi(0) + \mathcal{H}\phi \end{aligned} \tag{B.8}$$

With the sign convention used for the Fourier transform, this equation corresponds to a left–moving state with speed v_F. Such a state can in general be written as

$$\psi(x) = \begin{cases} e^{-ikx}\mathcal{U}a^{\text{in}} & , \quad x > 0 \\ e^{-ikx}\widetilde{\mathcal{U}}c^{\text{out}} & , \quad x < 0 \end{cases} \tag{B.9}$$

The generalized outgoing wave $\widetilde{\mathcal{U}}c^{\text{out}}$ after scattering in the device can be mapped back to the basis of a^{out} as follows: By appealing to figure B.1 the identification $\widetilde{\mathcal{U}}c^{\text{in}} = a^{\text{out}} \Leftrightarrow c^{\text{in}} = \widetilde{\mathcal{U}}^\dagger a^{\text{out}}$ is made. $\widetilde{\mathcal{U}}$ is a unitary. $\widetilde{\mathcal{U}}$

is the same as $\mathcal{U}$ except that the notion of left and right are interchanged. Mathematically, this correspond to

$$\begin{pmatrix} a_{\mathrm{L}}^{\mathrm{in}} \\ a_{\mathrm{R}}^{\mathrm{in}} \end{pmatrix} \rightarrow \tau_x \begin{pmatrix} a_{\mathrm{L}}^{\mathrm{in}} \\ a_{\mathrm{R}}^{\mathrm{in}} \end{pmatrix} = \begin{pmatrix} a_{\mathrm{R}}^{\mathrm{in}} \\ a_{\mathrm{L}}^{\mathrm{in}} \end{pmatrix} \tag{B.10}$$

Thus we may rewrite the scattering equation as follows

$$\begin{pmatrix} a_{\mathrm{L}}^{\mathrm{out}} \\ a_{\mathrm{R}}^{\mathrm{out}} \end{pmatrix} = \mathcal{U} \begin{pmatrix} a_{\mathrm{L}}^{\mathrm{in}} \\ a_{\mathrm{R}}^{\mathrm{in}} \end{pmatrix} \rightarrow \begin{pmatrix} a_{\mathrm{R}}^{\mathrm{out}} \\ a_{\mathrm{L}}^{\mathrm{out}} \end{pmatrix} = \underbrace{\tau_x \mathcal{U} \tau_x}_{=\widetilde{\mathcal{U}}} \begin{pmatrix} a_{\mathrm{R}}^{\mathrm{in}} \\ a_{\mathrm{L}}^{\mathrm{in}} \end{pmatrix}. \tag{B.11}$$

Under the assumption $r = r'$ we see that $\widetilde{\mathcal{U}} = \mathcal{U}^T$, and hence the left–moving state can be written as

$$\psi(x) = \begin{cases} e^{-ikx} \mathcal{U} a^{\mathrm{in}} & , \quad x > 0 \\ e^{-ikx} \mathcal{U}^* a^{\mathrm{out}} & , \quad x < 0 \end{cases} \tag{B.12}$$

To use this wavefunction in Eq.(B.8), we need to evaluate $\psi(0)$ and we will use the regularization $\psi(0) = (\psi(0^-) + \psi(0^+)/2$. The Schrödinger equation for Eq.(B.12) is impossible to solve by matching boundary conditions, since the $\delta(x)$ in Eq.(B.8) introduces a kink. Instead, we employ the "standard" trick of integrating the Schrödinger equation from $0 - \eta$ to $0 + \eta$ and take the limit $\eta \rightarrow 0$. Using this, we arrive at

$$\begin{aligned} \text{lead:} \quad 0 &= i v_F \left(\mathcal{U} a^{\mathrm{in}} - \mathcal{U}^* a^{\mathrm{out}} \right) + \mathcal{W}^\dagger \phi \\ \text{device:} \quad \epsilon \phi &= \tfrac{1}{2} \mathcal{W} \left(\mathcal{U} a^{\mathrm{in}} + \mathcal{U}^* a^{\mathrm{out}} \right) + \mathcal{H} \phi \end{aligned} . \tag{B.13}$$

The device wavefunctions can be isolated from these equations, by rewriting the latter to

$$\phi = (\epsilon \mathbf{1} - \mathcal{H}) \frac{1}{2} \mathcal{W} \left(\mathcal{U} a^{\mathrm{in}} + \mathcal{U}^* a^{\mathrm{out}} \right) = \frac{1}{2} \mathcal{G}(\epsilon) \mathcal{W} \left(\mathcal{U} a^{\mathrm{in}} + \mathcal{U}^* a^{\mathrm{out}} \right), \tag{B.14}$$

where we introduced the Green function $\mathcal{G} = (\epsilon \mathbf{1} - \mathcal{H})$. Insertion into equation (B.13) and combining terms involving a^{in} and a^{out} yields

$$\left(i v_F + \frac{1}{2} \mathcal{W}^\dagger \mathcal{G} \mathcal{W} \right) \mathcal{U}^* a^{\mathrm{out}} = \left(i v_F - \frac{1}{2} \mathcal{W}^\dagger \mathcal{G} \mathcal{W} \right) \mathcal{U} a^{\mathrm{in}}. \tag{B.15}$$

Finally, introducing the density of states $\nu = 1/2\pi v_F$ of the wire, and utilizing that for a unitary matrix $(\mathcal{U}^*)^{-1} = \mathcal{U}^T$ the final result is

$$\boxed{a^{\mathrm{out}} = \mathcal{U}^T \left[1 + i\pi\nu \mathcal{W}^\dagger \mathcal{G}(\epsilon) \mathcal{W} \right]^{-1} \left[1 - i\pi\nu \mathcal{W}^\dagger \mathcal{G}(\epsilon) \mathcal{W} \right] \mathcal{U} a^{\mathrm{in}}} \tag{B.16}$$

By comparing with Eq.(B.2) the scattering matrix can identified.

PUBLICATIONS

1. M. Kjaergaard, F. Nichele, H. J. Suominen, J. A. Folk, M. P. Nowak, A. R. Akhmerov, K. Flensberg, J. Shabani, C. J. Palmstrom and C. M. Marcus, ANDREEV-ENHANCED QUANTUM POINT CONTACT AND TUNNEL SPECTROSCOPY OF A HARD SUPERCONDUCTING GAP IN A 2D INAS ELECTRON GAS, *(to be submitted)*.

2. J. Shabani, M. Kjaergaard, H. J. Suominen, Y. Kim, F. Nichele, K. Pakrouski, T. Stankevic, R. M. Lutchyn, P. Krogstrup, R. Feidenhans'l, S. Kraemer, C. Nayak, M. Troyer, C. M. Marcus, and C. J. Palmstrom, EPITAXIAL AL-INAS TWO-DIMENSIONAL SYSTEMS: A PLATFORM FOR GATEABLE TOPOLOGICAL SUPERCONDUCTIVITY, *(to be submitted)*.

3. M. Kjaergaard, H. J. Suominen, F. Nichele, M. P. Nowak, A. R. Akhmerov, J. Shabani, C. J. Palmstrom and C. M. Marcus, MULTIPLE ANDREEV REFLECTIONS IN HIGHLY TRANSMISSIVE INAS JOSEPHSON JUNCTIONS, *(manuscript in preparation)*.

4. J. T. Mlack, M. Kjaergaard, M. B. Santos, C. M. Marcus IN-PLANE MAGNETOCONDUCTANCE MAPPING OF INSB QUANTUM WELLS, *(to be submitted)*

5. M. Kjaergaard, K. Wölms and K. Flensberg, MAJORANA FERMIONS IN SUPERCONDUCTING NANOWIRES WITHOUT SPIN-ORBIT COUPLING, *Physical Review B: Rapid Communications* **85**, 020503 (2012).

6. C. Barthel, M. Kjaergaard, J. Medford, M. Stopa, C. M. Marcus, M. P. Hanson, A. C. Gossard, FAST SENSING OF DOUBLE-DOT CHARGE ARRANGEMENT AND SPIN STATE WITH A RADIO-FREQUENCY SENSOR QUANTUM DOT, *Physical Review B: Rapid Communications* **81**, 161308 (2012).

BIBLIOGRAPHY

[1] T. M. Klapwijk, "Proximity Effect From an Andreev Perspective," *Journal of Superconductivity*, vol. 17, pp. 593–611, Oct. 2004. (Cited on pages 1, 50, and 51.)

[2] B. Pannetier and H. Courtois, "Andreev Reflection and Proximity effect," *Journal of Low Temperature Physics*, vol. 118, no. 5-6, pp. 599–615, 2000. (Cited on page 1.)

[3] M. Tinkham, *Introduction to Superconductivity*. Dover Publications, 2nd ed., 2004. (Cited on pages 1, 19, 22, 61, and 74.)

[4] A. Y. Kitaev, "Unpaired Majorana fermions in quantum wires," *Physics-Uspekhi*, vol. 44, no. 10S, p. 131, 2001. (Cited on pages 1, 89, 105, and 109.)

[5] Y. Oreg, G. Refael, and F. von Oppen, "Helical Liquids and Majorana Bound States in Quantum Wires," *Physical review letters*, vol. 105, p. 177002, Oct. 2010. (Cited on pages 1, 3, 89, 94, and 109.)

[6] R. M. Lutchyn, J. D. Sau, and S. Das Sarma, "Majorana Fermions and a Topological Phase Transition in Semiconductor-Superconductor Heterostructures," *Physical review letters*, vol. 105, p. 077001, Aug. 2010. (Cited on pages 1, 3, 89, and 95.)

[7] J. D. Sau, R. M. Lutchyn, S. Tewari, and S. Das Sarma, "Generic New Platform for Topological Quantum Computation Using Semiconductor Heterostructures," *Physical review letters*, vol. 104, p. 040502, Jan. 2010. (Cited on pages 1 and 3.)

[8] J. Alicea, "Majorana fermions in a tunable semiconductor device," *Physical Review B*, vol. 81, p. 125318, Mar. 2010. (Cited on pages 1 and 3.)

[9] A. Y. Kitaev, "Fault-tolerant quantum computation by anyons," *Annals of Physics*, vol. 303, pp. 2–30, Jan. 2003. (Cited on page 1.)

[10] D. A. Ivanov, "Non-abelian statistics of half-quantum vortices in p-wave superconductors," *Phys Rev Lett*, vol. 86, pp. 268–271, Jan. 2001. (Cited on page 1.)

[11] C. Nayak, S. H. Simon, A. Stern, M. Freedman, and S. Das Sarma, "Non-Abelian anyons and topological quantum computation," vol. 80, pp. 1083–1159, Jan. 2008. (Cited on pages 1 and 2.)

[12] V. Mourik, K. Zuo, S. M. Frolov, S. R. Plissard, E. P. A. M. Bakkers, and L. P. Kouwenhoven, "Signatures of Majorana Fermions in Hybrid Superconductor-Semiconductor Nanowire Devices," *Science*, vol. 336, pp. 1003–1007, May 2012. (Cited on pages 2 and 89.)

[13] A. Das, Y. Ronen, Y. Most, Y. Oreg, M. Heiblum, and H. Shtrikman, "Zero-bias peaks and splitting in an Al-InAs nanowire topological superconductor as a signature of Majorana fermions," *Nature Physics*, vol. 8, pp. 887–895, Dec. 2012. (Cited on pages 2, 61, and 89.)

[14] M. T. Deng, C. L. Yu, G. Y. Huang, M. Larsson, P. Caroff, and H. Q. Xu, "Anomalous Zero-Bias Conductance Peak in a Nb–InSb Nanowire–Nb Hybrid Device," *Nano Letters*, vol. 12, pp. 6414–6419, Nov. 2012. (Cited on pages 2 and 89.)

[15] S. Das Sarma, M. Freedman, and C. Nayak, "Topologically Protected Qubits from a Possible Non-Abelian Fractional Quantum Hall State," *Physical review letters*, vol. 94, p. 166802, Apr. 2005. (Cited on page 2.)

[16] N. E. Bonesteel, L. Hormozi, G. Zikos, and S. H. Simon, "Braid topologies for quantum computation," *Phys. Rev. Lett.*, vol. 95, p. 140503, Jan. 2005. (Cited on page 2.)

[17] M. Leijnse and K. Flensberg, "Quantum Information Transfer between Topological and Spin Qubit Systems," *Phys. Rev. Lett.*, vol. 107, p. 210502, Jan. 2011. (Cited on pages 3 and 109.)

[18] B. van Heck, A. R. Akhmerov, F. Hassler, M. Burrello, and C. W. J. Beenakker, "Coulomb-assisted braiding of Majorana fermions in a Josephson junction array," *New Journal of Physics*, vol. 14, p. 035019, Mar. 2012. (Cited on page 3.)

[19] T. Hyart, B. van Heck, I. C. Fulga, M. Burrello, A. R. Akhmerov, and C. W. J. Beenakker, "Flux-controlled quantum computation with Majorana fermions," *Physical Review B*, vol. 88, p. 035121, July 2013. (Cited on page 3.)

[20] J. Alicea, Y. Oreg, G. Refael, F. von Oppen, and M. P. A. Fisher, "Non-Abelian statistics and topological quantum information processing in 1D wire networks," *Nature Physics*, vol. 7, pp. 412–417, May 2011. (Cited on page 3.)

[21] J. Shabani, A. P. McFadden, B. Shojaei, and C. J. Palmstrøm, "Gating of high-mobility InAs metamorphic heterostructures," *Applied Physics Letters*, vol. 105, p. 262105, Dec. 2014. (Cited on pages 6, 11, and 113.)

[22] J. Shabani, Y. Kim, A. P. McFadden, R. M. Lutchyn, C. Nayak, and C. J. Palmstrøm, "Tuning spin orbit interaction in high quality gate-defined InAs one-dimensional channels," *arXiv.org*, Aug. 2014. (Cited on pages 6, 11, and 113.)

[23] P. Krogstrup, N. L. B. Ziino, W. Chang, S. M. Albrecht, M. H. Madsen, E. Johnson, J. Nygård, C. M. Marcus, and T. S. Jespersen, "Epitaxy of semiconductor–superconductor nanowires," *Nature Materials*, vol. 14, pp. 400–406, Apr. 2015. (Cited on page 6.)

[24] W. Chang, S. M. Albrecht, T. S. Jespersen, F. Kuemmeth, P. Krogstrup, J. Nygård, and C. M. Marcus, "Hard gap in epitaxial semiconductor–superconductor nanowires," *Nature Nanotechnology*, vol. 10, pp. 232–236, Mar. 2015. (Cited on pages 6, 59, and 61.)

[25] D. C. Tsui, "Observation of Surface Bound State and Two-Dimensional Energy Band by Electron Tunneling," *Physical review letters*, vol. 24, pp. 303–306, Feb. 1970. (Cited on page 10.)

[26] A. Chrestin and U. Merkt, "High characteristic voltages in Nb/p-type InAs/Nb Josephson junctions," *Applied Physics Letters*, vol. 70, no. 23, p. 3149, 1997. (Cited on page 10.)

[27] A. Chrestin, T. Matsuyama, and U. Merkt, "Evidence for a proximity-induced energy gap in Nb/InAs/Nb junctions," *Physical Review B*, vol. 55, pp. 8457–8465, Apr. 1997. (Cited on pages 10, 26, 84, and 86.)

[28] S. G. Lachenmann, A. Förster, I. Friedrich, and D. Uhlisch, "Superconductor/semiconductor step junctions: the basic element for hybrid three terminal devices," *Applied Superconductivity*, vol. 6, pp. 681–688, 1998. (Cited on page 10.)

[29] H. Takayanagi and T. Kawakami, "Superconducting Proximity Effect in the Native Inversion Layer on InAs," *Physical review letters*, vol. 54, pp. 2449–2452, June 1985. (Cited on page 10.)

[30] I. Vurgaftman, J. R. Meyer, and L. R. Ram-Mohan, "Band parameters for III–V compound semiconductors and their alloys," *Journal of Applied Physics*, vol. 89, no. 11, p. 5815, 2001. (Cited on page 11.)

[31] S. Adachi, *Properties of Semiconductor Alloys: Group-IV, III–V and II–VI Semiconductors*. West Sussex: John WIley & Sons Ltd., 2009. (Cited on page 11.)

[32] D. A. Williams, "NS junctions using high-mobility GaAs:AlGaAs heterostructures," *Superlattices and microstructures*, vol. 25, pp. 701–709, May 1999. (Cited on page 12.)

[33] R. Taboryski, J. Kutchinsky, J. B. Hansen, M. Wildt, C. B. Sorensen, and P. E. Lindelof, "Multiple Andreev reflections in diffusive SNS structures," *Superlattices and microstructures*, vol. 25, pp. 829–837, Jan. 1999. (Cited on pages 12 and 75.)

[34] J. Kutchinsky, R. Taboryski, T. Clausen, C. B. Sørensen, A. Kristensen, P. E. Lindelof, J. Bindslev Hansen, C. Schelde Jacobsen, and J. L. Skov, "Decay Lengths for Diffusive Transport Activated by Andreev Reflections in Al/ n-GaAs/Al Superconductor-Semiconductor-Superconductor Junctions," *Physical review letters*, vol. 78, pp. 931–934, Feb. 1997. (Cited on page 12.)

[35] S. De Franceschi, F. Giazotto, F. Beltram, L. Sorba, M. Lazzarino, and A. Franciosi, "Andreev reflection in Si-engineered Al/InGaAs hybrid junctions," *Applied Physics Letters*, vol. 73, no. 26, p. 3890, 1998. (Cited on page 12.)

[36] R. Winkler, *Spin-orbit coupling effects in two-dimensional electron and hole systems*. Springer, 2003. (Cited on pages 15 and 96.)

[37] Y. Imry, "Introduction to mesoscopic physics." Oxford University Press, Oxford, 2002. (Cited on pages 16 and 17.)

[38] B. J. Van Wees, H. van Houten, C. W. J. Beenakker, J. G. Williamson, L. P. Kouwenhoven, D. van der Marel, and C. T. Foxon, "Quantized conductance of point contacts in a two-dimensional electron gas," *Physical review letters*, vol. 60, pp. 848–850, Feb. 1988. (Cited on page 16.)

[39] D. A. Wharam, T. J. Thornton, R. Newbury, M. Pepper, H. Ahmed, J. E. F. Frost, D. G. Hasko, D. C. Peacock, D. A. Ritchie, and G. A. C. Jones, "One-dimensional transport and the quantisation of the ballistic resistance," *Journal of Physics C: Solid State Physics*, vol. 21, pp. L209–L214, Mar. 1988. (Cited on page 16.)

[40] T. Ihn, *Semiconductor Nanostructures*. Oxford University Press, 2010. (Cited on page 17.)

[41] H. A. Fertig and B. I. Halperin, "Transmission coefficient of an electron through a saddle-point potential in a magnetic field," *Physical Review B*, vol. 36, pp. 7969–7976, Nov. 1987. (Cited on page 17.)

[42] M. Büttiker, "Quantized transmission of a saddle-point constriction," *Physical Review B*, vol. 41, pp. 7906–7909, Apr. 1990. (Cited on pages 17 and 57.)

[43] J. Bardeen, L. N. Cooper, and J. R. Schrieffer, "Microscopic Theory of Superconductivity," *Physical Review*, vol. 106, pp. 162–164, Apr. 1957. (Cited on page 19.)

[44] T. Schäpers, *Superconductor/Semiconductor Junctions*, vol. 174 of *Springer Tracts in Modern Physics*. Berlin, Heidelberg: Springer, 2001. (Cited on pages 19, 26, 69, 71, and 72.)

[45] R. Meservey and P. M. Tedrow, "Properties of very thin aluminum films," *Journal of Applied Physics*, vol. 42, no. 51, 1971. (Cited on page 22.)

[46] P. N. Chubov, V. V. Eremenko, and Y. A. Pilipenkko, "Dependence of the critical temperature and energy gap on the thickness of superconducting aluminum films," *JETP Letters*, vol. 28, 1969. (Cited on page 22.)

[47] A. M. Clogston, "Upper Limit for the Critical Field in Hard Superconductors," *Physical review letters*, vol. 9, pp. 266–267, Sept. 1962. (Cited on page 22.)

[48] B. S. Chandrasekhar, "A note on the maximum critical field of high-field superconductors," *Applied Physics Letters*, vol. 1, no. 1, p. 7, 1962. (Cited on page 22.)

[49] L. C. Mur, C. Harmans, J. E. Mooij, J. F. Carlin, and A. Rudra, "Experimental indication for supercurrents carried by opened transport channels," *Physical Review B*, vol. 54, no. 4, pp. R2327–R2330, 1996. (Cited on pages 26 and 75.)

[50] K. Neurohr, A. A. Golubov, T. Klocke, J. Kaufmann, T. Schäpers, J. Appenzeller, D. Uhlisch, A. V. Ustinov, M. Hollfelder, H. Lüth, and A. I. Braginski, "Properties of lateral Nb contacts to a two-dimensional electron gas in an Ino.77Gao.23As/InP heterostructure," *Physical Review B*, vol. 54, pp. 17018–17028, Dec. 1996. (Cited on page 26.)

[51] M. Amado, A. Fornieri, F. Carillo, G. Biasiol, L. Sorba, V. Pellegrini, and F. Giazotto, "Electrostatic tailoring of magnetic interference in quantum point contact ballistic Josephson junctions," *Physical Review B*, vol. 87, p. 134506, Apr. 2013. (Cited on pages 26 and 75.)

[52] "Aluminum Etchants, from Transence Company Inc.." (Cited on page 31.)

[53] F. Pobell, *Matter and Methods at Low Temperatures*. Berlin, Heidelberg: Springer, 3rd ed., 2007. (Cited on page 40.)

[54] A. T. A. M. de Waele, "Basic Operation of Cryocoolers and Related Thermal Machines," *Journal of Low Temperature Physics*, vol. 164, no. 5-6, pp. 179–236, 2011. (Cited on page 40.)

[55] G. E. Volovik, *The Universe in a Helium Droplet*. International Series of Monographs on Physics, Clarendon Press, Oxford: Oxford University Press, 2003. (Cited on page 40.)

[56] A. F. Andreev, "The Thermal Conductivity of the Intermediate State in Superconductors," *Soviet Physics Jetp-Ussr*, vol. 19, no. 5, pp. 1228–1231, 1964. (Cited on page 48.)

[57] G. E. Blonder, M. Tinkham, and T. Klapwijk, "Transition from metallic to tunneling regimes in superconducting microconstrictions: Excess current, charge imbalance, and supercurrent conversion," *Physical Review B*, vol. 25, pp. 4515–4532, Apr. 1982. (Cited on pages 48, 50, 53, 75, and 76.)

[58] A. V. Zaitsev, "Quasiclassical equations of the theory of superconductivity for contiguous metals and the properties of constricted microcontacts," *JETP Letters*, vol. 86, pp. 1742–1758, 1984. (Cited on page 48.)

[59] G. B. Arnold, "Superconducting Tunneling Without the Tunneling Hamiltonian," *Journal of Low Temperature Physics*, vol. 59, no. 1-2, pp. 143–183, 1985. (Cited on page 48.)

[60] Y. V. Nazarov and Y. M. Blanter, *Quantum Transport*. Introduction to Nanoscience, Cambridge University Press, 2009. (Cited on page 51.)

[61] K. Flensberg, J. Hansen, and M. Octavio, "Subharmonic energy-gap structure in superconducting weak links," *Physical Review B*, vol. 38, pp. 8707–8711, Nov. 1988. (Cited on page 53.)

[62] N. W. Ashcroft and D. N. Mermin, *Solid State Physics*. Holt, Rinehart and Winston, 1st ed., 1976. (Cited on page 53.)

[63] F. Deon, V. Pellegrini, F. Giazotto, G. Biasiol, L. Sorba, and F. Beltram, "Quantum dot spectroscopy of proximity-induced superconductivity in a two-dimensional electron gas," *Applied Physics Letters*, vol. 98, p. 132101, Mar. 2011. (Cited on page 54.)

[64] F. Deon, V. Pellegrini, F. Giazotto, G. Biasiol, L. Sorba, and F. Beltram, "Proximity effect in a two-dimensional electron gas probed with a lateral quantum dot," *Physical Review B*, vol. 84, p. 100506, Sept. 2011. (Cited on page 54.)

[65] H. O. H. Churchill, V. Fatemi, K. Grove-Rasmussen, M. T. Deng, P. Caroff, H. Q. Xu, and C. M. Marcus, "Superconductor-nanowire devices from tunneling to the multichannel regime: Zero-bias oscillations and magnetoconductance crossover," *Physical Review B*, vol. 87, p. 241401, June 2013. (Cited on page 61.)

[66] E. J. H. Lee, X. Jiang, M. Houzet, R. Aguado, C. M. Lieber, and S. De Franceschi, "Spin-resolved Andreev levels and parity crossings in hybrid superconductor-semiconductor nanostructures," *Nature Nanotechnology*, vol. 9, pp. 79–84, Jan. 2014. (Cited on page 61.)

[67] S. Takei, B. M. Fregoso, H.-Y. Hui, A. M. Lobos, and S. Das Sarma, "Soft Superconducting Gap in Semiconductor Majorana Nanowires," *Physical review letters*, vol. 110, p. 186803, Apr. 2013. (Cited on pages 61 and 89.)

[68] W. S. Cole, S. D. Sarma, and T. D. Stanescu, "Large superconducting gap in semiconductor Majorana nanowires: Too much of a good thing?," *arXiv.org*, May 2015. (Cited on page 61.)

[69] S. Guéron, H. Pothier, N. O. Birge, D. Esteve, and M. H. Devoret, "Superconducting Proximity Effect Probed on a Mesoscopic Length Scale," *Physical review letters*, vol. 77, pp. 3025–3028, Sept. 1996. (Cited on page 63.)

[70] H. le Sueur, P. Joyez, H. Pothier, C. Urbina, and D. Esteve, "Phase Controlled Superconducting Proximity Effect Probed by Tunneling Spectroscopy," *Physical review letters*, vol. 100, p. 197002, May 2008. (Cited on page 63.)

[71] V. Cherkez, J. C. Cuevas, C. Brun, T. Cren, G. Ménard, F. Debontridder, V. S. Stolyarov, and D. Roditchev, "Proximity Effect between Two Superconductors Spatially Resolved by Scanning Tunneling Spectroscopy," *Physical Review X*, vol. 4, p. 011033, Mar. 2014. (Cited on pages 63 and 85.)

[72] J. Nitta, Y. Lin, T. Akazaki, and T. Koga, "Gate-controlled electron g factor in an InAs-inserted-channel Ino.53Gao.47As/Ino.52Alo.48As heterostructure," *Applied Physics Letters*, vol. 83, pp. 4565–4567, Dec. 2003. (Cited on page 64.)

[73] C. M. Hu, C. Zehnder, C. Heyn, and D. Heitmann, "THz collective spin-flip excitation of a two-dimensional electron system," *Physical Review B*, vol. 67, p. 201302, May 2003. (Cited on page 64.)

[74] C. H. Möller, C. Heyn, and D. Grundler, "Spin splitting in narrow InAs quantum wells with Ino.75Gao.25As barrier layers," *Applied Physics Letters*, vol. 83, pp. 2181–2183, Sept. 2003. (Cited on page 64.)

[75] H. W. Jiang and E. Yablonovitch, "Gate-controlled electron spin resonance in GaAs/AlxGa1−xAsheterostructures," *Physical Review B*, vol. 64, p. 041307, July 2001. (Cited on page 64.)

[76] C. W. J. Beenakker, "Quantum transport in semiconductor-superconductor microjunctions," *Physical Review B*, vol. 46, pp. 12841–12844, Nov. 1992. (Cited on page 64.)

[77] K. Likharev, "Superconducting Weak Links," *Reviews of Modern Physics*, vol. 51, no. 1, pp. 101–159, 1979. (Cited on page 69.)

[78] I. O. Kulik, "Macroscopic Quantization and the Proximity Effect in S-N-S Junctions," *Soviet Physics Jetp-Ussr*, vol. 30, no. 5, p. 944, 1970. (Cited on page 70.)

[79] A. A. Golubov, M. Y. Kupriyanov, and E. Il'Ichev, "The current-phase relation in Josephson junctions," *Reviews of Modern Physics*, vol. 76, no. 2, pp. 411–469, 2004. (Cited on pages 72 and 73.)

[80] P. F. Bagwell, "Suppression of the Josephson current through a narrow, mesoscopic, semiconductor channel by a single impurity," *Physical Review B*, vol. 46, pp. 12573–12586, Nov. 1992. (Cited on page 72.)

[81] C. W. J. Beenakker and H. van Houten, *Semiconductor heterostructures and nanostructures*, vol. 44. New York: Academic Press, 1991. (Cited on page 72.)

[82] H. X. Tang, Z. D. Wang, and Y. Zhang, "Normal reflection effect on the critical current in a clean-limit superconductor–normal-metal–superconductor junction," *Zeitschrift fur Physik B*, vol. 101, pp. 359–366, 1996. (Cited on page 72.)

[83] H. Courtois, M. Meschke, J. Peltonen, and J. Pekola, "Origin of Hysteresis in a Proximity Josephson Junction," *Physical review letters*, vol. 101, p. 067002, Aug. 2008. (Cited on page 74.)

[84] C. W. J. Beenakker and H. van Houten, "Josephson current through a superconducting quantum point contact shorter than the coherence length," *Physical review letters*, vol. 66, pp. 3056–3059, June 1991. (Cited on page 74.)

[85] C. W. J. Beenakker and H. van Houten, "The superconducting quantum point contact," in *Nanostructures and Mesoscopic Systems*, pp. 481–497, Elsevier, 1992. (Cited on page 74.)

[86] J. C. Hammer, J. C. Cuevas, F. S. Bergeret, and W. Belzig, "Density of states and supercurrent in diffusive SNS junctions: Roles of non-ideal interfaces and spin-flip scattering," *Physical Review B*, vol. 76, p. 064514, Aug. 2007. (Cited on pages 74 and 79.)

[87] M. Octavio, M. Tinkham, G. E. Blonder, and T. Klapwijk, "Subharmonic energy-gap structure in superconducting constrictions," *Physical Review B*, vol. 27, pp. 6739–6746, June 1983. (Cited on pages 75 and 81.)

[88] I. O. Kulik and A. O. Omelyanchuk, "Contribution to the microscopic theory of the josephson effect in superconducting bridges," *JETP Letters*, vol. 21, no. 4, pp. 96–97, 1975. (Cited on pages 75 and 78.)

[89] I. O. Kulik and A. O. Omelyanchuk, "Properties of superconducting microbridges in the pure limit," *Soviet Journal of Low Temperature Physics*, vol. 3, pp. 459–461, 1977. (Cited on pages 75 and 78.)

[90] J. Nitta, T. Akazaki, H. Takayanagi, and K. Arai, "Transport properties in an InAs-inserted-channel In 0.52 Al 0.48 As/In 0.53 Ga 0.47 As heterostructure coupled superconducting junction," *Physical Review B*, vol. 46, no. 21, pp. 14286–14289, 1992. (Cited on page 75.)

[91] H. Irie, Y. Harada, H. Sugiyama, and T. Akazaki, "Josephson coupling through one-dimensional ballistic channel in semiconductor-superconductor hybrid quantum point contacts," *Physical Review B*, vol. 89, p. 165415, Apr. 2014. (Cited on page 75.)

[92] S. N. Artemenko, A. F. Volkov, and A. V. Zaitsev, "On the excess current in microbridges S-c-S and S-c-N," *Solid State Communications*, vol. 30, pp. 771–773, June 1979. (Cited on pages 76 and 86.)

[93] J. C. Cuevas, J. Hammer, J. Kopu, J. K. Viljas, and M. Eschrig, "Proximity effect and multiple Andreev reflections in diffusive superconductor–normal-metal–superconductor junctions," *Physical Review B*, vol. 73, p. 184505, May 2006. (Cited on pages 76 and 79.)

[94] A. Chrestin, T. Matsuyama, and U. Merkt, "Critical currents and supercurrent oscillations in Josephson field-effect transistors," *Physical Review B*, vol. 49, pp. 498–504, Jan. 1994. (Cited on page 76.)

[95] H. Takayanagi and T. Akazaki, "Critical-Current Oscillations due to Interference Effects in a Clean-Limit Superconductor-Two-Dimensional-Electron-Gas-Superconductor Junction," *Japanese Journal of Applied Physics*, vol. 34, pp. 4552–4554, Aug. 1995. (Cited on page 76.)

[96] H. Takayanagi, T. Akazaki, and J. Nitta, "Interference effects on the critical current in a clean-limit superconductor–normal-metal–superconductor junction," *Physical Review B*, vol. 51, pp. 1374–1377, Jan. 1995. (Cited on page 76.)

[97] W. Haberkorn, H. Knauer, and J. Richter, "A theoretical study of the current-phase relation in Josephson contacts," *Physica Status Solidi A*, vol. 47, pp. K161–K164, June 1978. (Cited on page 78.)

[98] T. T. Heikkila, J. Sarkka, and F. K. Wilhelm, "Supercurrent-carrying density of states in diffusive mesoscopic Josephson weak links," *Physical Review B*, vol. 66, no. 18, 2002. (Cited on page 79.)

[99] J. Gu, W. Cha, K. Gamo, and S. Namba, "Properties of niobium superconducting bridges prepared by electron-beam lithography and ion implantation," *Journal of Applied Physics*, vol. 50, no. 10, p. 6437, 1979. (Cited on page 79.)

[100] Y. Harada, S. Jensen, T. Akazaki, and H. Takayanagi, "Anomalous magnetic flux periodicity of supercurrent in mesoscopic SNS Josephson junctions," *Physica C: Superconductivity*, vol. 367, pp. 229–233, Feb. 2002. (Cited on page 79.)

[101] J. Paajaste, M. Amado, S. Roddaro, F. S. Bergeret, D. Ercolani, L. Sorba, and F. Giazotto, "Pb/InAs Nanowire Josephson Junction with High Critical Current and Magnetic Flux Focusing," *Nano Letters*, vol. 15, pp. 1803–1808, Feb. 2015. (Cited on page 79.)

[102] T. M. Klapwijk, G. E. Blonder, and M. Tinkham, "Explanation of subharmonic energy gap structure in superconducting contacts," *Physica B+C*, vol. 109-110, pp. 1657–1664, July 1982. (Cited on page 81.)

[103] E. N. Bratus, V. S. Shumeiko, and G. Wendin, "Theory of Subharmonic Gap Structure in Superconducting Mesoscopic Tunnel Contacts," *Physical review letters*, vol. 74, pp. 2110–2113, Mar. 1995. (Cited on page 81.)

[104] D. V. Averin, "Theory of ac Josephson effect and noise in superconducting constrictions," Mar. 1998. (Cited on page 81.)

[105] A. Kastalsky, A. W. Kleinsasser, L. H. Greene, R. Bhat, F. P. Milliken, and J. P. Harbison, "Observation of pair currents in superconductor-semiconductor contacts," *Physical review letters*, vol. 67, pp. 3026–3029, Nov. 1991. (Cited on page 83.)

[106] A. A. Golubov and M. Y. Kupriyanov, "Quasiparticle current in ballistic NcN'S junctions," *Physica C*, vol. 259, no. 1-2, pp. 27–35, 1996. (Cited on page 84.)

[107] B. A. Aminov, A. A. Golubov, and M. Y. Kupriyanov, "Quasiparticle current in ballistic constrictions with finite transparencies of interfaces," *Physical Review B*, vol. 53, no. 1, pp. 365–373, 1996. (Cited on pages 84 and 86.)

[108] A. F. Volkov, P. H. C. Magnée, B. J. Van Wees, and T. M. Klapwijk, "Proximity and Josephson effects in superconductor-two-dimensional electron gas planar junctions," *Physica C: Superconductivity*, vol. 242, pp. 261–266, Feb. 1995. (Cited on page 84.)

[109] N. B. Kopnin and A. S. Melnikov, "Proximity-induced superconductivity in two-dimensional electronic systems," *Physical Review B*, vol. 84, p. 064524, Aug. 2011. (Cited on page 84.)

[110] N. B. Kopnin, A. S. Melnikov, I. A. Sadovskyy, and V. M. Vinokur, "Weak links in proximity-superconducting two-dimensional electron systems," *Physical Review B*, vol. 89, p. 081402, Feb. 2014. (Cited on page 84.)

[111] C. Nguyen, H. Kroemer, and E. L. Hu, "Anomalous Andreev conductance in InAs-AlSb quantum well structures with Nb electrodes," *Physical review letters*, vol. 69, pp. 2847–2850, Nov. 1992. (Cited on pages 84 and 85.)

[112] C. Nguyen, H. Kroemer, and E. L. Hu, "Contact resistance of superconductor-semiconductor interfaces: The case of Nb-InAs/AlSb quantum-well structures," *Applied Physics Letters*, 1994. (Cited on pages 84 and 85.)

[113] W. L. McMillan, "Tunneling Model of the Superconducting Proximity Effect," *Physical Review*, vol. 175, pp. 537–542, Nov. 1968. (Cited on page 84.)

[114] D. Chevallier, P. Simon, and C. Bena, "From Andreev bound states to Majorana fermions in topological wires on superconducting substrates: A story of mutation," *Physical Review B*, vol. 88, p. 165401, Oct. 2013. (Cited on page 90.)

[115] D. Rainis, L. Trifunovic, J. Klinovaja, and D. Loss, "Towards a realistic transport modeling in a superconducting nanowire with Majorana fermions," *Physical Review B*, vol. 87, p. 024515, Jan. 2013. (Cited on page 90.)

[116] P. Ghosh, J. D. Sau, S. Tewari, and S. Das Sarma, "Non-Abelian topological order in noncentrosymmetric superconductors with broken time-reversal symmetry," *Physical Review B*, vol. 82, p. 184525, Nov. 2010. (Cited on page 92.)

[117] S. Tewari, T. D. Stanescu, J. D. Sau, and S. Das Sarma, "Topological minigap in quasi-one-dimensional spin-orbit-coupled semiconductor Majorana wires," *Physical Review B*, vol. 86, p. 024504, July 2012. (Cited on page 92.)

[118] C. H. L. Quay, T. L. Hughes, J. A. Sulpizio, L. N. Pfeiffer, K. W. Baldwin, K. W. West, D. Goldhaber-Gordon, and R. de Picciotto, "Observation of a one-dimensional spin–orbit gap in a quantum wire," *Nature Physics*, vol. 6, pp. 336–339, Mar. 2010. (Cited on page 96.)

[119] D. Rainis and D. Loss, "Conductance behavior in nanowires with spin-orbit interaction: A numerical study," *Physical Review B*, vol. 90, p. 235415, Dec. 2014. (Cited on page 96.)

[120] M. M. Uddin, H. W. Liu, K. F. Yang, K. Nagase, T. D. Mishima, M. B. Santos, and Y. Hirayama, "Characterization of InSb quantum wells with atomic layer deposited gate dielectrics," *Applied Physics Letters*, vol. 101, p. 233503, Dec. 2012. (Cited on page 96.)

[121] M. M. Uddin, H. W. Liu, K. F. Yang, K. Nagase, K. Sekine, C. K. Gaspe, T. D. Mishima, M. B. Santos, and Y. Hirayama, "Gate depletion of an InSb two-dimensional electron gas," *Applied Physics Letters*, vol. 103, no. 12, p. 123502, 2013. (Cited on page 96.)

[122] W. Yi, A. A. Kiselev, J. Thorp, R. Noah, B.-M. Nguyen, S. Bui, R. D. Rajavel, T. Hussain, M. F. Gyure, P. Kratz, Q. Qian, M. J. Manfra, V. S.

Pribiag, L. P. Kouwenhoven, C. M. Marcus, and M. Sokolich, "Gate-tunable high mobility remote-doped InSb/In1−xAlxSb quantum well heterostructures," *Applied Physics Letters*, vol. 106, p. 142103, Apr. 2015. (Cited on pages 96 and 97.)

[123] S. V. Iordanskii, Y. B. Lyanda-Geller, and G. E. Pikus, "Weak localization in quantum wells with spin-orbit interaction," *JETP Letters*, vol. 60, no. 3, p. 206, 1994. (Cited on page 96.)

[124] T. P. Choy, J. M. Edge, A. R. Akhmerov, and C. W. J. Beenakker, "Majorana fermions emerging from magnetic nanoparticles on a superconductor without spin-orbit coupling," *Phys. Rev. B*, vol. 84, p. 195442, Jan. 2011. (Cited on page 99.)

[125] B. Braunecker, P. Simon, and D. Loss, "Nuclear Magnetism and Electronic Order in C-13 Nanotubes," *Phys. Rev. Lett.*, vol. 102, p. 116403, Jan. 2009. (Cited on pages 99 and 101.)

[126] P. Roulleau, T. Choi, S. Riedi, T. Heinzel, and I. Shorubalko, "Suppression of weak antilocalization in InAs nanowires," *Physical Review B*, vol. 81, no. 15, p. 155449, 2010. (Cited on page 102.)

[127] S. Estévez Hernández, M. Akabori, K. Sladek, C. Volk, S. Alagha, H. Hardtdegen, M. G. Pala, N. Demarina, D. Grützmacher, and T. Schäpers, "Spin-orbit coupling and phase coherence in InAs nanowires," *Physical Review B*, vol. 82, p. 235303, Dec. 2010. (Cited on page 102.)

[128] J. Shabani, M. Kjaergaard, H. J. Suominen, Y. Kim, F. Nichele, K. Pakrouski, T. Stankevic, R. M. Lutchyn, P. Krogstrup, R. Feidenshansl, S. Kraemer, M. Troyer, C. M. Marcus, and C. J. Palmstrøm, "Epitaxial Al-InAs two-dimensional systems: a platform for gate-able topological superconductivity," *In Preparation*. (Cited on page 102.)

[129] A. R. Akhmerov, J. P. Dahlhaus, F. Hassler, M. Wimmer, and C. W. J. Beenakker, "Quantized Conductance at the Majorana Phase Transition in a Disordered Superconducting Wire," *Phys. Rev. Lett.*, vol. 106, p. 057001, Jan. 2011. (Cited on pages 103, 104, and 105.)

[130] I. C. Fulga, F. Hassler, A. R. Akhmerov, and C. W. J. Beenakker, "Scattering formula for the topological quantum number of a disordered multimode wire," *Phys. Rev. B*, vol. 83, p. 155429, Jan. 2011. (Cited on pages 103 and 104.)

[131] A. Altland and M. R. Zirnbauer, "Nonstandard symmetry classes in mesoscopic normal-superconducting hybrid structures," *Phys. Rev. B*, vol. 55, pp. 1142–1161, Jan. 1997. (Cited on page 105.)

[132] B. Karmakar, D. Venturelli, L. Chirolli, F. Taddei, V. Giovannetti, R. Fazio, S. Roddaro, G. Biasiol, L. Sorba, V. Pellegrini, and F. Beltram,

"Controlled Coupling of Spin-Resolved Quantum Hall Edge States," *Phys. Rev. Lett.*, vol. 107, p. 236804, Jan. 2011. (Cited on page 107.)

[133] D. Sticlet, C. Bena, and P. Simon, "Spin and Majorana Polarization in Topological Superconducting Wires," *Phys. Rev. Lett.*, vol. 108, p. 096802, Jan. 2012. (Cited on page 109.)

[134] K. Flensberg, "Non-Abelian Operations on Majorana Fermions via Single-Charge Control," *Phys. Rev. Lett.*, vol. 106, p. 090503, Jan. 2011. (Cited on page 109.)

[135] I. L. Aleiner, P. W. Brouwer, and L. I. Glazman, "Quantum effects in Coulomb blockade," vol. 358, pp. 309–440, Jan. 2002. (Cited on page 123.)